Master Thesis

Czech Technical University in Prague

F3

Faculty of Electrical Engineering
Department of Cybernetics

Tactile Sensors Based on Graphene Aerogel

Bc. Tomáš Chaloupecký

Supervisor: doc. Matěj Hoffmann, Ph.D.
Supervisor–specialist: Ing. Bedřich Himmel
Study program: Cybernetics and Robotics
May 2023

MASTER'S THESIS ASSIGNMENT

I. Personal and study details

Student's name: **Chaloupecký Tomáš**

Personal ID number: **483548**

Faculty / Institute: **Faculty of Electrical Engineering**

Department / Institute: **Department of Cybernetics**

Study program: **Cybernetics and Robotics**

II. Master's thesis details

Master's thesis title in English:

Tactile Sensors Based on Graphene Aerogel

Master's thesis title in Czech:

Taktilní senzory na bázi grafenového aerogelu

Guidelines:

Tactile sensors are based on different principles (capacitive, resistive, magnetic, optical; e.g. [1]-[4]) and made from different materials, determining the sensor properties like sensitivity, range, hysteresis etc. Recently, graphene aerogel was found to have promising properties as a contact resistance-based tactile sensor [5]. In collaboration with the Institute of Physics of the Czech Academy of Sciences, the goal of this thesis is to turn the material into a functional prototype of a tactile sensor for robotics.
Instructions:
1. Familiarize yourself with the graphene-based resistive tactile sensor.
2. Design a circuit for measuring changes in electrical resistance and read data.
3. Experiment with different designs of a single tactile sensor - the attachment of graphene aerogel to a substrate, protective layer covering the sensor etc. and study the sensitivity, hysteresis, drift, and robustness of the sensor preparation.
4. Pick the most robust solution and turn into a full sensor prototype (including power and data transfer) attached to a robot gripper.
5. If time permits, prepare a sensor matrix (for example 2x2 or larger).
6. Test the sensor in a closed-loop control scenario such as grasping a fragile object. The existing Robotiq 2F-85 gripper with force feedback will serve as a baseline.

Bibliography / sources:

[1] Chen, M. et al. An ultrahigh resolution pressure sensor based on percolative metal nanoparticle arrays. Nat. Commun. 10, 4024 (2019).
[2] Lee, H., Park, H., Serhat, G., Sun, H. & Kuchenbecker, K. J. Calibrating a soft ERT-based tactile sensor with a multiphysics model and sim-to-real transfer learning. In Proc. IEEE International Conference on Robotics and Automation 1632–1638 (IEEE, 2020).
[3] Lambeta, M., Chou, P. W., Tian, S., Yang, B., Maloon, B., Most, V. R., ... & Calandra, R. (2020). DIGIT: A novel design for a low-cost compact high-resolution tactile sensor with application to in-hand manipulation. IEEE Robotics and Automation Letters, 5(3), 3838-3845.
[4] Sun, H., Kuchenbecker, K. J., & Martius, G. (2022). A soft thumb-sized vision-based sensor with accurate all-round force perception. Nature Machine Intelligence, 4(2), 135-145.
[5] Kumar, P., Šilhavík, M., Zafar, Z. A., & Cervenka, J. (2022). Contact resistance based tactile sensor using covalently cross-linked graphene aerogels. Nanoscale.

Name and workplace of master's thesis supervisor:

doc. Mgr. Mat j Hoffmann, Ph.D.   Vision for Robotics and Autonomous Systems FEE

Name and workplace of second master's thesis supervisor or consultant:

Ing. Bed ich Himmel   Vision for Robotics and Autonomous Systems FEE

Date of master's thesis assignment: **01.02.2023**   Deadline for master's thesis submission: **26.05.2023**

Assignment valid until: **22.09.2024**

_____   _____   _____
doc. Mgr. Mat j Hoffmann, Ph.D.   prof. Ing. Tomáš Svoboda, Ph.D.   prof. Mgr. Petr Páta, Ph.D.
Supervisor's signature   Head of department's signature   Dean's signature

III. Assignment receipt

The student acknowledges that the master's thesis is an individual work. The student must produce his thesis without the assistance of others, with the exception of provided consultations. Within the master's thesis, the author must state the names of consultants and include a list of references.

_____   _____
Date of assignment receipt   Student's signature

Acknowledgements

I would like to thank my supervisors Matěj Hoffman a Bedřich Himmel for guidance and patience. Next, I thank Sergiu Popescu for his help with the stylistics of the text. Special thanks to my parents, partner, and cat for their support. Finally, I would like to thank the Institute of Physics of the Czech Academy of Science for collaboration on this project, namely Jiří Červenka and Prabhat Kumar.

Declaration

I declare that the presented work was developed independently and that I have listed all sources of information used within it in accordance with the methodical instructions for observing the ethical principles in the preparation of university theses.

Prohlašuji, že jsem předloženou práci vypracoval samostatně a že jsem uvedl veškeré použité informační zdroje v souladu s Metodickým pokynem o dodržování etických principů při přípravě vysokoškolských prací.

V Praze dne 26. května 2023

. . . .
Tomáš Chaloupecký

Abstract

In robotics, hands and grippers are being equipped various types of tactile and force sensors. These sensors can help increase the robustness of grasping tasks or contribute to safety in human-robot interaction. Currently developed sensors are based on several principles, from electronic ones measuring changes in electric units, to vision-based sensors, which use low-cost camera sensors to estimate deformation. A few years ago, a new material was discovered, the graphene aerogel. Graphene aerogel is a substance that shows unique mechanical properties like superelasticity. In combination with electrical conductivity, this makes it a very promising material for tactile sensing. This thesis describes the design of a series of tactile sensor prototypes based on the graphene aerogel. The different designs were extensively experimentally tested and compared to other tactile sensors. In addition to this, a custom electronic system was designed and manufactured to measure and process sensory data. Finally, closed-loop grasping experiments with the sensor mounted on a robot gripper were performed and compared to the performance of the gripper force feedback. This thesis was conducted in collaboration with the Institute of Physics of the Czech Academy of Sciences, which developed the graphene aerogel.

Keywords: Tactile sensor, Graphene Aerogel, Robotic grasping

Supervisor: doc. Matěj Hoffmann, Ph.D.

Abstrakt

V robotice jsou ramena a chapadla vybavována různými typy taktilních senzorů. Tyto senzory pomáhají zvýšit robustnost uchopování předmětů a přispívají ke zvýšení bezpečnosti při interakci člověka s robotem. V současnosti používané senzory jsou založeny na různých principech, počínaje elektronickými, měřící změny v elektrických veličinách, po senzory založené na strojovém vidění, které používají levné kamery k odhadování deformace. Před několika lety byl vyvinut nový materiál, grafenový aerogel. Grafenový aerogel vykazuje unikátní mechanické vlastnosti, jako je superelasticita. V kombinaci s elektrickou vodivostí tohoto materiálu se jedná o slibný materiál pro snímání taktilní informace. V této práci popisujeme návrh několika prototypů založených na grafenovém aerogelu. Navržené prototypy jsme podrobili testům a výsledky porovnali s ostatními taktilními senzory. Nadále jsme vyvinuli vlastní elektronický systém k měření a zpracování dat ze senzoru. Na závěr jsme náš senzor použili k pokusům se zpětnovazebním řízením, kdy byl senzor usazen na robotické chapadlo, a porovnali jsme výkon našeho senzoru a silové zpětné vazby použitého chapadla. Tuto práci jsme vypracovali v kolaboraci s Fyzikálním ústavem české akademie věd.

Klíčová slova: Taktilní sensor, Grafenový aerogel, Robotické uchopovnání

Překlad názvu: Taktilní senzory na bázi grafenového aerogelu

Contents

Chapter 1

Introduction

Tactile sensors and artificial skins are proving to be useful sensors in modern robotics. Giving a robot a sense of touch can lead to much better performance in grasping tasks, especially in the case of fragile objects, or in the case of physical uncertainties of the grasped object [1]. Next, covering the robot with artificial skin can lead to safer applications in human-robot interactions [2]. These sensors and skins can be based on various principles. Generally, capacitive, piezoresistive, vision-based, magnetic, or pneumatic sensors are used [3–7].

To compare tactile sensors, parameters such as sensitivity, dynamic range, frequency response, or reaction time can be used. Recently published sensors based on contact resistance show high sensitivity, however, the dynamic range shows to be rather low. Examples of devices that measure pressure can usually be seen in the range of several kPa [3, 8, 9]. Other resistive sensors based on tunneling effect show a dynamic range of up to $2\,\mathrm{MPa}$ [10]. Our research introduces a new possible sensor based on a new material that shows a much higher dynamic range [11].

In recent years, researchers at the Institute of Physics of the Czech Academy of Sciences, Department of Thin Films and Nanostructures (IoP) have developed new materials that show remarkable mechanical features. It is called a graphene aerogel. It is highly flexible, showing mechanical resonance frequencies even in units of MHz [11]. Graphene aerogel, GA for short, is also electrically conductive. When the electrodes are attached, contact resistance between them and GA is formed. This contact resistance is highly dependent on the normal force applied due to the elastic deformation of GA against contacts. We exploit this relation in the design of the sensor. As graphene aerogel shows such mechanical properties, it is a promising material for a new type of tactile sensor.

In collaboration with IoP, we developed a tactile sensor based on a graphene aerogel. Prototypes of such sensors were already published in [12], however, this design still requires improvements before it could be used in a practical situation. We improved the mechanical construction of the sensor itself and designed the electronics to process the signal produced by the sensor. Our goal was to create a sensor that incorporates more than one tactile unit (taxel) to enhance the spatial distribution of the forces. In case of a GA based sensor, one taxel can measure forces on relatively small area (in units of mm^2), whereas the area of regular a gripper is much larger (in units of cm^2). According to researchers from IoP blocks of GA greater than a few cubic millimeters tend to break apart easily. A sensor composed of multiple small GA blocks is the only way to build such a multitaxel sensor. On the

1

other hand, designing a multitaxel system is a more complex task. To divide this task into smaller parts, we started with design of one taxel sensor. After optimizing individual taxel sensor, we used developed technology to manufacture several tactile units and formed a multitaxel sensor.

In the first part of this thesis, we focus on sensor design. We experiment several ways of mechanical construction and show their advantages and disadvantages. We show our final design of single and multitaxel sensor based on our research.

Next, we introduce our design of an electronic system that is used to measure resistance changes in a tactile matrix. This system is developed specifically for this purpose to suit our needs. Specifically, it is capable of simple interfacing to Robotic Operational System (ROS), features taxel addressing, and allows to set suitable signal processing for each taxel.

In the third section of this thesis we conducted series of experiments on our designed sensors. To test the developed sensor, we designed instruments testing sensor's dynamic range or frequency response, as these tools are not standard measurement devices and are not easily to commercially acquire. The results of these experiments were compared to those of the published sensors. Not all parameters we measured are usually shown in publications, however, we find them also important. For example, the frequency range is not the usual topic of tactile sensor articles even though it is crucial to measure mechanical vibrations. Furthermore, articles publishing new sensor prototypes rarely show the influence of other variables such as temperature or humidity, which we evaluated to determine the robustness of the sensor.

In the final part, we used our sensor in a series of grasping experiments when we attached the sensor to the robotic manipulator. We implemented an algorithm to grasp fragile objects such as thin plastic cups, kitchen sponges, or paper cards. This algorithm allows us to grasp objects of unknown dimensions. Since grasped objects differ in stiffness, resulting in different strain-stress curves, different parameters of the PD controller were used for each stiffness group.

Chapter 2

Related Work

In recent years, attempts have been made to give robots a sense of touch. Development of tactile sensors and artificial skins is done by several research teams. Equipping a robot with artificial skin can benefit human-robot interaction or safety measures in industrial context [2].

In this work, we mostly focus on sensor design but to test our sensor, we designed a simple grasp application. As we design our sensor for grasping tasks and manipulation, we are interested in features such as the wide dynamic range of force that the sensor can measure, sensitivity, mechanical integrity, and durability.

Several sensor types were recently published that work on different principles. There are vision-based, capacitive-, magnetic-, hydraulic- or resistive-based sensors. We took the most interest in the resistance-based sensors as they are closest to our work.

Vision-based Sensors

First, let us discuss vision-based sensors. This kind of sensor uses deformable chambers containing light emitters and receptors [13, 14]. Such a receptor can be either singular photo-element or camera. When a chamber or chambers is deformed, the intensity detected by a single photoelement is changed.

In case of more complex sensors, where a camera is used, the light emitted has different colors that form a pattern. When the chain is deformed, the pattern becomes chained. To evaluate such data, convolutional neural networks are used. This project was clearly focused on precise force mapping rather than robust grasping, manipulation, or other tasks. The dynamic range of up to $2\,\mathrm{N}$ reflects such a purpose. Such range may could be enough for delicate manipulation but in case of heavier fragile objects (a glass or a cup) higher force might be needed. Next, we find the video camera as a fragile piece of equipment to be used as a part of the force sensor. On the other hand, the spatial resolution of such a sensor when detecting the touch position appears to be very accurate up to $0.4\,\mathrm{mm}$ [13]. This performance is beyond what we could observe with other sensor principles.

An interesting construction is shown in [6] where a vision-based sensor is used for tactile grasping. The construction of such a sensor is shown in Figure 2.1. The sensor is based on the same principle as [13] and to evaluate sensor data, convolutional neural networks are used. This sensor features very high resolution in a small area. In the article, no mention

of maximal applicable fore nor sensitivity as a function of pressure is made; therefore, we cannot compare this sensor. Despite the fact that the sensor seems to be robustly constructed, we are still would be cautious about the fragility of the sensor.
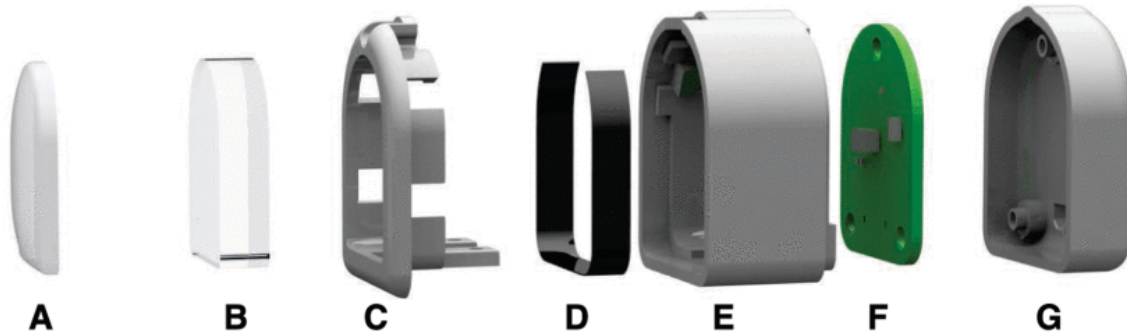
Figure 2.1: Exploded view of a single DIGIT sensor. **A)** elastomer, **B)** acrylic window, **C)** snap-fit holder, **D)** lighting PCB, **E)** plastic housing, **F)** camera PCB, **G)** back housing. Figure and caption from [6].

■ Capacitive Sensors

The next type of sensor is capacitive. These sensors exploit the change in capacity by changing the electrode distance [5]. The example of the construction of such a sensor is shown in Figure 2.2. The dynamic range up to 1 MPa presented by [5] is in comparison to some types of resistive-based sensors, as their dynamic range is up to several kPa, much higher. On the other hand, the sensitivity of capacitive sensors seems to be much smaller than that of other sensors, only a few percent change of capacity per kPa.

One disadvantage, which may not be regularly problematic, is coupling of electric field generated by a capacitive sensors with other objects, namely metalic parts of robot or grasped objects. This could cause changes in sensor capacity even when the sensor is not touching anything [15]. This issue is not present for other kinds of sensors as they do not generate an electric field as part of their principle. On the other hand, the same principle, influencing the electric field generated by the sensor, can be used to detect objects without touching. This principle was shown in [16] where resistance-based skin was used to measure capacitance changes. Measurement allows detection of human parts from distances of a few cm.

■ Magnetic Sensors

Another approach to build a tactile sensor is to take advantage of magnetism. The sensor is constructed using a permanent magnet inside a soft structure. Under the magnet, a Hall sensor is placed, which measures the magnetic field generated by the permanent magnet. When force is applied to the sensor, the magnet moves and the magnetic field profile changes [17]. To increase sensitivity, an air gap is added to the system. The principle is illustrated in Figure 2.3. Sensors presented in [17] shows saturation when exposed to force of 4 N.
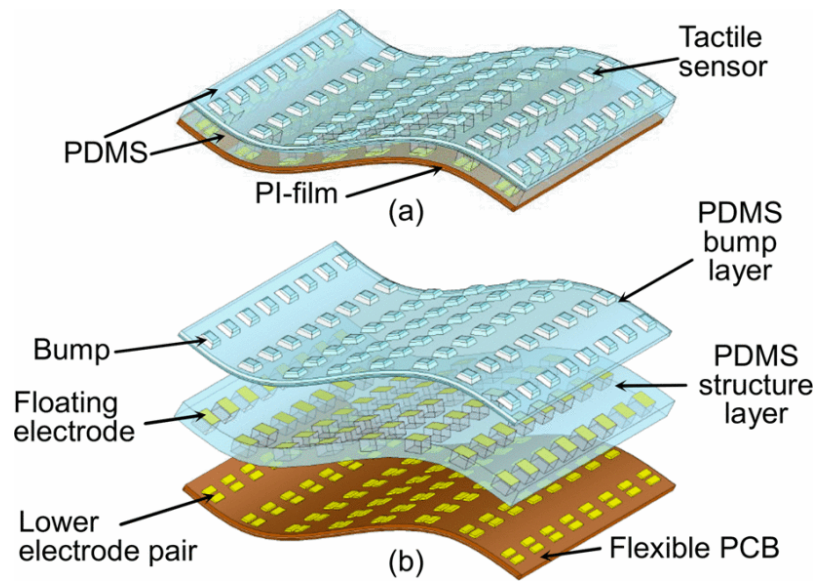
Figure 2.2: (a) The schematic diagram of the artificial skin proposed in [5].. **(b)** The exploded drawing of the sensing array. Figure and caption from [5].
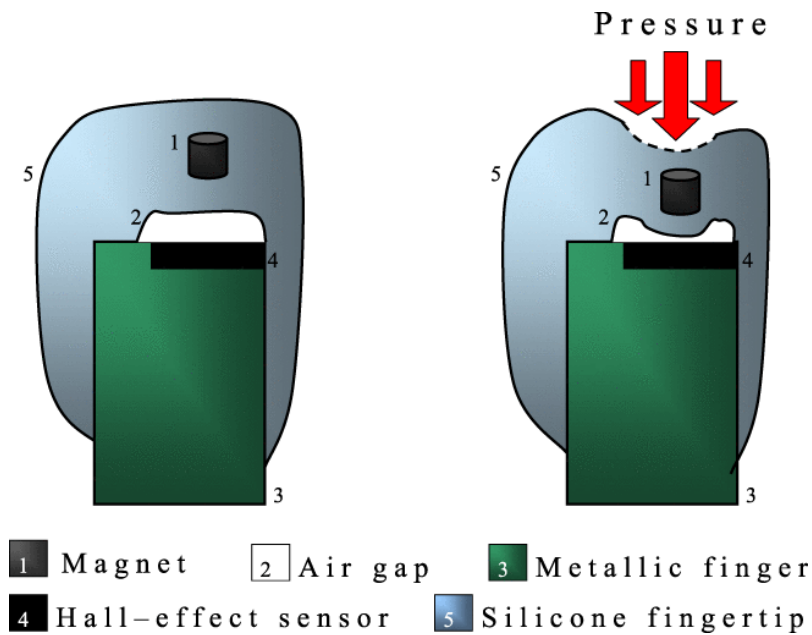
Figure 2.3: Structure of the sensor and sensing principle. Note the presence of an air gap between the silicone shell and the Hall effect sensor, that increases the sensitivity of the system. Figure and caption from [17].

In more advanced sensors such as shown in [7] 3-axis magnetic flux sensors are used. Instead of a magnet, a magnetic elastomer is used. To fabricate such an elastomer, two-part polymer is doped with magnetic micro particles. The mixture is cured between two magnets. The resulting sensor is capable of measuring applied forces up to 2 N.

The magnetic sensors presented in [7, 17] show a lower dynamic range compared to some other sensors. What is concerning to us is the potential sensitivity of such sensors to external magnetic field. On the other hand, sensors are very sensitive, low-cost, and relatively easy to manufacture. Sensor in [17] also is said to be easy to repair in case of damage.

▪ Resistive Sensors

Regarding resistive-based sensors, they often exploit a change in contact resistance. A material showing change in electrical conductivity with applied pressure is referred to as piezo-resistive. This change can be caused by several factors such as the deformation of conductive foams that results in a larger contact area, tunnel resistance, or a change in volume resistance by increasing the number of perlocation paths [3, 8, 9, 18].

The example of a piezo-resistive sensor is shown in [10]. This sensor is based on silicone rubber (PDMS) doped with fine nickel particles. As the sensor deforms, particles move closer to each other and the tunneling conductance increases. This kind of sensor is shown to work up to 2 MPa of applied pressure, while resistance changes from 1 GΩ to 100 Ω. Sensitivity such as this is remarkable, but design an electronic system capable of measuring over such a high resistance range might be challenging.

The alternative way to utilize this kind of sensor is to use so-called microstructures. The PDMS rubber is formed to have a certain shape to form electrodes. On the surface of such electrodes, structures with a size of a few micrometers are made. Usually, we can see pyramids, hemispheres, or cylinders [3, 8, 9]. Two such electrodes are placed on each other in a way that both microstructures face each other. An example of such a structure and sensor response are shown in Figure 2.4. The structures are deformed over each other while increasing the area of contact. PDMS itself is not a conductive material; therefore, such structures are doped with conductive material such as graphene oxide particles, metallic nanowires, or carbon nanotubes [3, 8, 9]. For purposes of tactile grasping and manipulation,
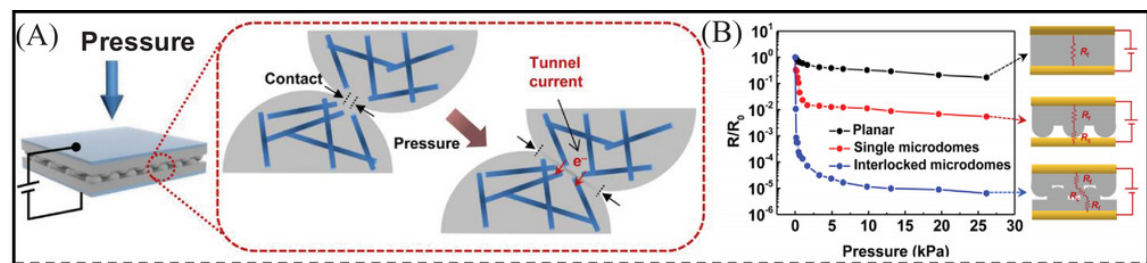
Figure 2.4: Hemisphere structured sensors: design principle and performance. **A)** Schematic of interlocked hemisphere structure. **B)** Resistivity comparison of different surface including planar, single hemisphere and interlocked hemisphere. Figure and caption from [3].

temperature dependency is also important, as the temperature of the grasped object could negatively influence the grasping performance. For a carbon nanotube-doped PDMS-based sensor, the temperature dependence. Sensor resistance increases by 2.5% with changing temperature by $50\,°C$ [9]. As mentioned in [3] sensors based on metallic particles show a significant temperature dependence. The graphene aerogel sensor shows no trend in temperature, which is an advantage [12]. Other research groups seem to show little interest in examining the sensitivity to other units, such as moisture, temperature, or atmospheric composition.

Other sensors we encountered in the literature are using the same principle as our sensor, a change in the contact area to lower the contact resistance. When the sensor is deformed, the pores of the foam are deformed against the electrodes, forming a larger contact area. The illustration of the working principle can be found in Figure 2.5. To some extent, this principle could be counted as piezo-resistance; however, the change is not inside the material itself but on the interface with other material. In [18] polymers such as EVA (ethylen vinyl acetate), PTFE (polytetrafluoroethylene) or silicone rubber were used. Two sensors constructed from these materials were shown to be capable of measuring only hundreds of kPa, while a PTFE-based sensor could measure up to $2\,MPa$ [18].
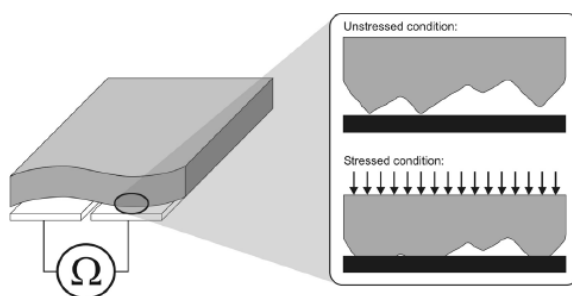
Figure 2.5: Working principle of a resistive tactile sensor cell. Figure and caption from [18].

Our sensor is using a graphene aerogel that is based on the same technology as the sensors in the article [18]. We do not design artificial shapes such as sensors based on PDMS microstructures, but rather exploit the already existing structure of the aerogel. The difference between materials used in [18] and GA is in mechanical properties, since GA is super-elastic.

One of the practical uses of tactile sensors is the electronic skin. In [19] is introduced a method to develop a skin patch based on resistive changes with a relatively small number of electrodes. Thanks to electrical resistive tomography, it is possible to reconstruct the continuous resistance distribution of an electronic skin patch. To evaluate pressure distributions on the skin surface deep neural networks are used. Currently, it is not possible to manufacture a graphene aerogel in a shape with a wide area for use in such a device. Therefore, even though the graphene aerogel shows many interesting features, it is not the best candidate for electronic skin construction.

Hydraulic Sensors

An example of hydraulic based sensor is the artificial finger BioTac, which is frequently used in robotic tasks [1, 20, 21].This finger is a multi-modal sensor. The package contains a temperature sensor, a hydraulic pressure sensor, and an array of impedance-based pressure sensors as shown in Figure 2.6. This variety of sensors increases the amount of information acquired from experiment. From our results which we will discuss in this thesis we believe our sensor is capable of competing with the BioTac finger in parameters such as frequency range and exceed in the dynamic range of applicable pressures. It should be noted that our sensor is still in the prototyping phase, as BioTac is a commercial product.
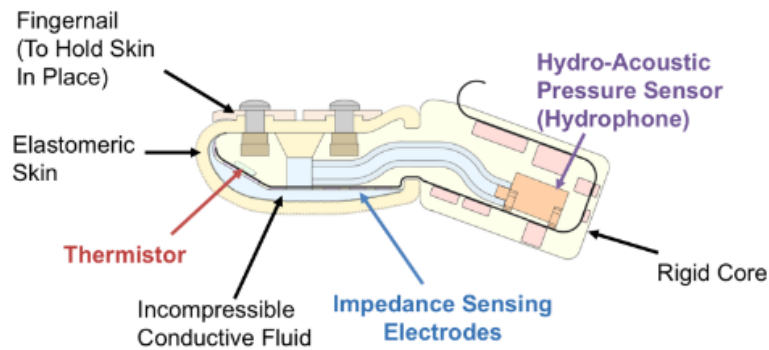
Figure 2.6: The BioTac Tactile Sensor. Figure and caption from [4].

Tactile Grasping

Tactile grasp operations generally consist of surface contact detection, grasp force estimation, slip detection, and force control [22] [20]. To achieve a functional grasp, the processing of several signals can be used. In [22] to detect slips or contact with the material, a simple comparison with constant value is used. Alternatively, in [20] deep neural networks are presented to accomplish such a task. Both methods show remarkable results.

Our grasping pipeline was much simpler than that presented in both articles. We estimate the grasping forces only manually, and in a given time we could not design a functional slip detector. However, the point of implementing the sensor was to show its capabilities rather than implementing high performance grasping pipeline.

Chapter 3

Used materials and software

3.1 Graphene Aerogel and principle of function

As the base material for this sensor, the so-called graphene aerogel (GA), fully named covalently cross-linked graphene aerogel, is used. This sponge-like material is unique from a mechanical point of view, showing what is called super-elasticity. Graphene aerogel can be stretched up to 68% and strained 92%. [11]
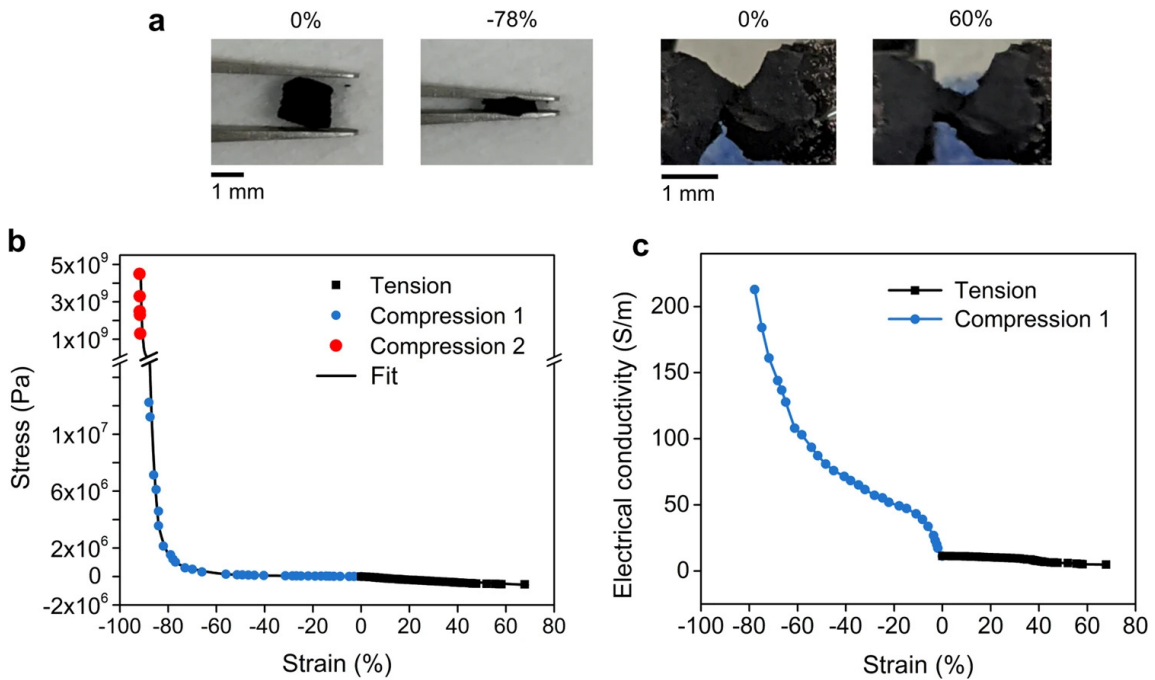
Figure 3.1: a. Optical image of macroscopic samples under compressive (-78%) and tensile (60%) strain. The positive and negative strain is used to distinguish between tensile and compressive deformation, respectively. **b.** Compressive and tensile stress-strain curves of graphene aerogel. The negative stress depicts the opposite direction to the applied pressure. Each point represents an average of N = 10 experiments. Error bars are smaller than the symbol size, see Methods Mechanical testing for full statistics. **c.** Electrical conductivity as a function of compressive (negative) and tensile (positive) strain. Figure and caption from [11].

In addition to its high elasticity and mechanical resilience to normal forces, graphene aerogel shows interesting dynamic capabilities. As we can see in the Figure 3.2 we can see

the graphene aerogel showing very high resonance frequencies, ~24 MHz. To measure the resonance frequency, the following experiment was conducted. Vibrations were induced in the material by a metal rod. To capture such vibrations, the strain-conductivity dependency of GA shown in the Figure 3.1 was exploited. Oscilloscope measurements showed oscillations with an amplitude of $1\,\mu m$ within $50 - 250$ ns [11]. From these experiments, we assume that these mechanical and electromechanical characteristics are promising for the resulting sensor to have a fast response and a wide frequency range.

Regarding dynamic range, tactile sensors usually show some response time. Response time can vary for types of sensors from $0.2\,ms$ to $1\,s$ [3,9]. The graphene-based sensor shows this time very low, $<0.2\,ms$ specifically [12]. This response time was for the GA base sensor measured using 0.1g steel ball dropped from ~ 75cm. The output signal was captured by oscilloscope.
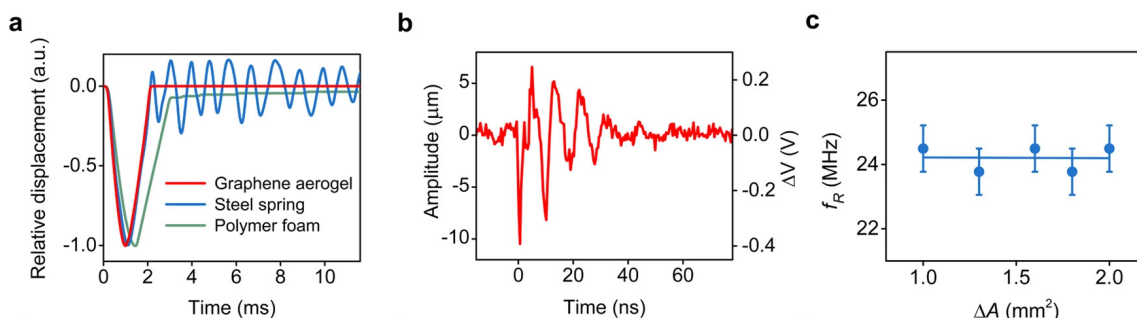
Figure 3.2: a. Comparison of mechanical responses of elastic, plastic materials with graphene aerogel on the impact of a bouncing ball. **b.** The natural resonance of a graphene aerogel block of the size of $2mm \times 1mm \times 2mm$ on the mechanical impact. The amplitude was determined from the voltage response of the sample at a constant current of 100 mA. **c.** Resonant frequency of graphene aerogel blocks as a function of the cross-section area at a constant sample thickness of 2 mm. Figure and caption from [11].

We did not participate in the synthesizing of the graphene aerogel. Its manufacture requires specific tools and machines which are not available in our laboratory. We only order a number of prepared samples from researchers from IoP. However, to become more familiar with the material, we spent a brief time researching this topic. To synthesize a graphene aerogel, first commercially available graphene oxide (produced by Graphenea or XFNANO) is dissolved in deionized water. For $1\,ml$ of H_2O $2\,mg$ graphene oxide is used. The mixture is then sonicated for 30 minutes to obtain a homogeneous dispersion. Then the mixture (30 ml) is sealed in a Teflon-lined stainless steel autoclave of 50 ml size and is annealed at a temperature of $180\,°C$ for six hours. By this hydrothermal process, graphene oxide is reduced and then self-assembles into a 3D hydrogel structure. The hydrogel was then washed with deionized water and freeze-dried in vacuum for 16 hours, resulting in a reduced graphene oxide aerogel. Finally, the aerogel is annealed at $1300\,°C$ in a vacuum furnace to obtain a superelastic graphene aerogel. The final aerogel is then carefully cut and polished using blocks of sandpaper. These blocks tend to break apart when not worked with caution. With this approach, it is nearly impossible to manufacture GAs with precise dimensions. From our point of view, the final part should be optimized for better precision and easier production; alternatively, a way of directly producing exactly shaped GA samples

could be invented.

The manufacturing process is a complex procedure, as it requires vacuumed tools, such as a furnace. On the other hand, microstructure-based sensors require molds with shapes in the range of µm. The manufacture of carbon nanotubes used in such sensors is also not a trivial task [23]. However, we are not skilled enough in material science to compare carbon nanotubes with GA manufacturing.

Next, let us illustrate the working principle of the GA based sensor. Despite the fact that graphene aerogel shows piezo-resistive capabilities, this phenomenon is not mainly responsible for the high sensitivity. According to Figure 3.1, the resistance of the aerogel itself changes very little. Its conductivity varies with full strain for approximately $200\,\mathrm{S\,m^{-1}}$, which corresponds to a decrease in resistivity by $0.005\,\Omega\,\mathrm{m}$. The article [12] reports that the resistance changes are much higher. It was proven that the source of such a sensitivity is the contact resistance [12]. When pressure is applied, the superelastic graphene aerogel deforms against the electrodes. Pores, walls, and struts are deformed and increase the contact area, resulting in lower contact resistance. Because the resistance of the graphene aerogel is much lower than the contact resistance, the contact resistance is dominant [12]. The phenomena of changing contact resistance is then used to measure the applied force.

One more interesting feature reported in [12] is that the contact resistance of the GA-based sensor does not depend on the temperature. The only other work showing this dependency we studied was [9] with regard to carbon nanotube-doped PDMS sensors. In this work, the temperature dependence of this sensor was shown.

The response of GA based sensors will in this thesis shown either as

$$R = R_0 + \Delta R[\Omega] \tag{3.1}$$

or as

$$R = \frac{\Delta R}{R_0}[-]. \tag{3.2}$$

The variable R_0 represents the resistance of the sensors without applied pressure, ΔR is the resistance difference caused by the applied pressure. All these resistances are in ohms. Equation 3.2 is a ratio of resistance change with respect to the base resistance. The ratio is unitless, which is marked by the symbol $-$ in square brackets. The higher the ratio in absolute value for a given applied force, the more significant the change. It shows the percentile change of resistance. This notation will be held in whole thesis. Scaling the resistance response by R_0 is showing as a well-known trend in the field of tactile sensors [3, 12].

■ 3.2 Robot Operating System – ROS

Through out this thesis, we use a Robot Operating System, ROS for short. We will refer to it's functionalities and eventually show applications running under it. In this section we would like to lightly introduce ROS and it's basics.

As the name suggests, ROS is a system that is used to run robotic applications. More correctly to say, it is a set of libraries and tools developed to help with robot operations. It features robot drivers, high-level algorithms, such as visualizations, motion planning pipelines, etc., and introduces framework to link these algorithms into one working piece. It is worth mentioning that this middleware is completely open source [24].

Despite the fact that ROS 2 has been introduced and promoted, we still use ROS 1. We are not yet convinced that the new version is capable to compete with the old one. Regarding the exact version, we used the ROS 1 Noetic distribution, which is the latest ROS 1 distribution. We used this one mainly for its Python 3 support.

What is, in our opinion, more important is the structure of ROS applications. Applications are divided into nodes. The node is a piece of code performing some task. Such tasks might be, for example, data processing, communication with other devices, control, etc. [25]. The nodes can communicate with each other. Under ROS it is done by topics. The topic is a channel through which nodes can broadcast their messages. The node that publishes the data is called the publisher, and the one receiving the data subscriber. When data are published into topic, all subscribers are notified and can respond to the message [25]. Figure 3.3a further illustrates topic-based communication. These messages have fixed
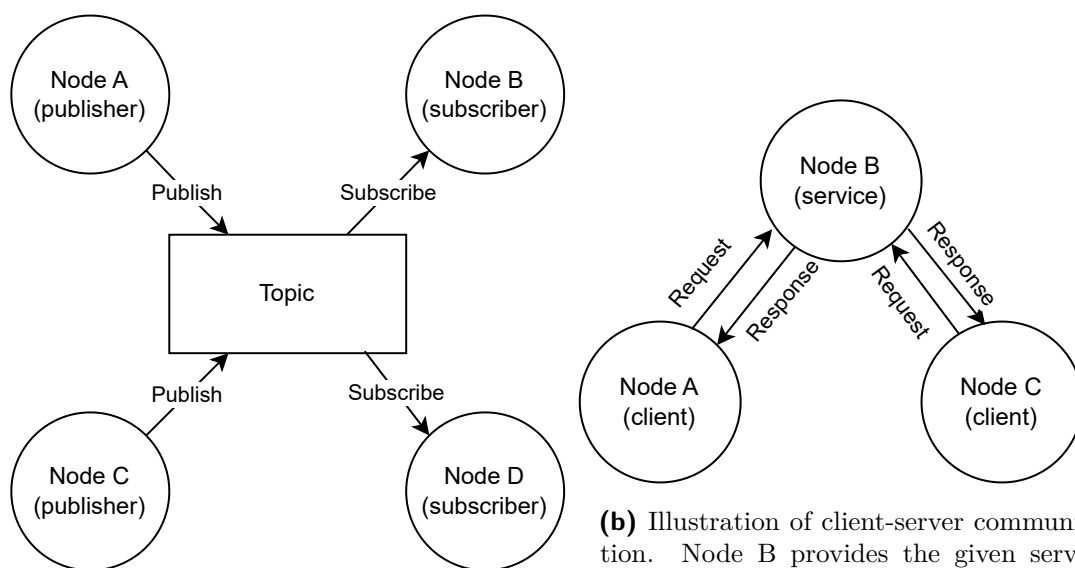
(a) Illustration of topic based communication between nodes. Nodes A and C are, in this case, publishers and, therefore, can publish messages on the topic. Nodes B and D subscribe to a given topic. Nodes B and D receive messages from both nodes A and C.

(b) Illustration of client-server communication. Node B provides the given service. When node A sends the request and node B responds accordingly. The same holds for node C. Node A does not receive any information about node C and vice versa.

Figure 3.3: ROS communication principles illustrations

structure defined while creating a topic and usually one topic serves one purpose. In the base installation of ROS some simple messages are already implemented but the user can define their own as a combination of already created messages. For example, there exists a

message type "Float32" that contains one 32bit floating point number. We can use ROS message functionalities to compose a message type describing outer and room temperature by combining two "Float32" into one message. In our work, we implemented messages for data transfer from the GA sensor [25].

The next communication type in ROS is service-client. This type uses a protocol where the client sends the request and the server responds. The server usually provides some service, for example, computes some function. In a very simple example, client sends a request containing two numbers and server responds with their sum. In our case, we used this functionality for the GA sensor calibration computation. As in topic-based communication, the request and the response from the server have a fixed structure [25]. Figure 3.3a further illustrates the principle of server-client communication.

To communicate with low-level device ROS serial library can be used. This library implements protocol to publish and subscribe for data, time synchronization, etc. By using such tool, fast prototyping with low-level hardware is much easier. To utilize the connection, the node in the ROS system must be running. This node is also implemented by the ROS serial library and its purpose is to communicate with low-level device. It initiates the connection, re-publishes data sent by the low-level device for the high-level application and vice versa. In the current version, UART and Ethernet interfaces are supported.

Chapter 4

Hardware construction

4.1 Graphene aerogel based sensor development and construction

In following chapter we will describe the process of sensor design. We started with development of a sensor composed of a single taxel, as it is less complex than a multitaxel. Since GA is a new material, our procedure was based mainly on trial and error. Also, the stability of GA production is not optimal, and the properties of samples tend to vary from batch to batch.

To measure and evaluate sensors performance we developed our custom electronics described in the Section 4.2. This system allows us to read sensor resistance and send measured data to the PC with a running Robotic Operational System. The ROS interconnection allows easy data logging, time synchronization with other devices connected to same system, such as robotic manipulator Kinova Gen3.

4.1.1 First generation

The development of our sensor was based on the design we were provided from IoP with. The schematics of the prototype is shown in Figure 4.1. As substrate material, we used generic printed circuit board (PCB). This material is cheap, provides firm mechanical support, and is already equipped with a conductive layer to create electrodes. The GA was placed on top of two plate electrodes. To secure it in place, conductive carbon adhesive was used. The adhesive was cured on a hot plate at temperature ~70 °C. Adjusting the heating time allows one to adjust the resistance of the sensor R_0. This resistance was set at approximately $200\,\Omega$. The GA was then covered with a thin nitrile sheet (obtained from a cut nitrile glove). We will refer to this cover as the primary cover. This construction shows major defect. The resistance R_0 of the sensor shows high hysteresis. Figure 4.2 shows the experiment during which this behavior can be observed. Based on our experiment in Figure 4.2 we assume the problem is in air pressure inside the sensor. The chamber formed by GA under the primary cover was not hermetically sealed. When the sensor is pressed, all of the air contained under the primary cover is pressed out from the sensor. After the release, the GA starts to return to the original shape. During this process, the primary cover draws air back inside. However, due to mechanical imperfections, the sensor stabilizes at a different pressure value than before pressing. This results in a very chaotic value R_0 and a very high hysteresis. To support our theory, we punctured several holes in the primary cover with a needle. Air can now flow through the primary cover more
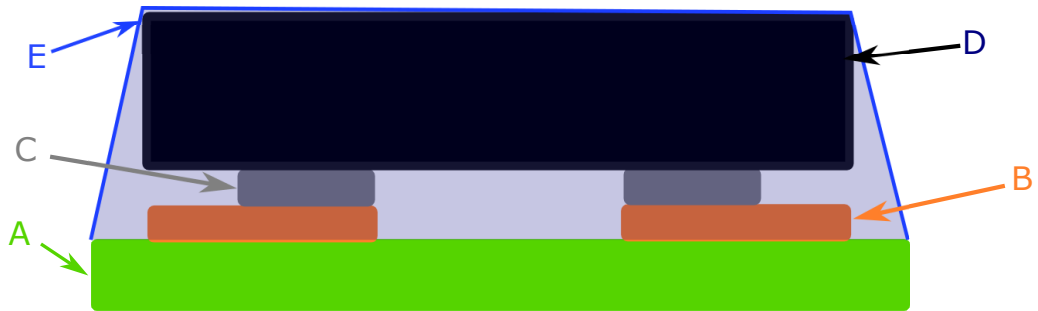
Figure 4.1: Schematics of first sensor design. Layers are not to scale. A) PCB substrate, B) copper plate electrodes, C) carbon adhesive, D) graphene aerogel, E) primary cover.
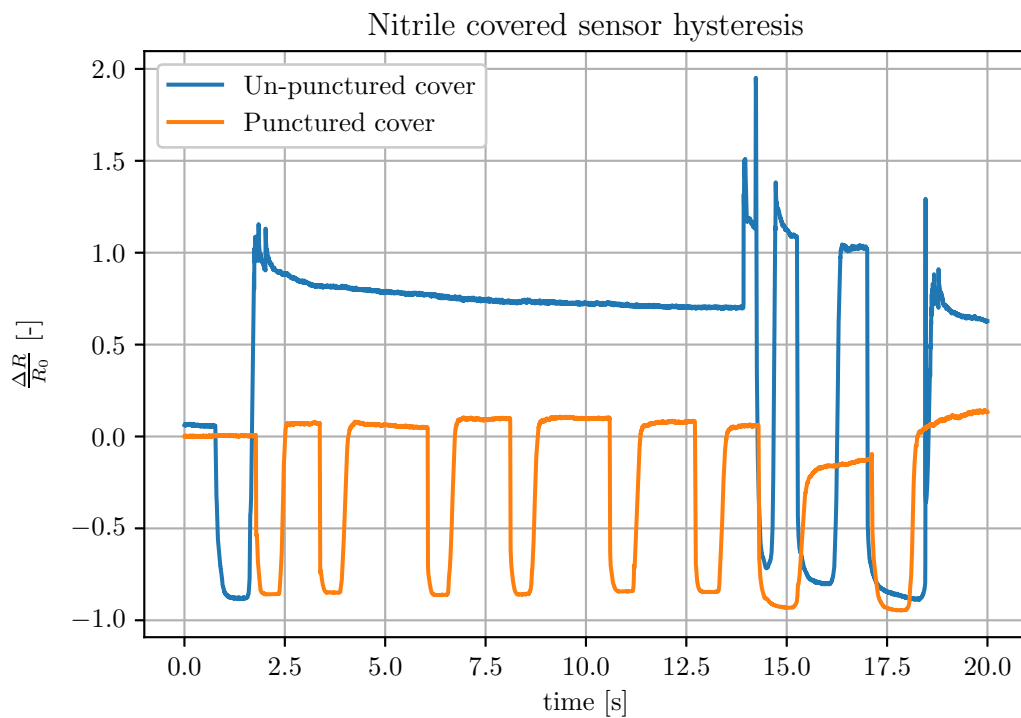
Figure 4.2: Comparison in performance between punctured and un-punctured graphene sensor, both sensors were pressed and released multiple times. Un-punctured, blue, sensor shows significant hysteresis >100%, punctured sensor, orange, shows hysteresis much lower.

freely and allows for easier pressure stabilization. We compared the performance of the same sensor without and with punctured holes. The punctured sensor shows a much lower hysteresis and acts much less chaotically as shown in Figure 4.2.

4.1.2 Air pressure influence elimination

In the previous section of this chapter, we observed the issue of high hysteresis and chaotic behavior of a nitrile-covered sensor. In this section, we will elaborate on this topic and introduce our solutions. To eliminate sensor hysteresis due to pneumatic pressure equalization, we invented several possible approaches.

First, to hermetically seal GA under the primary cover. This solution would not allow any volume of atmosphere to leave the cover. In this scenario, inert gas, such as argon, could be used to improve the chemical stability of the sensor. Alternatively, vacuum could be utilized. However, in our conditions, it is impossible to create such encapsulation. Next, when the sensor is pressed, the pneumatic pressure inside would build accordingly. This would cause greater reversing forces, lowering the sensitivity of the sensor. Finally, any piercing damage to the primary cover would cause the sensor to fail, as the cover would no longer be hermetically sealed. For these reasons, we abandoned this approach.

The second approach incorporates exactly the opposite to the first one. Instead of keeping the sensor sealed, we would allow air to flow freely through the substrate or through the primary cover. This approach is the next logical continuation of the experiment shown in Figure 4.2. In contrast to the first solution introduced, this method was possible to experiment with under our conditions. We decided to follow this variant.

To allow air to flow through the substrate, we milled a hole under the GA ~$2 \times 2mm$. However, after sensor construction and several press and release cycles, the GA inside broke apart. We assume that the GA broke after being pressed against sharp edges of the drilled hole in combination with uneven deformation of the material. Some parts of the GA were pressed through the drilled hole, and others against the electrodes. Alternatively, we ordered a PCB with several holes in the electrodes and substrate. These holes were 0.4 mm in diameter. Unfortunately, most of the holes got clogged with glue when the primary cover was attached. Also, the holes directly under the GA seemed not to work properly. Although GA is porous, it does not appear to be permeable. The remaining holes were unable to provide sufficient air flow. We decided to abandon this method.

Alternatively, allowing air to flow through the primary cover was more successful. For this construction, we replaced the nitrile sheet as the primary cover with medical tape, which is generally used to attach tubes and infusions to the patient. This tape is porous, permeable, flexible, and resilient. We tested the sensor for the hysteresis. The result is shown in Figure 4.4. During the experiment, a cobblestone was pressed and released. This cycle was repeated ten times. In the figure we can see the systematic decrease of resistance R_0 after each release. After each release, the resistance recovered very slowly to the original value. Recovery time was on a scale of hours.

Based on our observation we assumed the reason for this behavior is the adhesive on the
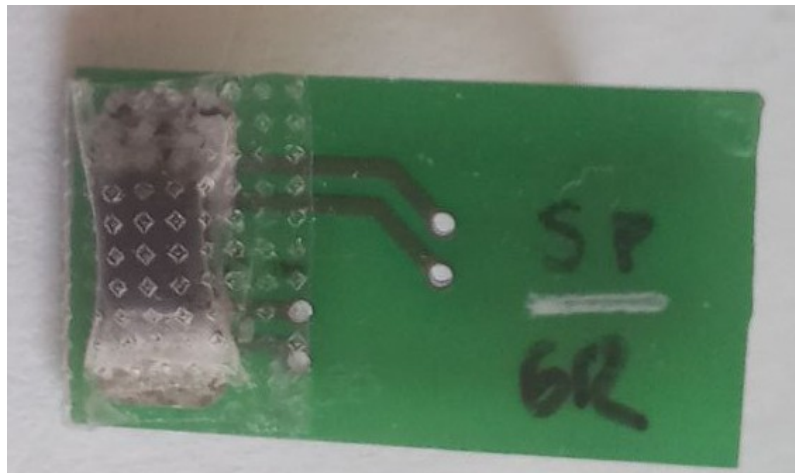
Figure 4.3: Sensor covered by porous medical tape.

tape. When the sensor is pressed, the tape is glued to the surface of the PCB by the tape adhesive. The revering force generated by GA is too low to unstick the tape quickly. The tape is eventually fully unstuck, but this process is simply too slow to be used.

We had to find a way to remove the glue from the tape. The adhesive proved to be quite resilient. The only two solutions that we found capable of cleaning the tape were C6600 thinner and technical benzine. We conducted the same test as with the unwashed tape cover sensor. The result of the experiment is shown in the Figure 4.5. Sensors that use this modified tape as primary cover exhibit low hysteresis as shown in Figure 4.5. This version of the sensor showed the best performance we found and so it was used in future work. The sample used in Figure 4.5 shows a lower sensitivity. On the basis of our experiences with GA we assume that it is caused by applying too much pressure to the aerogel while covering the sensor. Other sensors based on this construction show much higher sensitivity, as shown in Chapter 5.1.2.

◼ 4.1.3 Moisture dependency

It is not uncommon for sensors to be influenced by other variables than those that are meant to measure. Strain gauges, for example, which are mainly metallic wires, also show temperature dependence [26]. When conducting experiments with the sensor sample covered with cleared porous medical tape, we noticed strange behavior while the sensor was gently touched with the bare finger. The resistance began to increase with an approximately exponential course and decreased as the finger was removed. We suspected that the moisture on the finger is the reason for this behavior. To test this hypothesis, we exposed the sensor with increased moisture. After approximately $50\,\mathrm{s}$ we stopped the exposition. We observed the sensor response, which is shown in Figure 4.6. The sensor over the coarse of tens of seconds increased the resistance value by 14%. This value is relatively high for our purposes. On the other hand, it might be possible to design a humidity sensor based on GA. The sensor might also be able to detect other molecules, such as CO_2, but this was not the aim of this study. Our task was to eliminate this parasitic property.
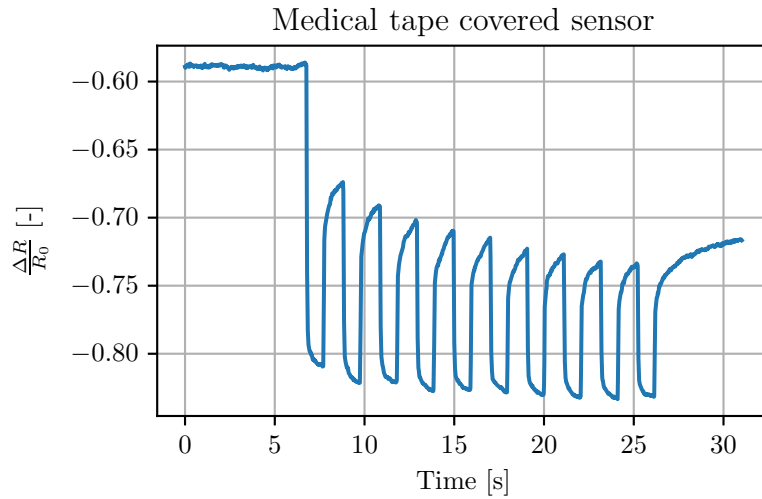
Figure 4.4: Decrease of value R_0 while repeatedly grasping cobble stone using gripper Robotiq 2f-85.
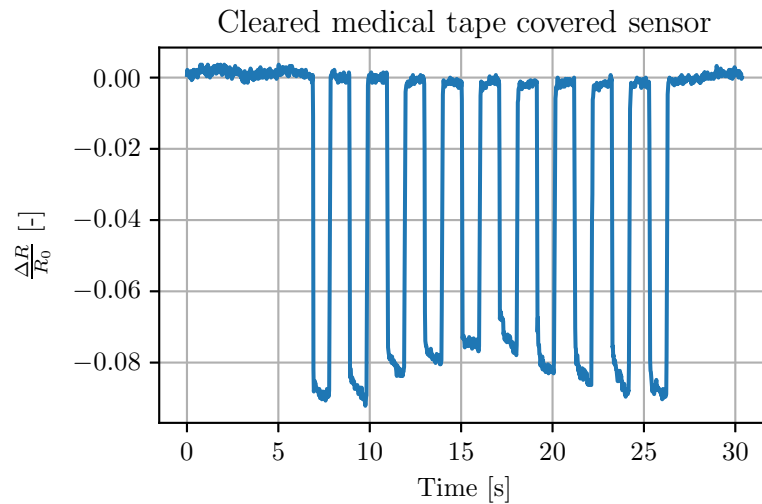
Figure 4.5: Performance of sensor using cleared plaster while grasping cobble stone using gripper Robotiq 2f-85.
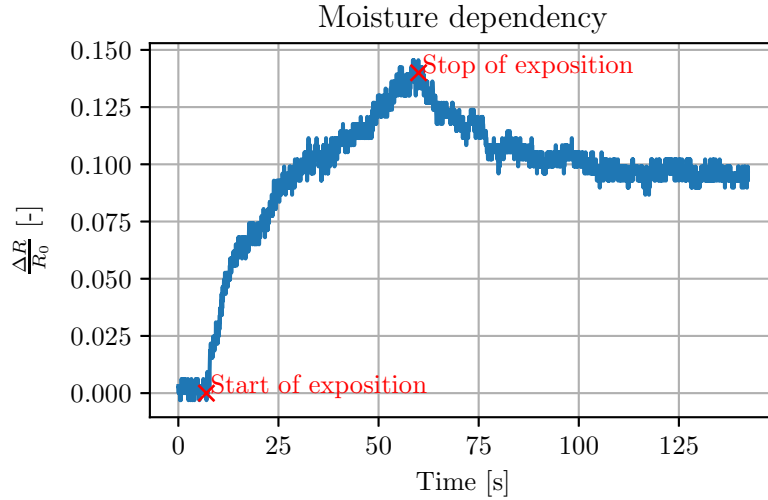
Figure 4.6: Record of humidity dependency of graphene aerogel based sensor.

To mitigate this phenomenon, we employed the secondary cover made from nitrile sheet. This cover cannot be permeable and should be flexible enough to not damp the sensor sensitivity. The secondary sheet should protect the sample from direct touch of other bodies and, at the very least, lover the influence of surrounding atmosphere.

However, as shown in Figure 4.2, when the sensor is enclosed in a not completely sealed chamber, excessive hysteresis is present. To avoid this issue, we constructed the chamber created by the secondary cover much larger than the GA. We attached the PCB to a plastic mount we used to attach the sensor to the Robotiq gripper. Then we covered the whole area with nitrile cover. When the sensor is pressed, air is pushed to other parts of the formed secondary chamber. Because the volume difference is very low with respect to the volume of the secondary chamber, the pressure change is also very low. This result has very low hysteresis and the sensor's value is no longer affected by direct touch of wet surfaces. Since we cannot completely seal the sensor (our laboratory does not contain devices capable of such hermetic sealing), we assume that the atmosphere under the secondary cover is not constant. The inner air humidity can change as the surrounding changes. The secondary cover protects against direct moisture excitation and potentially slows down the change of inner atmosphere inside of the sensor.

▪ 4.1.4 Long time stability

One of the good features of any sensor is the long-term stability of the offset or base value (in our case R_0). Otherwise, the detection of any touch or pressure becomes challenging without any calibration. In our case, we have observed exactly the opposite. Over a long period of time, when sensors were stored, significant drift R_0 occurred. This drift was caused by several tens of percent over a coarse of multiple hours. To ascertain the origin of such drift, we conducted long-term monitoring of two technologically same sensors (sensors A and B). We used two in case the derivation would be different for each sensors. These sensors were left to drift for numerous hours. We observed this time derivation as shows in

Figure 4.7.
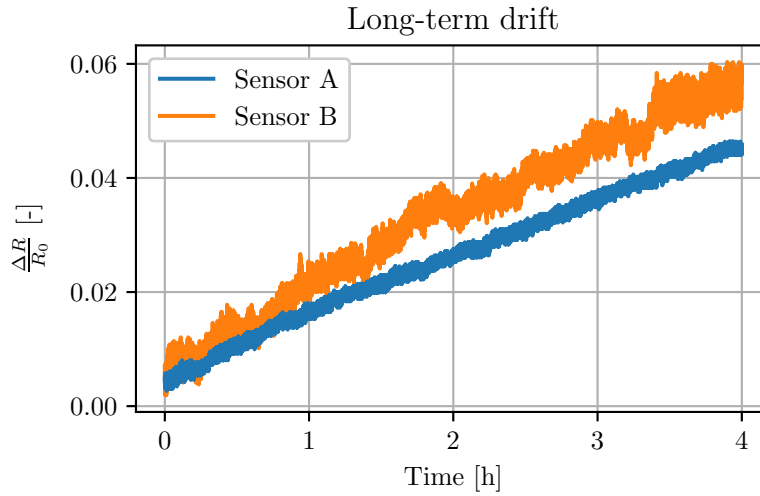
Figure 4.7: Drift of two independent graphene sensors using carbon glue over a 4 hour time.

In Figure 4.7 we can see both sensors drift in same pace. After four hours their difference is $\sim 1\%$ which is very little difference. From this we assume the drift is not an error or malfunction but systematic failure of design. We tried to compare our data with change of atmospheric pressure measured by local weather station; however we observed no correlation.

By listing and filtering possible causes, we located the main source of the error. The conductive carbon adhesive used to attach GA to the electrodes seemed to have a major impact on this feature. As mentioned above, it is possible by exposing to temperatures $\sim 70\,°C$ adjust the value R_0. We assume the carbon adhesive was not fully stabilized. We conducted several experiments in search for possible replacement.

First, we tried an alternative adhesive. A silver paste provided very nice stability over several hours. The disadvantage of such glue is that it must be applied in very small doses because of its high electrical conductivity. Even at small doses, the resulting R_0 is in units of Ω. For this reason, we decided to measure with Agilent 34401A until we develop more precise electronics. In Figure 4.8 we can see the silver paste adhesive provides almost perfect stability. The resulting sensor shows a difference lower than 0.1% of R_0. On the other hand, for the low impedance nature of the resulting sensor and manufacturing difficulty, we decided to look for another solution.

In search of an alternative attachment method, we tried to solder the GA to electrodes. We placed the GA onto a very small bit of solder paste on the PCB and used a hot plate to solder it. The GA was shown to be solderable, as the molten solder got capillary sucked into the structure. The resulting contact resistance was, similarly to the silver adhesive, in units of Ω. Furthermore, the cooled solder formed a rigid structure inside the GA. When pressure was applied to the sensor, the structure did not allow the GA to deform without tearing. This caused the GA sample to slowly tear apart after a few iterations of compress and release. For use in tactile sensor scope of interest, this method is highly inconvenient,
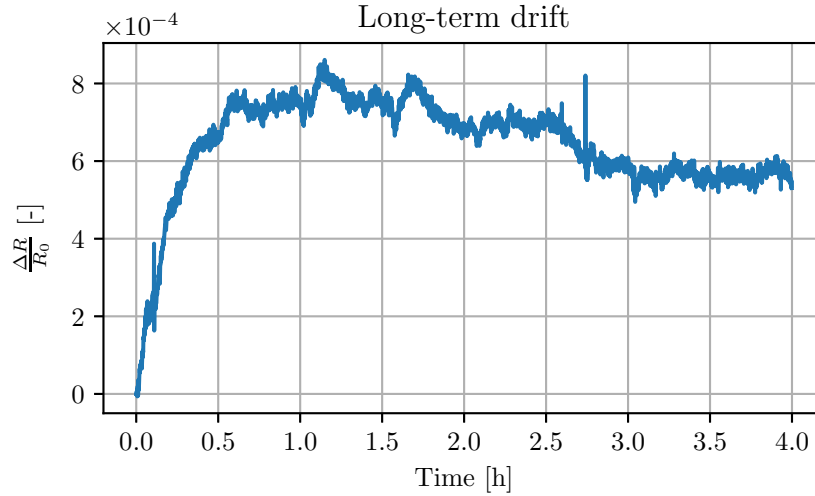
Figure 4.8: Long term drift of GA sensor's R_0 using silver paste adhesive.

and so we abandon this approach. On the other hand, this technique could be utilized in some different usage of GA should anyone research such a topic.

Finally, we tested the option of using neither adhesive nor solder. In this case, the GA is held in place by friction forces between the electrodes and the surface of the sample. The primary cover presses the graphene aerogel against the electrodes. The pressure provided should not be too large, otherwise the sensitivity of the sensitivity of the sample significantly decreases. The result of the drift experiment is shown in 4.9. The mean sensor value remained in the range of ~ 1.5%, which is worse than the performance of the silver paste. In contrast to the use of silver paste, this method appears to be easier to use. When silver paste is used, a lot of attention must be paid not to apply to much of this adhesive, else the resulting resistance is too low. On the other hand, the sensor without any adhesive also shows a relatively low impedance, in the range of ~5 Ω to ~30 Ω. This resistivity range is similar to that of sensors utilizing the silver paste. Nevertheless, we find this solution to be the best we invented and so we used it in future designs.

As we found, time stability has a limit in the range of several days. After a few days the value R_0 of the sensors changed without any adhesive changes in units of percent. From our observations, we derived the sensor's reaction to the atmosphere composition. In the above sections, we showed the sensor's dependence on moisture. To support our thesis, we reached the IoP, where we let GA sensors drift in an inert argon atmosphere over the course of 48 hours. Sensors were constructed using carbon adhesive and solver paste. Both were cured on a hot plate at 70 °C. Figure 4.10 shows the observed drift. The drift was measured using a hand multimeter. Deviations shown in Figure 4.10 are so low and nonsystematic that they are most likely caused by different contact resistance between multimeter probes and sensors.
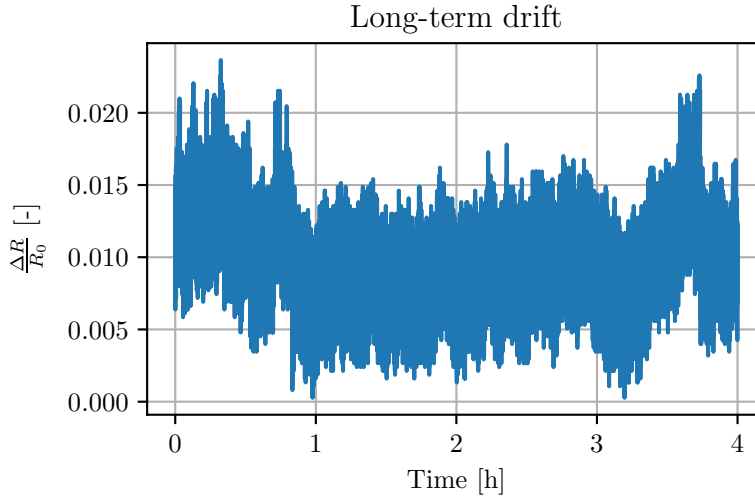
Figure 4.9: Drift of sensor without conductive adhesive nor solder over four hours.

4.1.5 GA resistive matrix

For tactile grasping, one sensor usually does not provide enough information, especially when the sensor has only a few squared millimeters, as is in our case. We would need to cover larger area of the gripper's finder with taxels. Tactile matrices are used in literature. These are constructed as a mesh of contacts that form rows and columns. Between them, typically one piece or stripes of material such as EVA (Ethyl Vinyl Acetate) is placed [10, 18, 27]. Unfortunately, this approach is not possible in our case. The manufacturing process of graphene aerogel allows to create blocks only a few millimeters in dimensions. Any larger piece is too unstable and tends to break down, according to IoP researchers. We decided to try to construct such a matrix as a combination of discrete taxels, each composed from one GA sample. A similar approach can be found in [9]. In article [9], the tactile array is constructed as individual sensors without any interconnection. We find this approach inappropriate with respect to the number of switches needed to read such an array.

Because we are making graphene sensors by hand, without any precise machinery, certain percent of the sensors fail in production. Graphene aerogel is very light and is caught on various surfaces by static electricity, which complicates the manufacturing process. If we construct the matrix in one piece, in case of one failed taxel, the whole product would go to waste. Instead, we developed system of discrete taxels, which are embedded into matrix using connectors. If one sensor fails, it can be easily replaced with a functioning one.

The disadvantage of this method is the increase in mechanical complexity as well as the increase in the number of connectors. More connectors bring more parasitic resistance which needs to be compensated for for precise measurement. To mitigate such resistances, we designed a matrix for 4-wire resistor measurement. In Figure 4.11 we show schematics of matrix 2×2 to illustrate the function.

We designed a system that allows you to build a matrix up to size 4×4. To enhance mechanical structure, supportive mesh was 3D printed. The mesh prevents taxels in

23
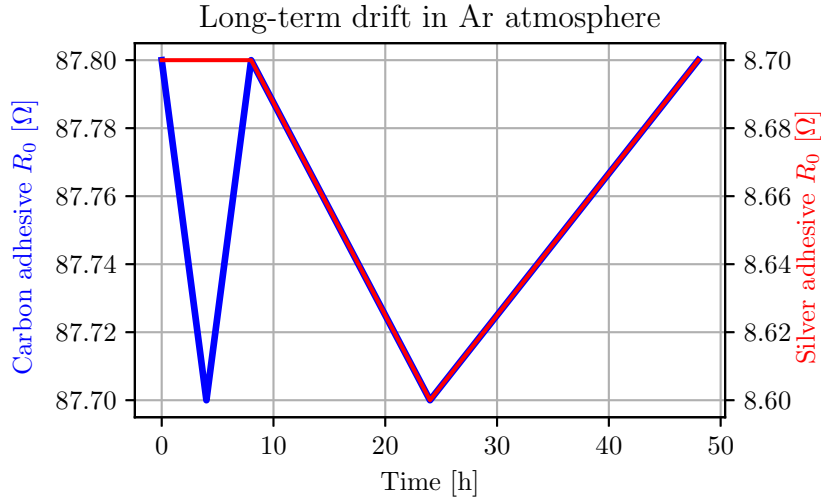
Figure 4.10: Drift of sensors using conductive adhesives in argon atmosphere

connectors to move, bend, or twist. The entire sensor is then screwed together with gripper finger attachment using M2.5 screws.

Each taxel is constructed using a PCB with comb electrode. On the opposite site, an SMD 2×2 1.27 male connector is soldered. During the manufacturing process, this connector can be used to monitor the sensor's impedance. The graphene aerogel is placed on top of the comb electrode and secured in place using the same cleared porous tape as shown above. The comb electrode allows easier construction. A sample of GA can be placed almost everywhere on the electrode surface and contact between both electrodes is established.

When resistors in tactile matrix are measured using a simple method of selecting a given row and column, measuring current actually flows through all resistors. This current is called the cross-talk current. There exist several solutions to cancel such currents, but for reasons described in Section 4.2.4 we were not able to compensate for such currents.

If we wanted to create a multi-taxel sensor, we needed to find other ways of incorporating them. We observed that we can arrange sensors into line, column, or diagonal without being restricted by these cross-talk currents. By using multiplexer-based electronic we can measure each taxel without an issue. This problem is described in more detail in Section 4.2.4. The final construction can be seen in Figure 4.12.

■ 4.1.6 Summary

We developed different variants of functioning sensors using graphene aerogel. Table 4.1 summarizes the technologies tested. During our research, we discovered the moisture dependence of the GA samples. We tried to reduce the drift of R_0 as much as possible by eliminating the conductive carbon adhesive. This adhesive appeared to have a significant impact on the stability of the sensor at time when used in a regular atmosphere. As
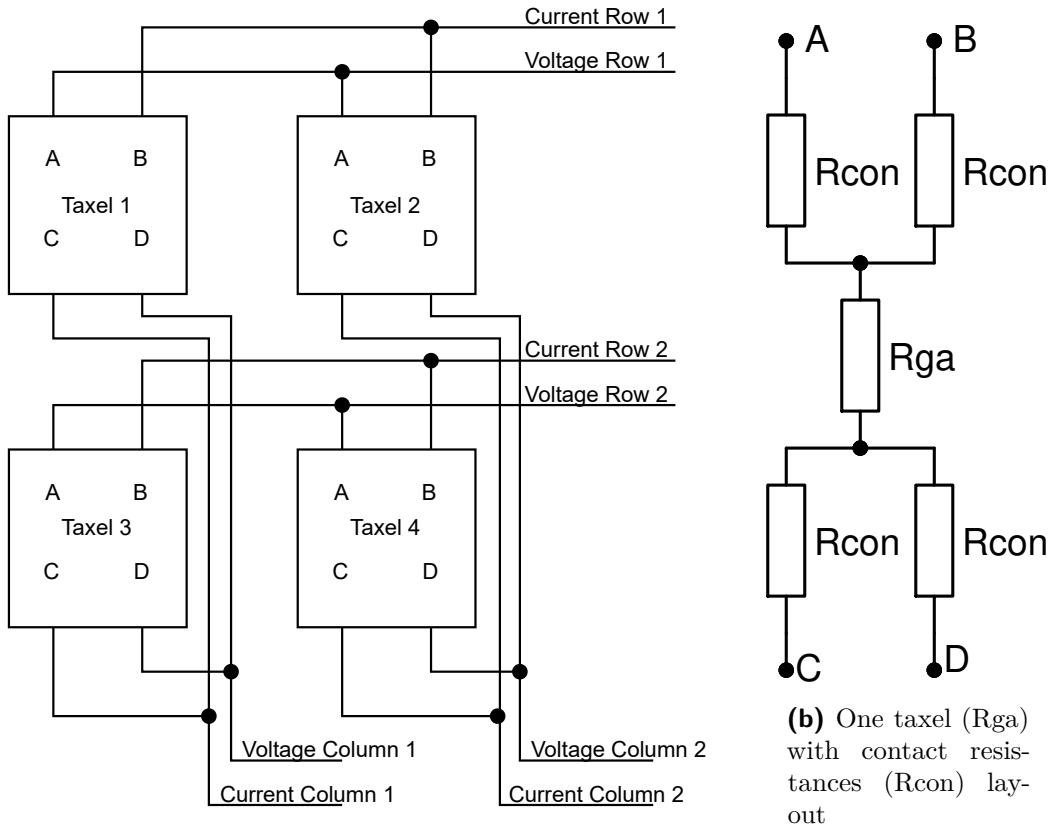
(a) Schematics of tactile matrix 2×2

(b) One taxel (Rga) with contact resistances (Rcon) layout
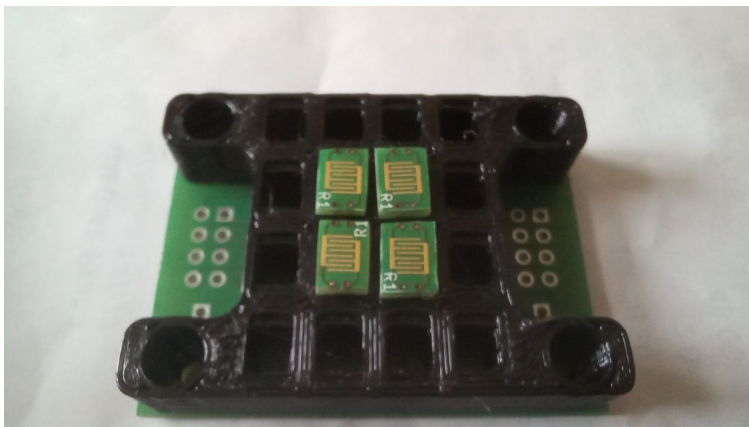
(c) Physical construction

(d) Taxel item (1 CZK for scale)

Figure 4.11: Matrix schematics designed for 4-wire measurement.
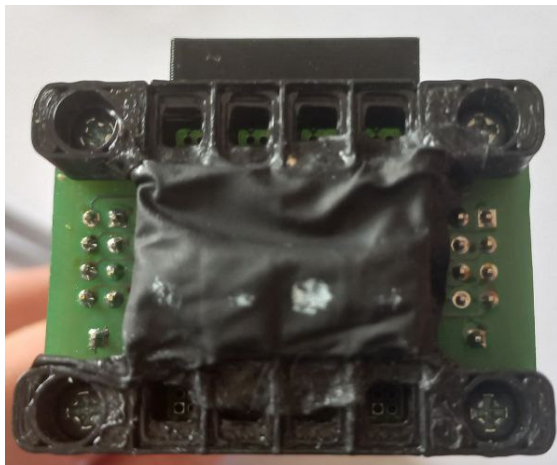
(a) Front view, white dots on nitrile cover marks position of taxels
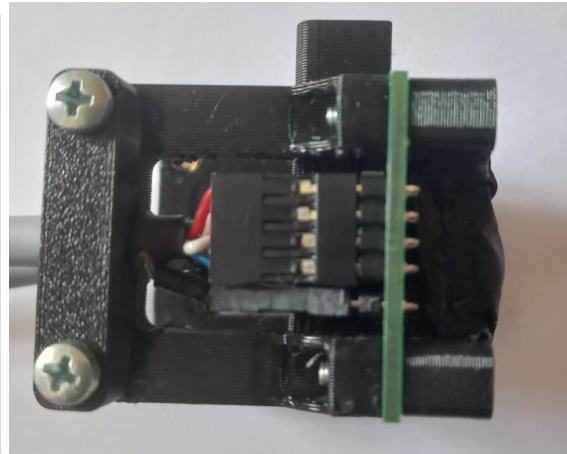
(b) Side view. The sensor is electrically connected to two 8 wire shielded cables. Cable is held in place using plastic holders.
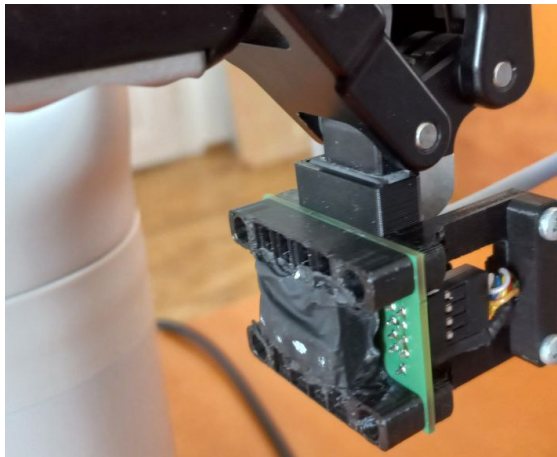
(c) Sensor mounted on gripper Robotiq 2f-85 for which mount was designed.
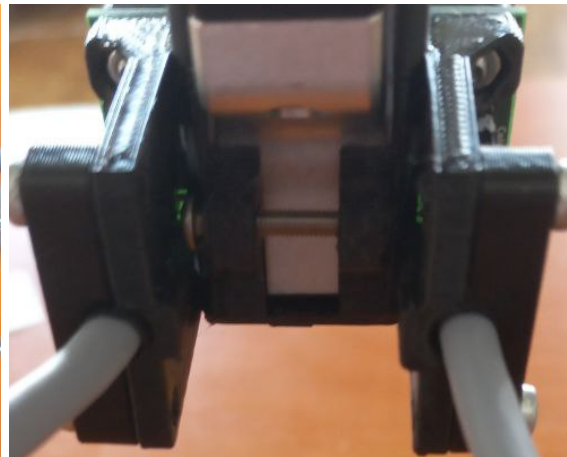
(d) Rear view, screw can be used to tighten the mount on the finger.

Figure 4.12: Final sensor construction.

shown in experiments conducted on the IoP, if placed into an inert atmosphere, the drift terminates. Since we cannot completely hermetically seal the sensor to maintain a stable atmosphere, the deviation R_0 persists. We slew it down by covering the sensor with a secondary cover and sealing the sensor as much as we could. Our sensors seem to be stable in the range of days. In case of usage in robotic application, some re-calibrating algorithm is needed. Over all, our design is not perfect and further research in this area would be needed to turn GA sensors into a commercial industry grade product.

Technology	Advantages	Disadvantages
Non-permeable primary cover	None	High hysteresis and chaotic behavior
Permeable primary cover	Low hysteresis	GA exposed to outer atmosphere (humidity dependency)
Permeable primary cover and nonpermeable secondary cover	Low hysteresis, Influence of atmosphere lowered	Increased mechanical complexity
Carbon conductive adhesive for GA connection	Higher impedance of the sensor	Significant resistance drift in time
Silver conductive adhesive for GA connection	Very low drift of resistance over time	Low sensor impedance, need for precise doses
Soldered GA connection	Simple manufacture	GA breaks apart, low impedance, not functional for tactile sensor
No adhesive for GA connection	Low resistance drifts, simple manufacture	Low impedance sensor

Table 4.1: Summary of used technologies, their advantages and disadvantages.

4.2 Design of measurement electronic system

In this section, we introduce our custom-designed reading electronics. Our demands for the reading pipeline were that it should be capable of reading multiple sensors at once. Next, we wanted it to be able to adjust the signal path for each individual taxel for the best performance. As we plan to use this device in robotic application, the stream of measured data into the Robotic Operational System (ROS) is mandatory. Finally, we paid attention to lowering the noise brought into a pipeline by other electronics such as communication and power management integrated circuits.

In this section, we show the most important parts of the design. The explanation of every particular component and its purpose would be too exhausting. Complete schematics can be found in the attached files.

4.2.1 Basic principle

Since we find graphene-based sensors relatively sensitive, we did not need to use Wheatstone's bridge circuits. Such a circuit is used to read directly ΔR rather than $R_0 + \Delta R$. On the other hand, the output of this circuit is highly nonlinear when only one sensor is used and requires balancing to function properly [26].

Instead, we utilized a 4-wire measurement. In our design, we need to compensate contact resistances of connectors. These resistances are in a range similar to the impedance of our sensors and their deviation would ruin the reading precision [26]. Moreover, thermal dependence of resistance of the copper wire, from which cables are constructed, could ruin the temperature properties of the GA sensors.

This method is based on the usage of a constant current source and an instrumentation amplifier. Instrumentation amplifier is a component amplifying voltage difference on it's inputs, which can be used to read voltage on one particular component. The constant measuring current generated by the current source is passed through the measured resistor. Passing current creates voltage over the resistor. This voltage is then measured using an instrumentation amplifier. If the instrumentation amplifier input leads are connected as close as possible to the physical body of the sensor, only the voltage across the sensor is sensed. Any other parasitic resistances, such as resistance of connectors, are ignored. The influence of connectors by which the amplifier is connected is also mitigated, as almost no current flows through them. The input currents of the reading amplifier are very low and can be ignored [26].

4.2.2 Complete circuit

In this section we show the general simplified schematics of the developed measurement pipeline. Separate parts are described in detail in the following sections of this chapter. In real implementation, we decided to divide the system into several modules which are interconnected to one another. The reason to this is that some parts of the design are repeating and this form of approach makes repairs, design updates, and overall development easier. In Figure 4.13 there are two sets of blocks. They are labeled as "left" and "right".

Figure 4.13: Block schematics of the system (blue arrows – analog signal of tactile information, green arrows – digital control signals, red arrows – analog signals of measurement diagnostics.)

We developed the system in a way that would allow us to equip both grippers with tactile sensors. For each finger, one multi-taxel sensor. To keep pipeline reasonably simple, we decided to make some parts twice rather than inventing a system to read both sensors at once. Needless to say, this approach keeps sensors on each finger independent. Finally, the developed board used Teensy 4.1 contains two separate 12 bits analog-to-digital converters, which can be read synchronously.

As mentioned, the heart of the measurement pipeline is the Teensy 4.1 development board. This controller continuously selects the taxel which is to be measured, sets proper gain, and reads analog values. Then communicates over 100 Mbit Ethernet with the master computer running ROS thanks to the ROS serial library.

To save a number of pins dedicated to control of the pipeline we used several shift registers with latching output to create a daisy chain communication structure. By this utility we can set each taxel to be measured and signal amplification. To drive the shift registers we exploited the SPI hardware interface of the Teensy board. The SPI communication principle is based on shifting registers, so even though it is not intended to be used in this way, it is possible. We used the MOSI pin of the SPI interface to feed data into a chain of shift registers. The clock signal of SPI was used to synchronously shift registers. Finally, we used one CS pin to control latch to output synchronously on every register with rising edge of the signal.
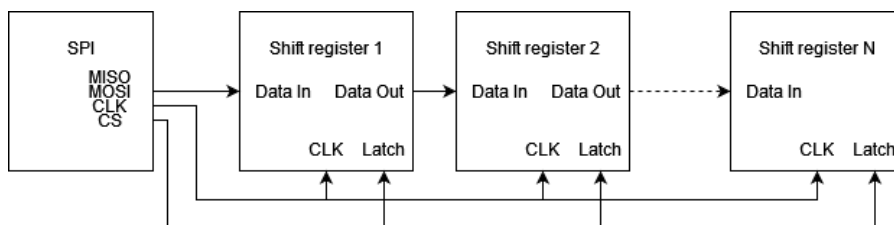
Figure 4.14: SPI interface exploit illustration

The analog part of pipeline is powered from 5V instead of 3.3V as processor on Teensy board is. For control signals to work properly we used 74HCT08. This integrated circuit consists from four two input AND gates. By short-cutting inputs fro each gate we create

YES gate. Since it is HCT type of circuit, logical high level is at 2V, which is low enough for 3.3V logic to safely trigger [28]. We could use more straight forward approach and use all logical circuits in HCT variant, or at least use YES gates directly. Unfortunately, these types of integrated circuits were commercially unavailable in time of design.

With respect to different supply voltages for the analog part and Teensy 4.1 board, protection resistors are used. Whenever the voltage at the output of the analog electronics exceeds the expected level, the current starts to flow through the substrate diodes of the mosfet transistors, forming the input stage of Teensy 4.1. The protection resistors limit this current to save values to prevent permanent damage to the device.

■ 4.2.3 Supply voltage and noise reduction

Measurement chain can be powered in two modes. Straight from USB through Teensy board or from any DC voltage source in the range [6.5V, 36V]. Since the USB interface is not used for communication, we wanted to provide the option to not use the USB connector at all for cases when it is not practical.

In case of powering from the voltage source, the supply voltage is adjusted to 5V using circuit TSR 1-2450. This circuit implements a switching step-down voltage regulator. On the one hand, the power conversion is very efficient (up to 96%), on the other hand, the switching nature of the circuit produces noise [29]. To power reading electronics, such noisy supply voltage is not suitable as the noise would affect the measured signal. The manufacturer shows in the data sheet [29] an LC filter to filter the input voltage to protect the source of the supply from noise (regulation EN 55022). We placed this LC filter on the output to reduce the noise as shown in Figure 4.15.
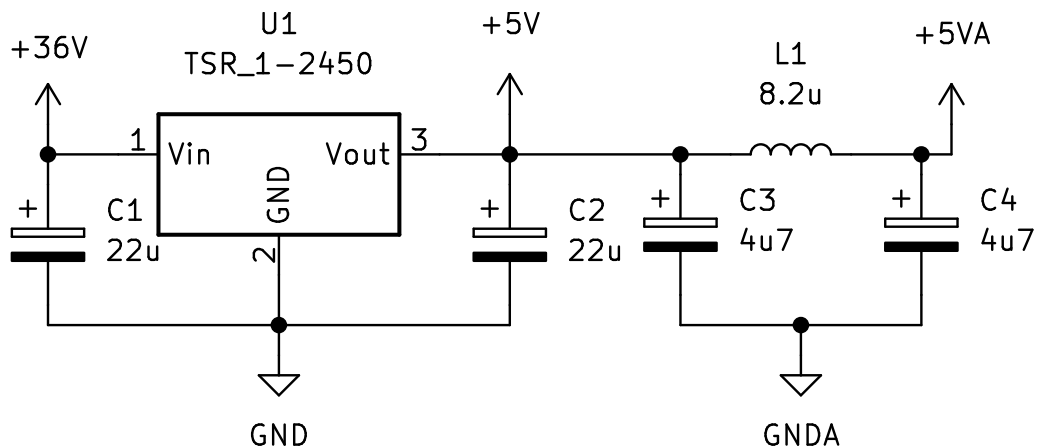
Figure 4.15: Analog supply voltage filter to reduce noise generated by TSR1-2450. In components values letter 'u' stands for μ.

Regarding other sources of noise, our design combines high-speed digital circuits such as microcontrollers or communication interfaces. Such devices produce noise in the supply voltage which is usually caused by fluctuation in current consumption of the device. Since no voltage source is ideal, such current changes result in a voltage decrease due to the inner

resistance of the supplying voltage source. Shifting the supply voltage then influences the analog signal obtained from the measurement chain.

The fist protection to this phenomenon that we used is adding the blocking capacitor in parallel to the supply pin of each integrated circuit on the board. This capacitor provides charge to the component in the need. The second protection is the filter mentioned in Figure 4.15.

Finally, to lower the noise in our analog part, we separated the ground for the analog and digital parts. In PCB design are two separate polygons of poured copper are connected by one thin route. The analog ground is marked in Figure 4.15 by the GNDA symbol. It is worth mentioning that the analog multiplexers and shift registers are also powered from filtered voltage and connected to the analog ground. The control of the pipeline adds noise when measurement is being set; however, we measure voltage only when all transients are already subsided. By this approach, we eliminate noise created by switching electronics.

■ 4.2.4 Resistor Matrix and reading principles

When a multi-taxel sensor is designed, multiple resistors are needed to be read. In several works published, the resistor matrix occurs. With a growing number of resistors to be measured, having static electronics for every one of them leads to a very complex design. A slightly better design would be having one reading electronics and using analog switches to multiplex between resistors. However, this idea leads to a high number of driving signals and an unnecessary high number of analog switches. To reduce this number, a resistance matrix can be utilized. Figure 4.16 shows the matrix in 2 by 2 shape and the basic read of its matrix. The most simple and intuitive reading principle is based around selecting resistor

(a) Schematics of simple resistor matrix with two rows and two columns

(b) Basic reading schematics featuring column and row select multiplexers with one channel for each row and column of matrix.
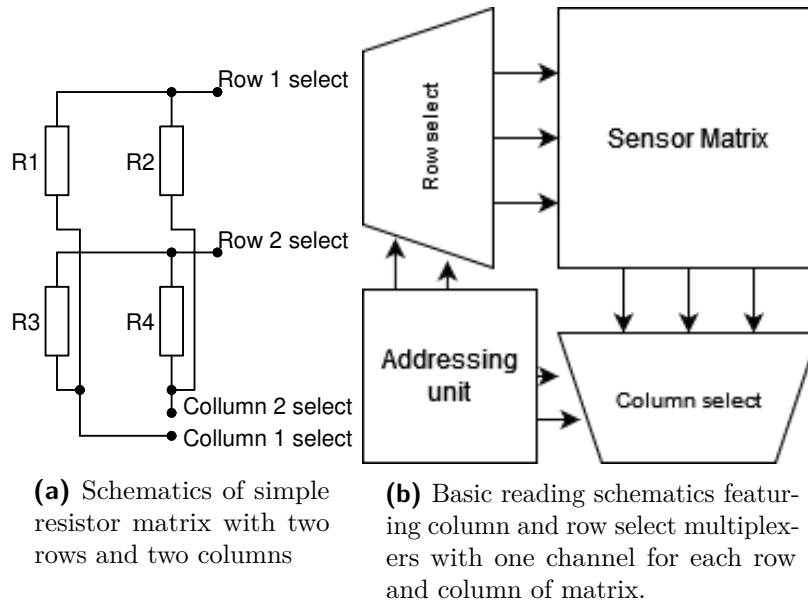
Figure 4.16: Resistive matrix principle

to be measured by switching signal paths using multiplexers. For example, if resistor R1 is

to be selected, measuring current is sent through Row 1 select node and is sunk out using Column 1 select node. Unfortunately, in this configuration, the measurement of current is not restricted to flow only through resistor R1. Current flows also through the resistors R2, R3, and R4 because nothing prevents it from doing so. This phenomenon is called cross-talk, and unwanted currents cross-talk currents. [30] This results in not reading the actual value of R1, but rather the serial-parallel combination of resistors given by formula

$$R_{read} = \frac{R1\,(R2 + R3 + R4)}{R1 + R2 + R3 + R4}. \tag{4.1}$$

There are numerous ways to work around this problem. The first possible solution to this problem is to adjust the reading circuitry to provide shielding and block cross-talk currents [30]. Instead of using multiplexers to select row and column, a series of switches is used instead. Switches as shown in Figure 4.17 connect a particular row select wire to a reference voltage potential or to the ground. Since negative feedback is utilized for each operational amplifier, all column select channels are forced to Vref voltage. If a row-select line is connected to ground potential, measurement current flows through a given resistor. Since the other row select lines are connected to reference voltage potential, there is no potential difference on non-selected resistors and, therefore, no cross-talk current flows. Measurement current is given as
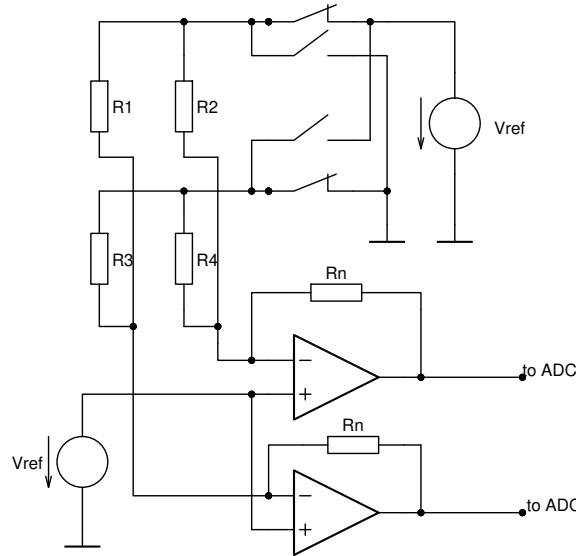
Figure 4.17: Cross-talk compensation using shielding

$$I_m = \frac{Vref}{Rx}, \tag{4.2}$$

where Rx is measured resistor. Outputting voltage of operational amplifiers is then given as

$$Vo = Vref\left(\frac{Rn}{Rx} + 1\right), \tag{4.3}$$

where Rn is known resistance and Rx the measured resistance [30].

The only sources of error for this reading principle are the imperfections of operational amplifiers such as input offset voltage [30]. Negative feedback forces the zero voltage difference between inputs of the operational amplifier; however, the component is not ideal, and a certain voltage difference between inputs persists. This voltage is called the input voltage offset. For a regular amplifier, such voltage is in units of mV, so if the reference voltage is set much higher, for example, 1.2V, the resulting voltage difference is negligible.

Unfortunately, this design would be challenging to use in our case. The main issue would be to measure the current. Since our sensors have low impedance, Equation 4.2 implies high measuring currents and potential destruction of operational amplifiers. The solution to this might be either adding bias resistors in series with each measured resistor or lowering the reference voltage. If a lower reference voltage was used, in units of mV, for example, the input offset of the amplifiers would cause a significant error. Adding bias resistor would lower the overall range of $\frac{\Delta R}{R_0}$ which is high for GA-based sensors. Furthermore, this solution does not compensate for the contact resistance of the connectors used in construction, which is crucial for our work due to the low impedance nature of our sensors.

F. Vidal-Verdú in [30] introduces more possible ways of canceling cross-talk currents. Some introduced methods turned direct resistor measurement into time measurement. A capacitor is charged through a measured resistor. The time constant of the formed RC circuit is then proportional to the resistance, since capacitance is, unless we ignore capacitor drifts, static. The cross-talk currents are also blocked by applying voltage to the rest of the circuit, similarly to Figure 4.17. Still, none of these methods is useful in our case, as none compensates parasitic resistances.

The next solution we found to this problem is to use a convolutional neural network to estimate the real distribution of resistance in the matrix [27]. The input for the neural network is resistances computed by Ohm's law, while cross-talk currents are still present. The neural network was trained on a synthetic dataset. As stated in [27], it is possible to evaluate the model in $2.2ms$ for 16×16 taxels on Intel i7 processor. We would rather find solution on low level or even in hardware, instead of compensating during run-time using such computation heavy software.

Since our work mainly focused on designing functional sensors, we had not much more time to design a system suitable for matrix composed of GA sensors. Next, the construction of a resistor matrix is an optional task in the specification of this thesis, so we decided to focus on mandatory parts in the remaining time. The technological issues stated above brought too many complications to our design that we could not use them. We plan to investigate this topic in future work. Instead, we used the principle for basic matrix reading shown in Figure 4.16 for now.

To eliminate the influence of contact resistance described in Figure 4.11b of connectors, the 4-wire method was used. In Figure 4.18 is shown basic schematics of the measurement. Measuring current is passed through node A, through one of current channel switches (I row 1 or I row 2), through selected resistor (if we ignore cross-talks for now), through current channel switches (I col. 1 or I col. 2) and finally through node C out. The voltage created by the measurement of current is then sensed between nodes B and D using an instrumental
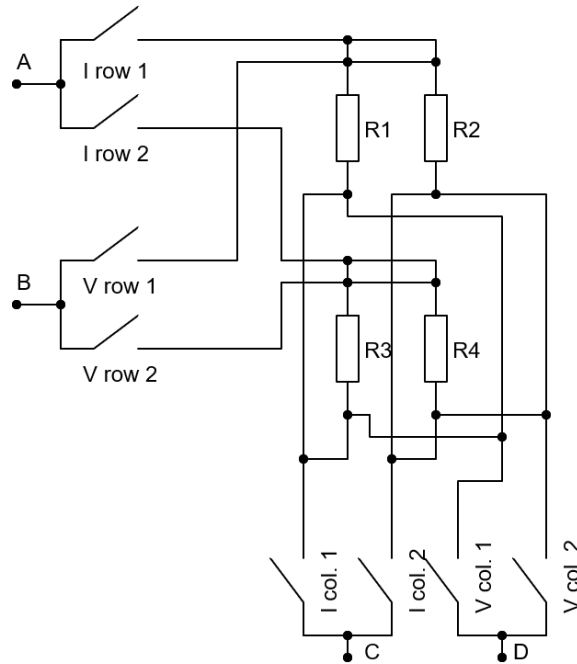
Figure 4.18: Schematics of 4-wire connection using multiplexers for matrix 2 by 2. Parasitic resistances are for sake of simplicity of schematics left out.

amplifier. Since the voltage track is connected to the resistor as close as possible and since no current flows through nodes B and D, none of the parasitic resistances is included in the measurement [26]. This design mitigates not only the contact and wire resistance, but also the on-resistance of the used analog switches. For an integrated circuit CD4052 used by Texas Instruments, the resistance can be around $470\,\Omega$ when supplied from 5V [31]. This resistance is much higher than the resistance of taxels, meaning that it cannot be ignored.

To avoid cross-talk currents in our current work, we used just a single row (or column) of sensors. In this configuration, the other current paths are opened and no current flows.

As a current source we used circuit LM334 as shown in Figure 4.19. When choosing two resistors, the measuring current was set at approximately 0.5 mA. Circuit LM334 can be alternatively used as a thermometer and for our cause it's temperature dependency must be compensated. By adding a silicone diode to the schematics, thermal feedback is established [32]. Data sheet provided by manufacturer [32] introduces a formula

$$I \approx \frac{0.134}{R1}, \frac{R2}{R1} = 10. \tag{4.4}$$

Thermal stabilization performs at the best performance when the diode is placed as close as possible to the body of the current source [32].

▪ 4.2.5 Adjustable gain

In our research we decided to design a sensor with multiple taxels. Unfortunately, our taxel manufacturing procedure is not perfect, and the resulting sensors usually do not
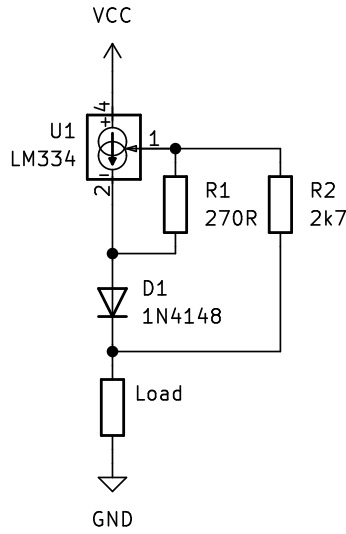
Figure 4.19: Schematics of current source with LM334. Load resistance is in our case resistor matrix.

always have the same base resistance R_0. If static gain would have been used in the reading pipeline, the resulting measurement would have had different resolutions for each sensor. For example, assume two taxels "A" and "B". Taxel "A" has base resistance $R_{A0} = 10\,\Omega$ and taxel "B" $R_{B0} = 5\,\Omega$. If we set reading pipeline such as R_{A0} to result in maximum output voltage at input of an analog-to-digital converter, with the same setting, R_{B0} would result in half the voltage. This would lead to sensor "B" having half the resolution in contrast to sensor "A".

To overcome this problem, we could use programmable amplifiers. This component behaves similarly as regular amplifier, but it's gain is set over a digital interface such as SPI. Unfortunately, these amplifiers usually only have a small number of settings. For example, the MCP6S91 amplifier offers eight gain selections, which is not enough for our case [33].

We decided to design amplifier with more selections. The basic idea is shown in Figure 4.20. The circuit uses the principle of the R2R resistor network. When connecting resistors to ground potential using electronic switches S0 - S3, the feedback is adjusted and the gain is set as shown in Table 4.2.

S3	0	1	0	1	0	1	0	1	0	1	0	1	0	1	0	1
S2	0	0	1	1	0	0	1	1	0	0	1	1	0	0	1	1
S1	0	0	0	0	1	1	1	1	0	0	0	0	1	1	1	1
S0	0	0	0	0	0	0	0	0	1	1	1	1	1	1	1	1
G	1	2	2.5	4	3	5	5.25	8	3.5	6	6.5	10	6.5	10.5	10.625	16

Table 4.2: Truth table of adjustable amplifier gain using R2R network (1 – switch closed, 0 – switch open). As closing the switch changes serial-parallel combination of resistors, in one case we obtain same feedback for two different settings.

This solution is yet still not sufficient for our cause as it provides only 15 different gain

35
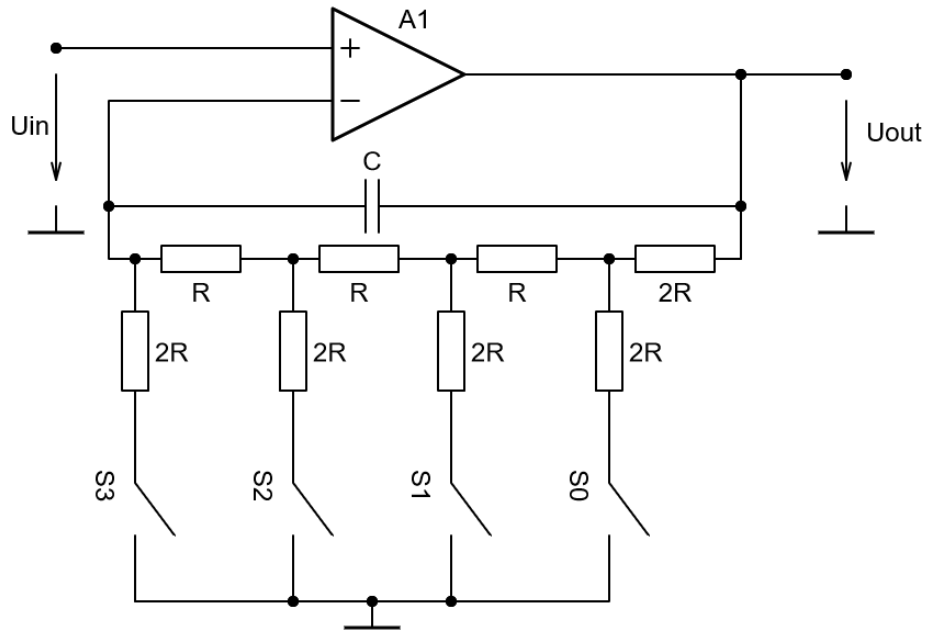
Figure 4.20: Adjustable gain using R2R network

settings. We improved the circuit as shown in Figure 4.21. Thanks to the second operational
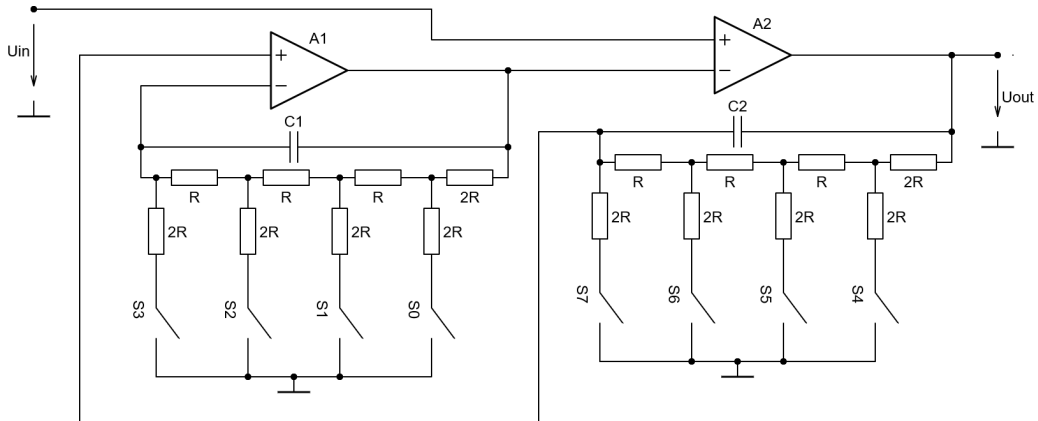
Figure 4.21: Dual adjustable gain using R2R network.

amplifier in the feedback of the first one, it is possible to set gain as a rational number composed from gain values shown in Table 4.2. Electronic switches S4 – S7 are set to set the gain nominator, and S0 – S3 to set the denominator. The number of possible unique gain selections is given as

$$N = 15P2 + 1 = 211, \tag{4.5}$$

where $15P2$ is permutation of 2 samples from set of 15 different settings (as gain of 6.5 occurs twice in the Table 4.2). Since unit gain is possible to set only by selecting one gain twice, we have to add one to result of permutation.

The source of error in this case is mostly the precision of resistors in the R2R network.

We used regular 1% resistors, which means that each resistor value is in the range of 1% from the advertised value. The next possible source of wrong gain would be resistance of an analog switch in the on state. Since only one direction of current is needed, we can simply use transistors. In real implementation of the circuit, using eight pins of driving processor to set gain would be unpractical. Instead, to connect resistors of the network to ground, we used the shift register with open-drain output TPIC6C595. This integrated circuit features in one package eight transistors to drive the gain and shift register which is perfect for this application.

The capacitors C1 and C2 in Figure 4.21 are used to stabilize the circuit. Without them, the circuit oscillates. We assume that the source of this behavior is parasitic capacitors formed between the legs of integrated circuits and the dynamics of the amplifiers themselves. Capacitors C1 and C2 help mitigate the influence of these effects. Using an experimental approach, we set the capacitors C1 and C2 to 330 pF.

When designing a measurement chain, the band width of such a device is an important parameter. While using operational amplifiers, the cutoff frequency of the amplifier could usually be estimated by formula

$$F_c = \frac{f_t}{G}, \tag{4.6}$$

where f_t is so called transient frequency of operational amplifier [34]. It is the frequency at which the gain of the inner amplifier of the operational amplifier reaches 0 dB. The variable G is the gain of the amplifier with feedback. This means that the higher the gain, the lower the bandwidth of the resulting amplifier.

In our case, due to the attached capacitance in the feedback, we cannot rely on a simple formula like Equation 4.6. To estimate the usable bandwidth of our designed amplifier, we decided to measure the frequency response characteristics for a number of selected gains. For this measurement, we used the computer oscilloscope PicoScope 2004A with integrated function generator. We measured up to 100 kHz, which was the maximum frequency of the signal generator used. In our implementation we used operational amplifiers MCP6002 with $F_t = 1\,\text{MHz}$. If we apply formula 4.6 to $G = 16$, we would obtain an estimated frequency range of 62.5 kHz. In Figure 4.22 we can see that the resulting cutoff frequencies are lower than formula 4.6 would result in. However, we expect signals with much lower frequencies, up to units of kHz, so these frequency responses are more than sufficient. We can also notice, due to imperfection of the components used, that the frequency responses of $G = \frac{1}{1}$ are not the same as $G = \frac{16}{16}$. However, any significant difference is present in the high frequency range, out of the range of our interest.

We also measured a phase spectrum of the amplifier. With respect to the magnitude spectrum, we would expect the phase spectrum to look like this. Our main aim for this examination was to ensure that there is no hidden problem in this part of the frequency response. For example, sudden change of phase.

The amplifier was powered by a 5 V supply voltage. The operational amplifier MCP6002 can be safely used with a supply voltage of 3.3 V. Since MCP6002 is a rail-to-rail amplifier, the maximum output voltage is almost the supply voltage. The 3.3 V supply would then
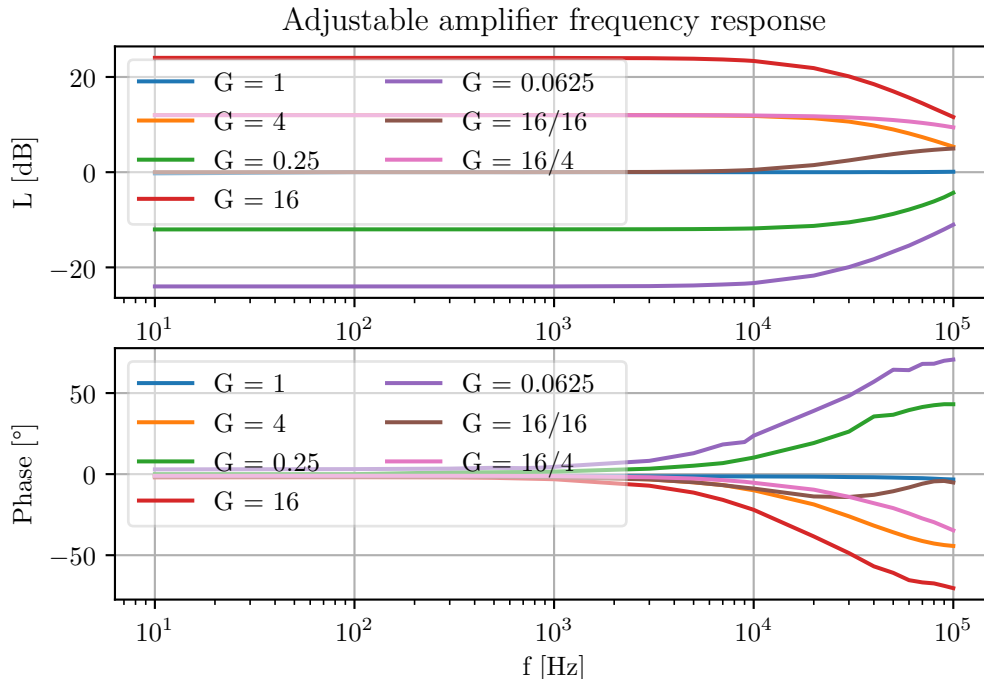
Figure 4.22: Frequency responses of amplifier for given gain set. The first plot shows the magnitude characteristics in dB. The cutoff frequency is defined as a decrease of 3dB from the middle of the band. Second plot shows phase shift between input and output signal.

be easier to use with an analog-to-digital converter powered also from $3.3\,\text{V}$. However, the input common mode range for this amplifier would not allow swinging in full range of $[0\,\text{V}., 3.3\,\text{V}.]$. Input voltage swing is given with respect to supply voltage, meaning the wider the input voltage range can be obtained by increasing the supply voltage.

On the other hand, we need to pay attention to an unwanted states of the amplifier. We cannot forget that the Teensy 4.1 board is connected to the output of the amplifier. To prevent the Teensy board pin from burning when saturation occurs, a protection resistor $470\,\Omega$ is added in series to the signal path that limits current through the substrate diode. Worst case scenario current is given as

$$I = \frac{Vcc - Vcc_{Teensy}}{R} = \frac{5 - 3.3}{470} \approx 3.62\,\text{mA}. \tag{4.7}$$

▪ 4.2.6 High pass filter

A good feature of the tactile sensor is also the ability to detect alternating signals. An example of such signals might be vibrations. When the tactile sensor slides onto the surface of the material, the generated AC signal can be used to classify the texture. For lack of time, we did not conducted any texture recognition experiments, but we wanted to observe sensors reaction to vibrations.

When our tactile sensor is excited with vibrations generated by speaker or vibration

motor, the outgoing signal oscillates with a rather small amplitude with quite high DC offset. In our case we observed, for example, oscillations with amplitude 20 mV around the 3 V DC value. Collecting such small oscillations with an analog-to-digital converter with fixed reference voltage is rather challenging. We decided to workaround this issue using a second-order active high pass Sallen-and-key filter with cutoff frequency $f_c \approx 1$ Hz followed by a static gain amplifier. The schematics of our design are shown in Figure 4.23. Using this circuit, we separate the DC part from the signal and amplify only the AC signal [34]. By setting the resistors R3 and R4 we adjust the damping of the resonance circuit. We
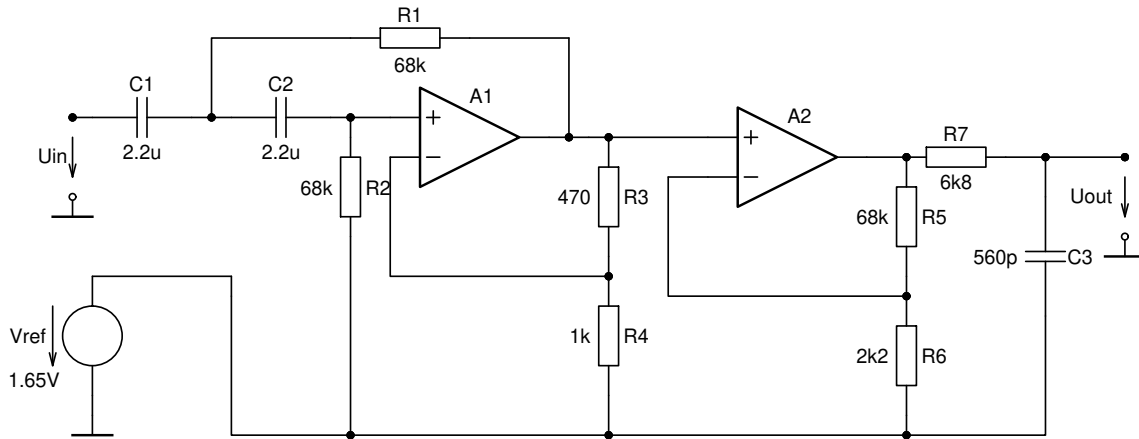
Figure 4.23: High pass filter schematics. Operational amplifier A1 operates as a high-pass filter and A2 as a static gain amplifier. Outputting signal is oscillating around voltage 1.65V, representing the middle of the ADC range.

were choosing between two settings, Chebyshev's and Butterworh's approximation, and compared their step response time series shown in Figure 4.24. The cutoff frequency is set

Figure 4.24: Comparison of step responses of high pass filters for given damping. Chebyshev's approximation filter shows rather long time to stabilize, in contrast to Butterworth's

by capacitors C1, C2, and resistors R1 and R2. The resonance of the filter for Butterworth's

approximation is given as

$$f_0 = \frac{1}{2\pi CR} = 1.064 Hz \tag{4.8}$$

and for Chebyshev's approximation as

$$f_0 = \frac{1}{0.907 \cdot 2\pi CR} = 1.173 Hz, \tag{4.9}$$

under condition R = R1 = R2, C = C1 = C2 [34].

Chebyshev's approximation provides a steep frequency characteristic, however, in the time domain it takes a long time to stabilize. On the other hand, Butterworth's is moderate in both cases. In this case, we are most interested in separating the DC value, the frequency response steepness is not the most important feature we are looking for. We decided to use Butterworth's approximation, since it stabilizes faster than Chebysev's. Moreover, since the amplifier is supplied from 5 V the saturation is in a higher range than is used for the analog-to-digital converter. In our design we use protective resistor, so when higher voltage is present on input of AD-converter, nothing is damaging, however, it is better to stay as much as possible in voltage ranges for which ADC was designed for. For this reason, we chose the Butterworth approximation.

Resistor R7 not only protects the input of Teensy board, it also in combination with capacitor C3 forms a low-pass filter tuned to approximately 40 kHz. The high-pass filter amplifies a lot of high frequency noise which is reduced by this low pass.

The disadvantage of using high-pass filter lies in the duration of transient response which limits switching rate between sensors. So far we used this part of the circuit only when only one taxel was measured. In case of some practical application, in which the task to measure vibrations is concerned, a low switching rate between taxels would be needed, for example a rate of $0.5Hz$.

◼ 4.2.7 Low level software

As mentioned above, the reading pipeline is controlled by the Teensy 4.1 development board. For the proper function of the device, software is needed. To program the Teensy board, Arduino IDE was used. This platform is not optimal and controversial; however, Teensy 4.1 has very sophisticated support for Arduino.

Moreover, for Arduino projects is already available ROS serial library. This library utilizes connection between low-level software and ROS running on master device featuring message publication, time synchronization, and topic subscription. The low-level device can simply work as a regular ROS node. We use this interface to propagate measured data into the system and synchronize our data using ROS time. Next, it is possible to command the ROS device to reset the values R_0 and select the best gain for each taxel.

One sensor data message contains information about one tactile matrix, such as the name of the sensor text, the dimensions of the sensor, and the timestamp of the message. Regarding data, the device sends pre-processed data for each taxel, raw data from an

analog-to-digital converter, and first-order differentiation of pre-processed data. Finally statistics such as mean over taxels, minimum and maximum for both pre-processed and differentiated data are sent.

The application executes a very simple algorithm. First, ROS serial communication, subscribers, and publishers are initialized. Next, all taxels are measured with unity gain. This value is used to compute optimal gain such that

$$G^* = \frac{V_{des}}{V_{G=1}} = \frac{3}{V_{G=1}}, \tag{4.10}$$

where V_{des} is voltage desire for resistance R_0 to result in, in our case $3\,\mathrm{V}$. Voltage $V_{G=1}$ is the voltage measured for the unity gain set. Based on G^* we choose from a bank of possible gains (denoted as B) the one for which holds

$$\hat{G} = \operatorname*{argmin}_{G \in B} |G^* - G|\,, GV_{G=1} < 3.2. \tag{4.11}$$

The condition for $GV_{G=1}$ is used to limit the maximal voltage output of the pipeline. This maximal voltage was selected so that the residual voltage range would form a reserve in the output voltage range of the amplifiers in the event of an increase R_0. The value $\hat{G}$ was selected simply using a brute-force algorithm that iterates over all possible gains in B. This algorithm is very inefficient with respect to time complexity; however, this selection is meant to run only occasionally. For a small number of sensors, this operation does not slow down the process.

When the best possible gain value for each sensor is obtained, the device starts to measure periodically. For each measured taxel, moving average is computed in order to lower noise in data. We utilize a circular data buffer over which the mean value is computed. The buffer has capacity for 10 measurements. Next, comes the data pre-process. This operation will be discussed in more detail in Section 6.2. After this we compute sensor statistics such as average over taxels of given sensor, maximum, and minimum. Finally, first-order differentiation is computed for all calibrated data; the same statistics are computed for differentiated data. These statistics are used for the control application in Chapter 6.

When data is obtained, a message containing new payload is created and published in a given topic over Ethernet interface. The pipeline then waits for a given period of time, in our case $10\,\mathrm{ms}$. The resulting data rate is $100\,\mathrm{Hz}$.

■ 4.2.8 Physical implementation

The measurement chain is designed as a multi-board system. Such an approach enables easier prototyping as each part can be tested and redesigned individually. The main board contains connectors for Teensy 4.1 as well as supply voltage management such as step-down, supply voltage filter, and reference voltage source for high-pass filter. The analog circuitry is divided into two boards. The upper containing taxel select, current source, and differential amplifier, the second the adjustable gain, and high pass filter. All boards are connected using pin header connectors.

To enhance mechanical integrity, boards are screwed to 3D printed plate and columns. The plate keeps all modules in place and securely connected, as well as prevents mechanical damage from bending the connectors.

The tactile matrix is connected using two pairs of eight wire-shielded cables. Cables are held in place using a 3D printed attachment. The holder keeps the sensor connected and prevents damage to the connectors. During experiments such attachment prevented any structural damage when robot executed unexpected trajectory and whole board was lifted off the table, where previously lied. Not only did no connector be disconnected, all boards stayed unharmed.

(a) Full view of the system without Ethernet socket connected.
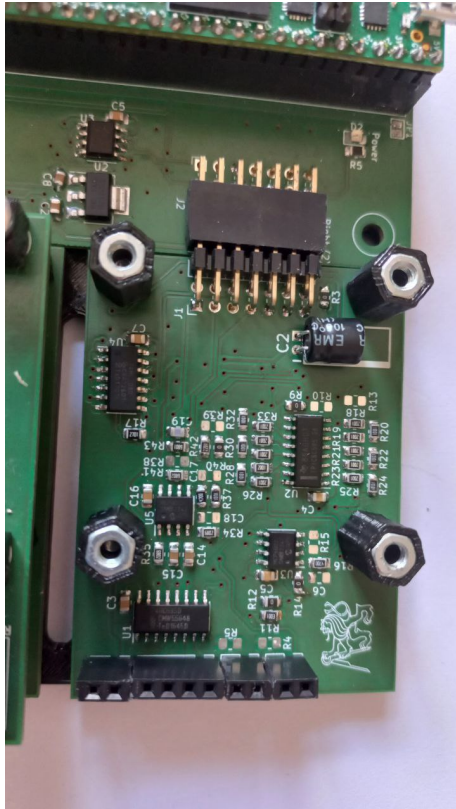
(b) Lower analog board featuring adjustable gain. The Board is connected to the main board using a double line pin header connector

(c) Upper analog board featuring taxel addressing. The cables are held in place using plastic 3D printed holders.

Figure 4.25: Physical implementation of reading electronics

Chapter 5

GA sensor testing and performance evaluation

In this chapter we would like to show the performance of our sensor. We tested the sensitivity, frequency range, temperature dependence, and durability. Most of the experiments were conducted on two particular sensors labeled "20R" and "5R". This label corresponds to the val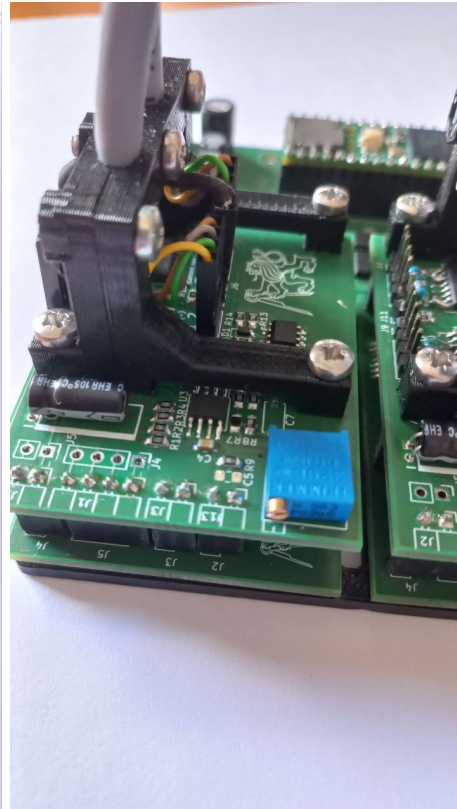ue sensors shown R_0 after manufacturing, although this value over a horizon of days of their lifetime drifted to the different value. Most of these experiments were performed prior to the design of the tactile matrix (line) sensor.

Figure 5.1: Sensors 20R and 5R. The sensors are labeled accordingly. White rectangles show sensor position.

5.1 Sensitivity and force matching

The aim of this experiment was to estimate the non-linear function which could used to describe the force-to-resistance dependency. Unfortunately, our laboratory was not equipped with such a device, which would apply a given force to the sensor. We decided to build our own press.

5.1.1 Press building

The main part of the press is a linear shift transmission. The device is actuated by a stepper motor that turns a bolt. The motor was operated with $\frac{1}{16}$ steps to enhance the smoothness of the movement. The resolution of the theoretical position has been estimated

to $2.5\mu m$, however we cannot ignore the elasticity of the material, and such precision cannot be ensured. For this reason, we cannot examine sensors sensitivity with respect to the strain of the GA sensor. Instead, we provide force measurement. The press was usable only to generate forces up to 15 N, since the mostly plastic construction started to bend significantly and the danger of destruction occurred.

On the top of the moving platform is a strain gauge. The strain gauge is read by the HX-711 analog to digital converter. On the opposite side of strain gauge is a mount to hold the experiment subject in place. The mount allows subject positioning to press on certain parts of the subject.

The heart of the device is a Raspberry Pi Pico development board, which controls the stepper motor driver and reads the values from HX-711. The device is furthermore connected to ROS using an interface based on the ROS serial library. Data are published on given ROS topic with timestamp for synchronization. To control the motion of the press, the number of steps is sent in the form of a message to the device from ROS. In case of wrong command or other error, Raspberry Pi Pico can be set into reset state using latching switch pulling the 'RUN' pin of the processor to the ground, effectively stopping all motion. In reset state, no new commands can be sent to the device.
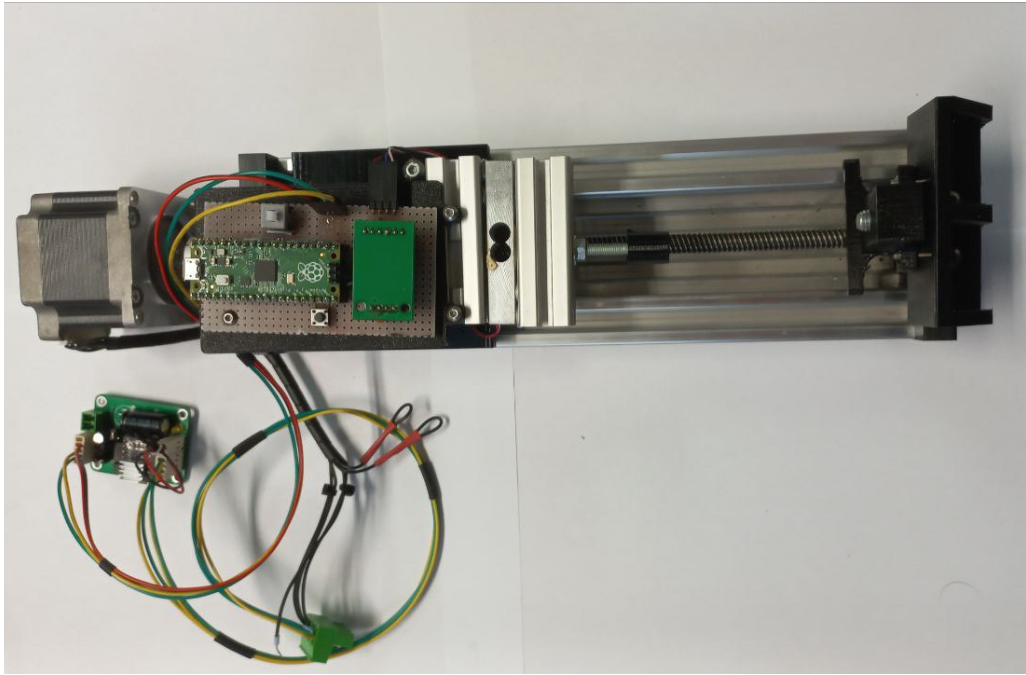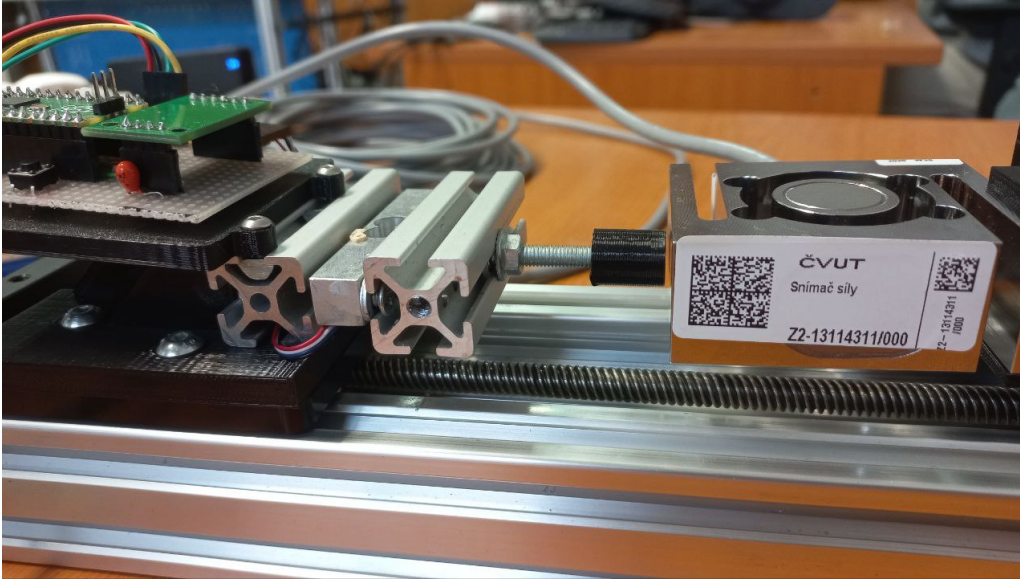

Figure 5.2: Press construction

Next, we needed to calibrate our press device. For the reference measurement device we took an HBM S9M strain gauge and a ClipX BM40 industrial amplifier. The sensor S9M is factory calibrated for a range of up to $500N$ in accuracy class 0.02%.

We assumed for calibration this model

$$F + b_{ref} = k(x + b_{press}), \tag{5.1}$$

Figure 5.3: Calibration procedure of the press using reference strain-gauge S9M.

where x represents numeric value obtained from sensor, b_{press} represents offset of press strain-gauge and b_{ref} is offset of reference sensor S9M. The parameter k is the sensitivity constant of our sensor. First, we calibrate the offset b_{press} and b_{ref} by measuring the output when no force was applied (the sensors did not touch at all). After subtracting offsets from output signals, we get the model

$$F = kx, \tag{5.2}$$

which allows us to obtain sensitivity k by dividing

$$k = \frac{F}{x}. \tag{5.3}$$

Theoretically, only one measurement is enough to obtain k precisely. However, our measurement also contains noise. For a more robust estimation of the sensitivity, we applied forces in the range $[0.5, 10]\,N$. Using equation 5.3 we estimated k for each data point in measured series. The final k was obtained by computing the mean value on all the values computed k. Result of our calibration of presses strain gauge is shown in following Table 5.1

b_{ref} [N]	b_{sen} [-]	k [N]
-1.421	$-2.986 \cdot 10^2$	$2.475 \cdot 10^{-5}$

Table 5.1: Press calibration result

Unfortunately, initially both strain gauges were not synchronized and with different sampling frequencies. To synchronize the the measurements in time, we have created a simple ROS interface for the ClipX amplifier. This amplifier is equipped with several industrial buses, such as Profinet or EtherCat. However, our laboratory does not have any device capable of communicating over these interfaces. However, the amplifier also provides an HTTP server for maintenance purposes. Our interface employs net-scrapping method to
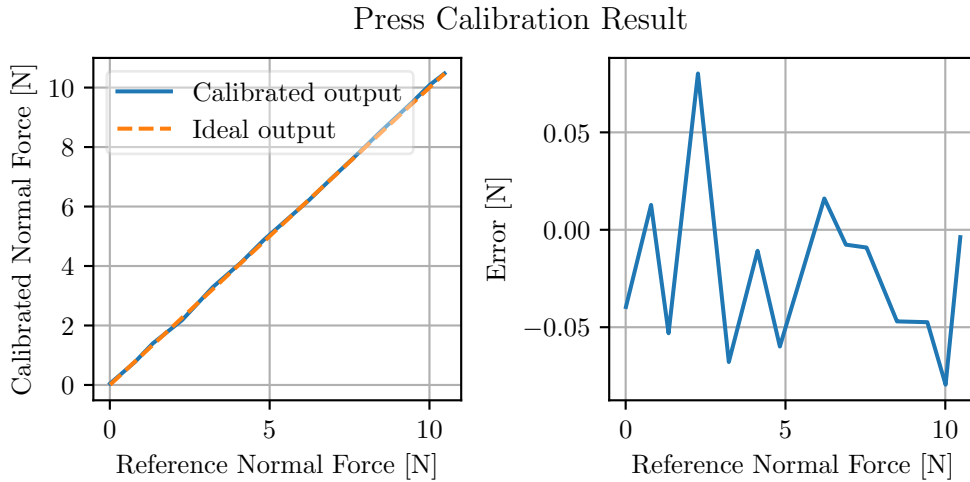
Figure 5.4: Press calibration result. To validate our calibration, several forces were set, and measured output was stored. The resulting error is shown to be very low.

obtain measured data using Python script. The data are then published in a given topic with ROS timestamps to synchronize with the sensory data from the press. While both devices had different sample rates, we decided to down-sample output signal of the press. We went through reference data time series and for each data-point we found two closest time-stamps in press strain gauge data points and linearly interpolated between these data points.

5.1.2 GA sensor calibration and sensitivity estimation

With our press prepared, the calibration of the GA sensor could begin. The aim was to find parameters for non-linear function by which we approximate sensor's force dependency. The calibration procedure was similar to the press calibration. We attach the graphene sensor to a device and apply force in rage $[0, 10]\,N$. Both signals were synchronized using ROS time and re-sampled using the same procedure as in the press calibration procedure.
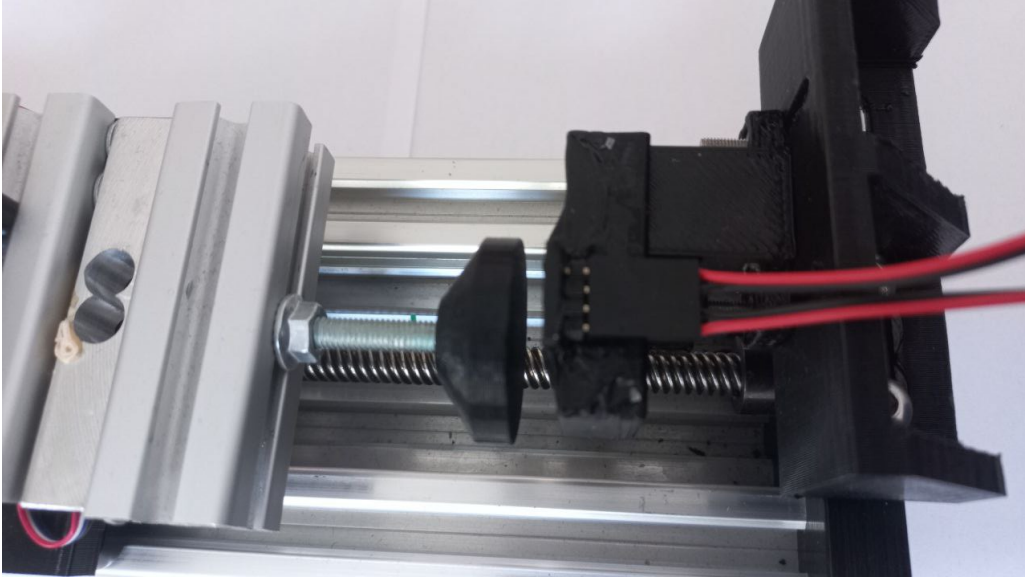
Figure 5.5: GA sensor calibration procedure

From [12] we know, the GA based sensor shows rather complex nonlinear function. On log-log scale, this function is linear for low forces and logarithmic for higher. Unfortunately, it would be hard to automatically calibrate this kind of model, without prior knowledge, where is the breaking point, where linear function terminates and exponential takes place. After few iterations of experimenting we fitted data with curve

$$F(x) = Ae^{-Bx} + C + Dx^3 + Ex^2 + Fx, \qquad (5.4)$$

where $x = \frac{\Delta R}{R_0} + 1 = \frac{R_0 + \Delta R}{R_0}$. To do so, we used the non-linear least squares method using the Python Scipy library. As a result, we obtained the parameters shown in Table 5.1. The curve fitting can be seen in Figure 5.6.

	A	B	C	D	E	F
20R	2110.8583	19.1635	11.7390	-13.5490	34.5664	-32.6890
5R	9279.7167	16.9108	51.2305	-91.2248	218.1547	-178.0039

Table 5.2: Sensors calibration constants

49
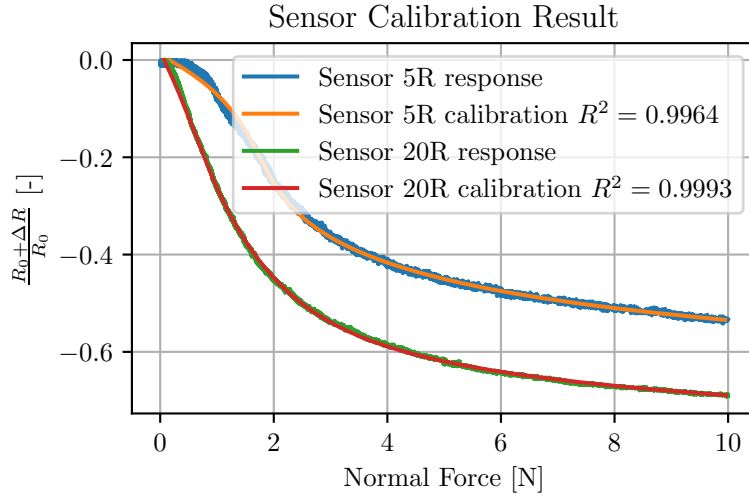
Figure 5.6: GA-based sensors response fitting results.

Sensitivity is defined as

$$S = \frac{dX_s}{dX_m} \approx \frac{\Delta X_s}{\Delta X_m}, \tag{5.5}$$

where X_s represents sensors output signal and X_m is measured value. [26] To estimate sensitivity we used force response approximation. Sensitivity is then given as

$$S = \frac{dF^{-1}(F_n)}{dF_n}, \tag{5.6}$$

where $F(x)$ is function 5.4 and F_n is applied normal force. The derivation was obtained numerically by first-order differentiation with a maximum step of $0.87\,\text{mN}$. Other sensors
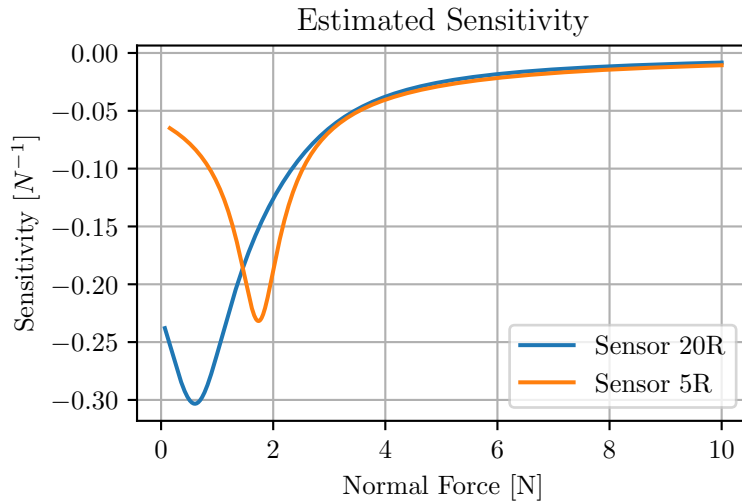
Figure 5.7: GA sensors estimated sensitivity as a function of applied normal force.

researchers tend to show sensitivity with respect to units of pressure, such as kPa^{-1}. In our

case, we cannot measure the sensor area accurately enough. Graphene samples were made as approximately $4 \times 4 \times 2mm$ blocks. The maximum sensitivity would be then given as

$$\hat{S} = S \cdot A,$$
$$\hat{S}_{20R} \approx -0.3033 \cdot 4^2 = -4.85 \, \mathrm{MPa}^{-1},$$
$$\hat{S}_{5R} \approx -0.2318 \cdot 4^2 = -3.7088 \, \mathrm{MPa}^{-1},$$

where $\hat{S}$ is sensitivity in units of pressure, S is sensitivity in units of force and A is area of sensor. These sensitivity values are compared to the sensors [3, 4] approximately $1000\times$ lower. On the other hand, these sensors were examined in a range of tens of kPa, whereas our sensor was exposed to pressure up to $625 \, \mathrm{kPa}$. Furthermore, in the following text, we discuss the performance of a GA-based sensor capable of measuring pressures in units of MPa.

Next, we examined how stable in time the calibration will be. We observed that features of graphene aerogel-based sensors drift over time. The experiment was repeated after portions of time.

(a) Verification immediately after calibration

(b) Verification after 12 hours

(c) Verification after 16 hours

(d) Verification after 17 hours
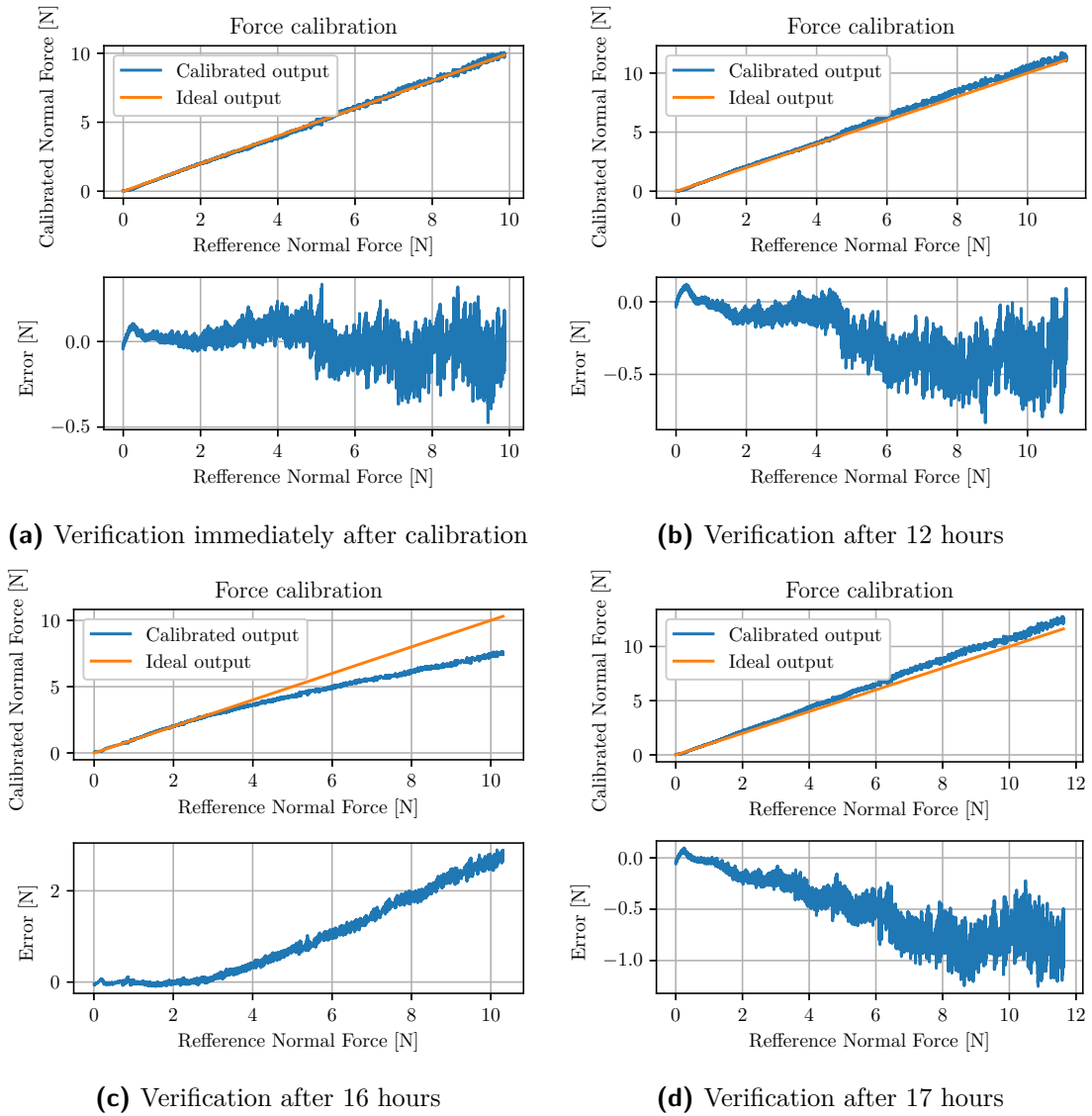
Figure 5.8: Calibration verification over time for sensor "20R"

We can see, that GA sensor long term instability is showing in calibration results as well. Also, something happened after sixteen hours as the sensor deviated from the expected function. However, this behavior vanished in the next hour. We conducted one more experiment right after calibration.

To validate our calibration data without contraption we built we tried to weight the M20 nut using the sensor "20R". Its mass was obtained using scales of 52 g. We used 3D printed plastic board (approximately 9 g in mass) to help balance the sensor nut. Total applied weight of 61 g would generate force

$$F = mg = 0.061 \cdot 9.81373 = 0.5986N, \tag{5.7}$$

where m is mass in kg, g is gravitation acceleration in ms^{-2}. The time series of the experiment is shown in 5.9. The highest deviation from expected output force give by
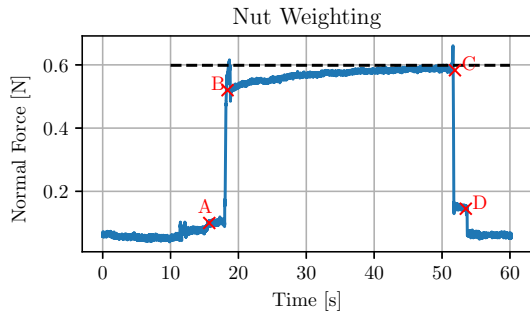
(a) Time series of experiment. At point A, a plastic plate was placed on top of the sensor, at point B the nut was placed. At point C nut was removed and at point D plastic plate.
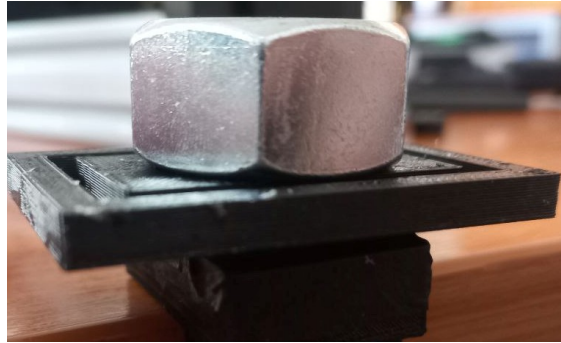
(b) Experiment procedure, sensor with plastic plate and M20 nut on top.

Figure 5.9: Nut weighting test using sensor "20R"

equation 5.7 is $0.0786N$ which by same equation corresponds to $8g$, which is ~13% of expected value. Even though an error like this is rather large with respect to the total dynamic range of the sensor, we find this result to be precise enough.

■ 5.1.3 Large force measurement

The aim of these experiments is to show that a GA-based sensor is capable of measuring normal forces in a wide range. For this experiment, we replaced the plastic parts from the press described in Section 5.1.1 with aluminum profiles. Since the strain gauge used in 5.1.1 would not withstand such high forces, we equipped the press with a strain gauge HBM S9M. This experiment was not carried out on sensors "20R" or "5R". These are mounted on a plastic gripper attachment. The attachment is mostly hollow to house the gripper finger and could not withstand such high forces. Instead we used sensors constructed only from PCB, primary and secondary covers.
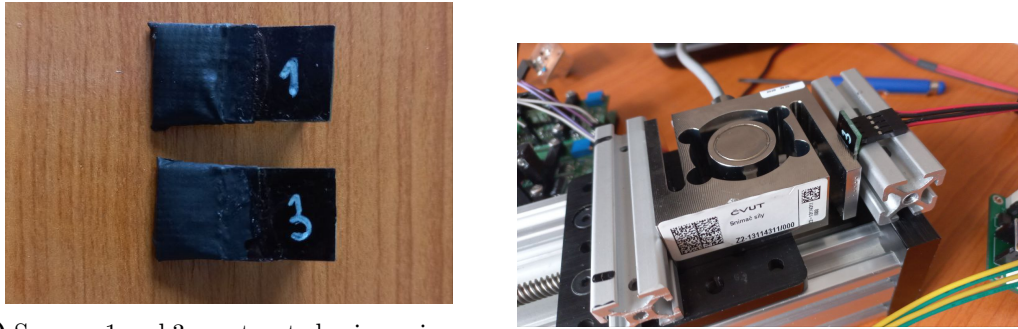
(a) Sensors 1 and 3 constructed using primary cover from cleared medical tape an nitrile secondary cover on top. Due to the air pressure issues discussed in 4.1.2 shows relatively small hysteresis.

(b) Sensor 3 being pressed during experiment. To prevent it from movement before being pressed double sided tape was used.

Figure 5.10: High force response measurement.

Measurement procedure stayed unchanged and response of sensor is shown in Figure 5.11. From Figure 5.11 we can see GA based sensors are capable of measuring forces up to 250N.
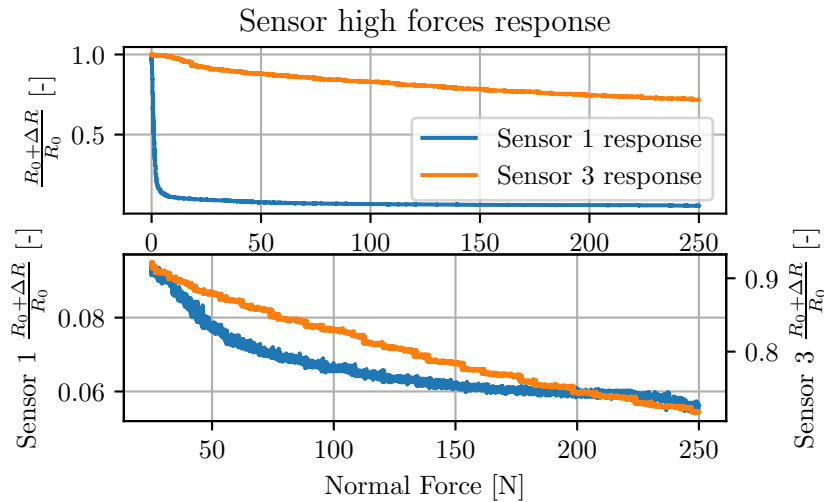
Figure 5.11: Response of sensors 1 and 3 to high normal forces. The second graph shows the zoom into the range of normal forces [25 N,250 N]. Sensor 3 has a significantly lower sensitivity for low forces compared to sensor 1. After reaching force of ~50 N, sensitivity is significantly decreased.

After these experiments, we did not observe any resemblance of breakage. Our sensors were made in approximately $4 \times 4 \times 2$mm. If we assumed the active area of the sensor ~16 mm^2, the maximum applied pressure would be ~15.625 MPa. This value is not the result of exact measurement and should not be taken as a fact. It only gives us the idea that we measured the values of a certain pressure of MPa, which is a much higher pressure than that found among other published sensors [3, 8, 9]. According to the manual [4] artificial finger BioTac is capable of measuring up to pressure of 100 kPa. The sensor capable of a similar maximal range would be the one published in [15]. Furthermore, with respect to Figure 3.1 shoving GA to sustain pressures in GPa, we can assume that it might be able to measure much

higher pressures. We assume that in this range the sensitivity would be very low, and the rest of the sensor must also be designed to withstand such high stress.

■ 5.2 Minimal distinguishable force of GA based sensor

Prototype of sensor shown in [12] shows a minimal measured force $326\,\mu N$. Such a resolution is truly remarkable, but the experiment was set to suit low-force measurement. We decided to find the minimum distinguishable force that we can detect while using our electronic devices. The resolution is fixed for full-scale measurement; the same setting is capable of measurement forces up to 250N.

In this measurement, we find significant noise in our signal. We are interested in a normal force, where the mean value of the noisy signal definitively leaves the noise range for no force applied. This restriction might be too timid and pessimistic, but in this case we are interested in a minimal force that we can confidently measure.
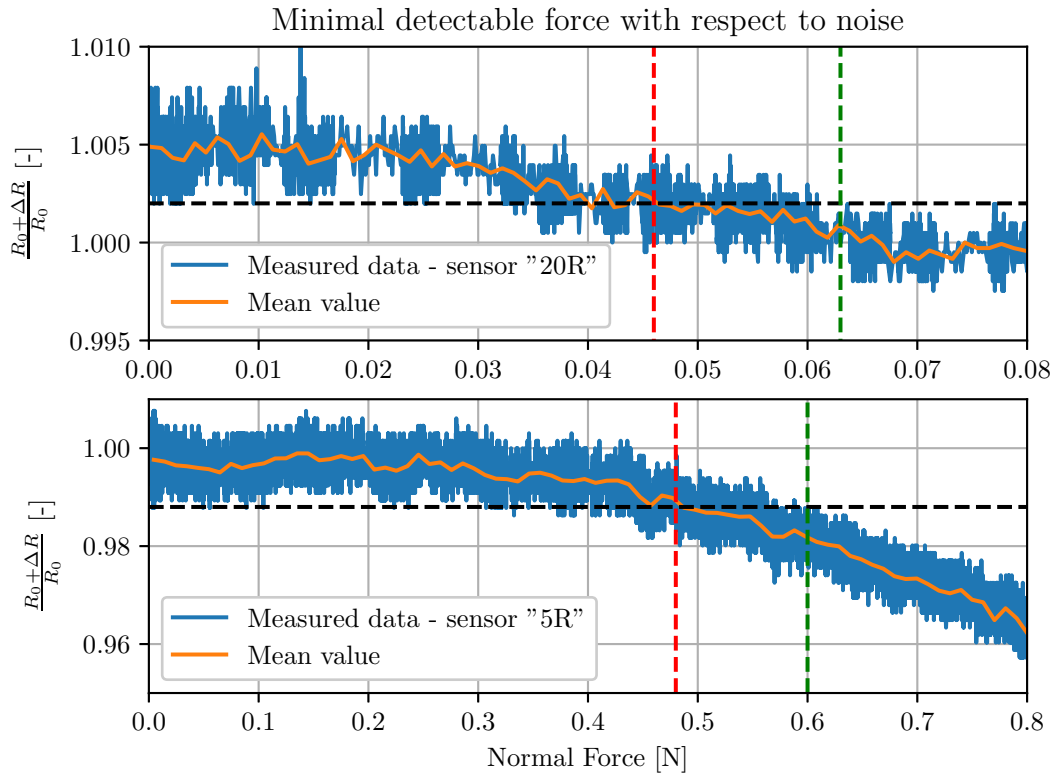
Figure 5.12: Upper plot shows minimal confidently detectable force (red line) where mean value leaves noise band for no force applied for sensor labeled as "20R". The green line marks the point where the noisy signal completely leaves this band. The same is marked in the lower plot for sensor "5R", however, for this sensor are such forces ~10× larger

As can be seen in Figure 5.12, for sensor "20R" is the minimal confidently detectable force

46 mN and for the other sensor 0.48 N. In comparison, our results are significantly worse than those presented in [12]. It is true that this measurement tests more the reading electronics than the actual sensor, but in a real-life application, these parts of the measurement chain are equally important. Moreover, with respect to the full range of measurement, we find this sensitivity to be quite fine.

5.3 Frequency range

The aim of this experiment was to acquire some guess of what the frequency response of the GA-based sensor would look like. We state that it is just a guess as our testing device is neither certified nor calibrated by any certified tool. To estimate the frequency range of our sensor, we needed a device capable of providing vibrations with frequencies up to units of kilohertz. Since we could not find such a commercially available device, we built our own. This device cannot provide any guarantees in the sense of some fixed reference. Moreover, our designed device does not allow us to set the exact amplitude of vibrations in units of length, which is a problem, as the sensitivity function of the GA-based sensor is highly non-linear as shown in Figure 5.7. For qualitative measurement, a more precise device would be needed.

5.3.1 Vibration device

As stated above, we built our own device to estimate frequency characteristics of GA based sensors. In this section, we will describe the construction of the device shown in Figure 5.13.

To generate vibrations of given frequency contraption consists of speaker attached to 3D printed holder. The speaker is driven by a D-class amplifier module board. Our first design was supposed to deliver vibrations directly from the speaker's membrane to the tested sensor. However, in this configuration we observed in the sensor's outputting signal's spectrum little spikes at given frequencies even when no mechanical contact was present. We suspect that due to the fluctuating magnetic field around the speaker, electro-magnetic induction is present either in the GA it self or the leads used to attach the sensor to the reading electronics. To overcome this issue we moved the GA sensor 12 cm further away from the speaker in the speaker coil axis. At this distance, no such spikes in the signal spectrum were present. The mechanical vibrations are then transferred using a diameter metal rod 2 mm. The rod is supported by two columns. Since the speaker is a rather weak actuator, we lubricated the rod to lower friction between its surface and supporting columns.

Since our speaker was only a generic speaker without any frequency characteristics provided by the manufacturer, we used the ADXL326BCPZ accelerometer to estimate the amplitude of the vibrations. An accelerator is attached to the rod, which transfers vibrations in such a way that the motion created by a speaker is collinear with the Y-axis of the integrated circuit. This accelerometer has analog outputs, which can be connected directly to an oscilloscope. Next, the manufacturer ushers band width up to 1600 Hz in the X and Y axes and 550 Hz in the Z axis. Unfortunately, manufacturer does not provide frequency response for this product, so we cannot take its outputting value as a ground

truth. We cannot see that there is no change or even resonance in frequency response of the said accelerometer. We can only expect that with the said bandwidth the frequency response will not be curved too much, which is a very vague term.

To make our measurement accurate, first we would have to calibrate our accelerometer by precise vibrations of exact amplitude, but if we had such a reference device, we would use it directly. This is the reason why the measurement using this device provides only an estimate of the frequency response. Still, the sensor gives us some basic information about oscillations present and, at the very least, confirms the frequency at which is currently used for measurement.

Finally, the GA sensor is attached to the device the same as it would be mounted to the grippers finger. The contact and level of press applied to the sensor is set using a bolt and a spring. The spring presses the mount for in opposite directions, away from the speaker, ensuring the mount's movement to be the same as the head of the bolt.
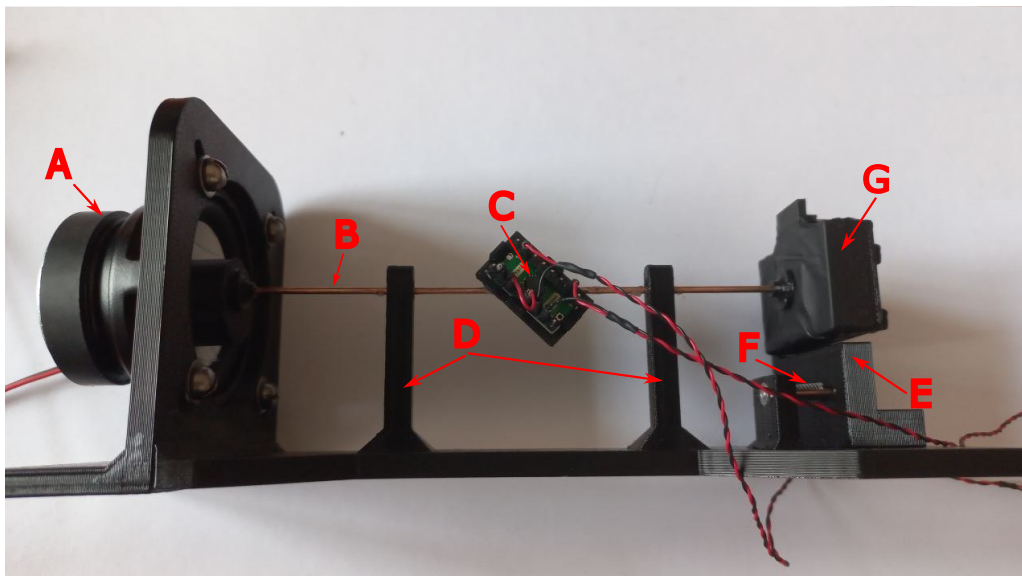
Figure 5.13: Vibration generating device. **A)** speaker, **B)** rod transferring vibrations, **C)** accelerometer integrated circuit, board is tilted with 45° angle so the Y axis is collinear with the rod B, **D)** supporting columns, **E)** mount for sensor to be attached, **F)** spring ensuring mount E to return when tightening screw is loosen, **G)** attached GA based sensor.

■ 5.3.2 Frequency response of GA sensor

When measuring the frequency response we used the PicoScope 2004A computer oscilloscope to measure the output voltage of GA sensor's reading electronics and the accelerometer output Y. The gain of the amplifiers was set manually. As shown in section 4.2 for every gain set, the frequency range of the amplifiers is significantly higher than the expected frequency range of sensors. During this experiment, the output filtered by a high-pass filter was measured to filter out only AC components of the measured signal.

To ensure galvanic insulation between the speaker's amplifier and the rest of the setup, a separate supply was used. We wanted to prevent cross-talk of signal driving the speaker to sensing part over supply tracks. The amplifier was powered by a battery pack that provided a 5V output voltage and a maximum output current of 2A. Next, we could not, due to the wanted galvanic insulation, use the function generator embedded in PicoScope 2004A. Instead we used cheap substitution in the form of audio output of a mobile phone Samsung Galaxy A32 and application to drive audio output at given frequency, controlling the speaker. As untrustworthy as this solution might seem, we did not encounter any issue. The accuracy of set frequency was checked for each measurement by PicoScope 2004A and no frequency error was observed.

The frequency characteristics were measured on discrete frequencies. In every iteration a new frequency was set to the speaker and confirmed by examining spectrum of the accelerometer outputting signal. The next voltage level in dBu on the observed frequency was recorded for both measured outputs. The functionality of fast Fourier transform (FFT) measurement and computation of voltage level is embedded in PicoScope computer application.

The accelerometer measures, of course, acceleration; however, we are interested in displacement. For harmonic oscillations we can derive

$$x(t) = A \cdot sin(2\pi ft + \varphi), \tag{5.8}$$

$$\frac{d^2x(t)}{dt^2} = -4\pi^2 f^2 A \cdot sin(2\pi ft + \varphi) = 4\pi^2 f^2 A \cdot sin(2\pi ft + \varphi + \pi). \tag{5.9}$$

To obtain displacement amplitude from acceleration amplitude we can derive

$$A_D = \frac{A_a}{4\pi^2 f^2}, \tag{5.10}$$

where A_D is amplitude of displacement and A_a is amplitude of acceleration. Since voltage level is computed as

$$L(V_x) = 20 \cdot log_{10}\left(\frac{V_x}{V_{ref}}\right), \tag{5.11}$$

the input-output characteristics is obtained for each measurement as

$$H(f) = 20 \cdot log_{10}\left(\frac{V_{GA}}{\frac{V_{acc}}{4\pi^2 f^2}}\right) = 20 \cdot log_{10}\left(\frac{\frac{V_{GA}}{V_{ref}}}{\frac{V_{acc}}{V_{ref}}}\right) + 20 \cdot log_{10}\left(4\pi^2 f^2\right) =$$

$$= 20 \cdot \left(log_{10}\left(\frac{V_{GA}}{V_{ref}}\right) - log_{10}\left(\frac{V_{acc}}{V_{ref}}\right) + log_{10}\left(4\pi^2 f^2\right)\right) =$$

$$= L(V_{GA}) - L(V_{acc}) + 20 \cdot log_{10}\left(4\pi^2 f^2\right).$$

Finally, to correct for phase shift data, we subtract 180° from the measured data.

During this experiment, we examined samples labeled as "5R" and "20R" as in previous tests. Frequency responses were measured for two pressure levels, labeled "light" and "tight". The pressure is set by pressing the sample against the rod of the measurement device using

the bolt as described in Section 5.3.1. The light pressure of the vibrating device that was turned off described above just gently touched the sensor, and the sensor output voltage decreased little. The second pressure was set by tightening the bolt by 2 mm. Motivation for the two sets of measurements was to see if the weather sensor would be more sensitive when GA is more deformed and forms denser material. In denser materials, vibrations may travel more easily.

In Figure 5.14 are visualized measured frequency responses. The magnitude spectrum H results in such high values because the output signals of the accelerometer and GA sensor are in a certain ratio. In these graphs the curve of magnitude spectrum is more important rather than amplitude.

Despite the fact that the accelerometer used is capable of measuring oscillations up to 1600 Hz, we measured the frequency response up to 1300 Hz. At higher frequencies were amplitudes of vibrations too low and signal outputting from our electronics was barely distinguishable from noise. To measure for higher frequencies, a better vibration plant would be needed.

From the measured response 5.14 we can observe that the harder the press is, the less curved the frequency characteristics. The measured frequency range is quite high. Regarding band width estimation, strictly speaking in electronics theory and control systems, the band width is defined as a point in the frequency spectrum, where magnitude decreases by 3dB from the middle of the band. However, in our case, the transfer function is rather complex, and there is no simply distinguishable band where the magnitude would be constant.

The phase shift spectrum was measured in the time domain. At certain frequencies was the output of sensors too noisy to correctly measure the phase shift between signals. This case was present when the frequencies were lower than 200 Hz for the tight press experiment. For these frequencies, no phase shift was measured. In the rest of the phase spectrum we can see changes around the same frequencies as in the magnitude spectrum. Specifically, we can see spikes around frequencies where spikes occur in the magnitude spectrum.

Next, we would like to compare our results with the other sensor. According to the manufacturers manual [4] of the BioTac sensor, the frequency range of the hydraulic pressure sensor is limited by a low-pass filter of up to 1040 Hz to prevent the effect of aliasing. This range is comparable to the range of our sensor. However, in the given manual, we cannot find its transfer function that shows the response to a given frequency. This frequency dependence of the BioTac sensing threshold is a topic of article [21]. In this article, the perceptual threshold to the vibration amplitude was measured. The BioTac finger shows a rather complex transfer function. This frequency response was obtained by the piezoelectric actuator AE0203D16F from NEC / TOKIN. This piezoactuator is said to have a blocking force large enough not to be affected by a touch of the sensor; therefore, no feedback system was used [21].

From the comparison data in Figures 5.15 and 5.14 we assume that our sensor shows a frequency range similar to that of the BioTac finger. The frequency response of both sensors is quite complex. When tight press is examined, we can notice a certain rise in magnitude spectrum. In Figure 5.15 we can also see a similar behavior; note that the figure

59
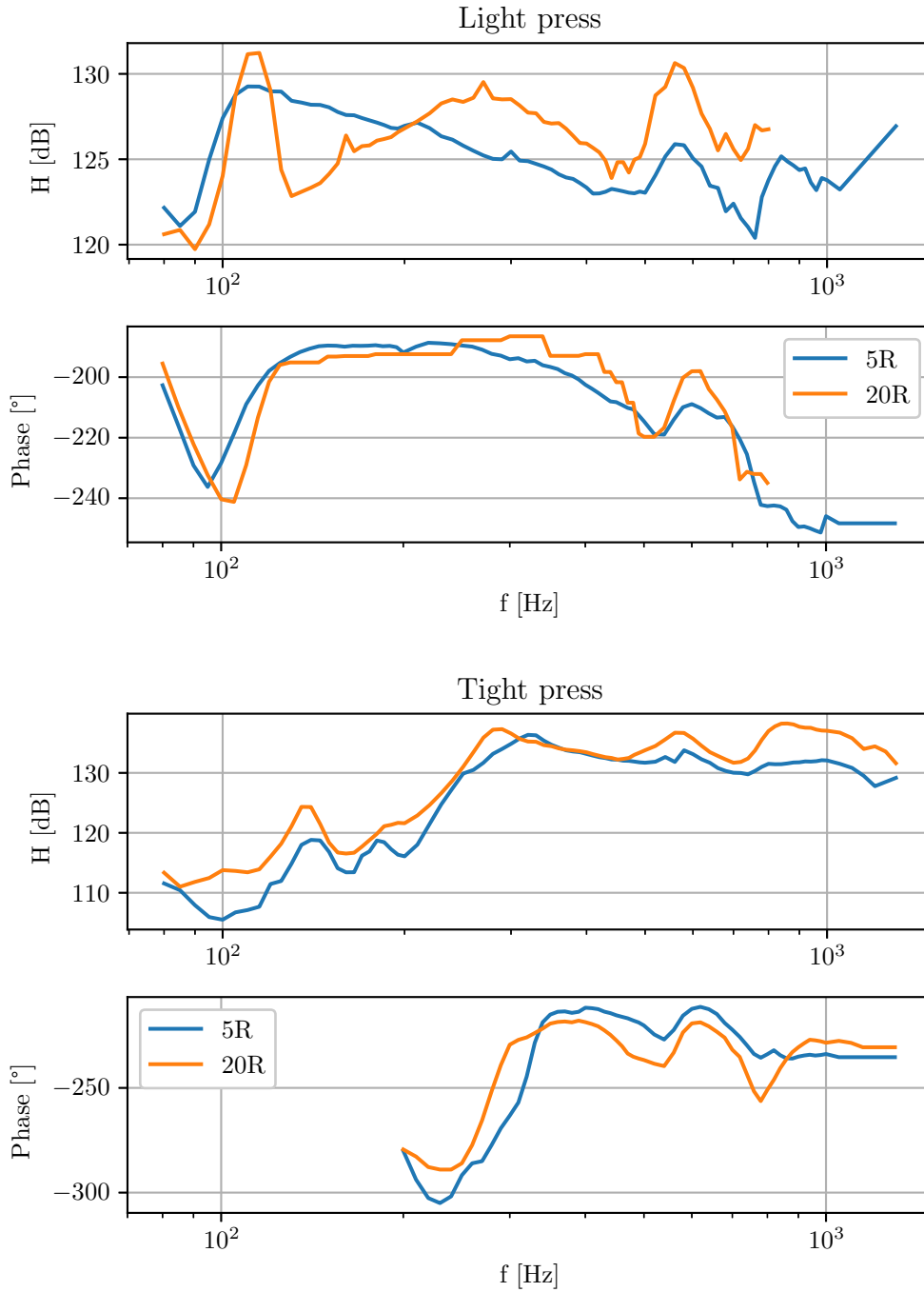
Figure 5.14: Frequency responses of sensors "20R" and "5R" for light and tight presses.
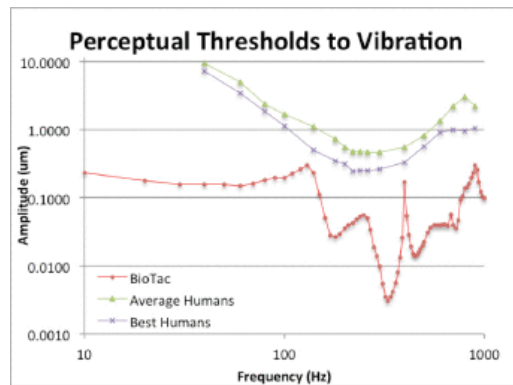
Figure 5.15: Frequency Sensitivity Plots. Green trace = average subject performance; purple trace = best subject performance; red trace = BioTac sensitivity. Figure and caption from [21]

shows threshold, therefore, sensitivity is rising. An increase in sensitivity of our sensor occurs in different frequency ranges.

Our measurement procedure is, as stated above, not very robust with respect to the unknown frequency response of the accelerometer used. On the other hand, the responses obtained from the measurement show similar results to those published in article [21]. Moreover, our sensor is based on material, which is capable of oscillations in the range of MHz. This capability is a promising feature for the GA-based sensor to be able to measure high-frequency vibrations. So, even though our measured data are not ground truth, they might not be too far from reality.

5.4 Durability test

During our sensor development we were interested in the robustness of our sensor. We tested one of our first sensors to see what work load it can withstand. The sensor was constructed using thin sheets of nitrile and medical tape as described in Chapter 4.1.2, so we expected it to show significant tears very easily.

We set up an experiment during which the Kinova Gen3 robot uses the robot Robotiq 2f-85 gripper equipped with our sensor to lift the cobblestone 1000 times. This task is not very gentle on the sensor. This kind of experiment also tests the repeatability of the sensors R_0 when repeatedly compressed and released with the high forces needed to grasp and lift the cobblestone.

Figure 5.16 shows the time series of the stress experiment. After all 1000 lifts, the sensor showed no signs of damage visible to the naked eye. Unfortunately, our laboratory is not equipped with any microscope to view more in detail. We did not expect the sensor to survive the experiment at all and record the iteration when it broke down, but the sensor exceeded our expectations.

Regarding repeatability, we can see that the sensor value R_0 shifts during the experiment. However, this could also be caused by the long-term drift discussed in Section 4.1.4 as the
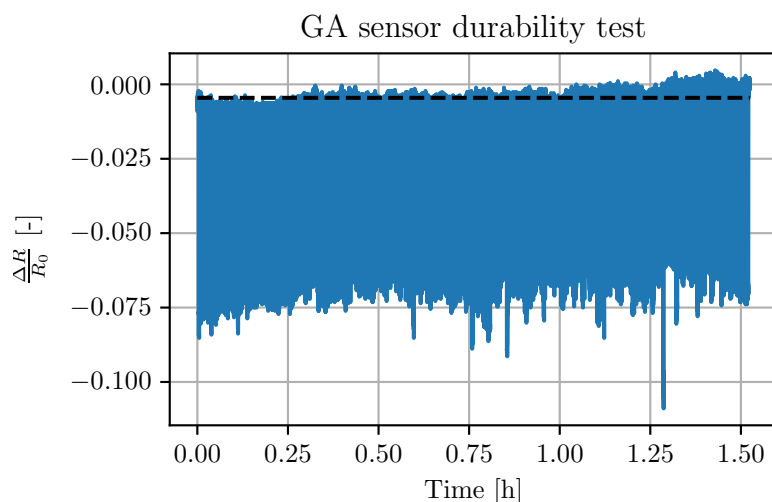
Figure 5.16: Graphene sensor stress-test. Black line shows mean value of sensors R_0.

experiment took more than 1.5 hours to complete. Regarding the response of the sensor when pressed, even though the gripper was always closed to the same distance, the sensor response shifted. This could be caused by a certain backlash of the gripper or an irregularity in the stone surface.

5.5 Sheer forces

During our experimentation, we observed a significant sensitivity of the sensor to sheer forces. This was initially observed during the stress test, the sensor reacts by increasing resistance when the stone is lifted. As shows Figure 5.17 This dependency however does not seem to be easily to exploit for purposes of slip detection. The sensory output is without prior knowledge indistinguishable from the change in applied pressure. The possible use of this phenomenon might be the weighting of objects at hand. The robot gripper equipped with a GA-based sensor would grasp the object and lift it. By sensors the output change might be proportional to the mass of the weighted object. Due to the limited time for experiments, we were unable to properly research this topic.

5.6 Temperature dependency

As reported in article [12] the resistance of the graphene aerogel sensor does not show a temperature dependence. This is a major advantage. We decided to replicate this experiment to ensure that our final design of the multi-taxel sensor preserves this feature.

As a source of heat, we used the TESLA TR64B power resistor. This 100 W resistor with resistance of $100\,\Omega$ was connected to the Voltcraft DPPS-60-10 power supply. The power source was set to a constant current mode up to 0.5 A which was modulated to adjust the slope of the increase in temperature.
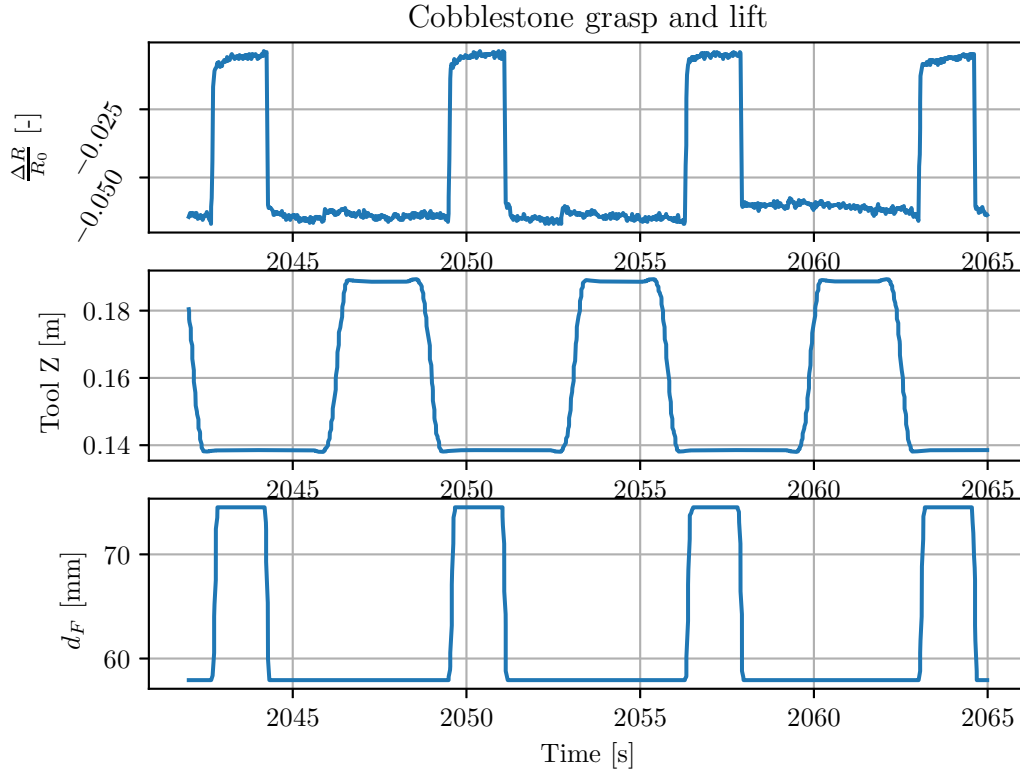
Figure 5.17: Time series of three iterations of cobble lift-ups. The first plot shows the response of the GA sensors. The second shows the grippers Z coordinate. The final plot shows the distance between the gripper's fingers. Sensor shows sensitivity to sheer forces when robot lifts gripper with cobble stone.

The K-type thermocouple was used to measure temperature in combination with the TM-902C thermometer. The measuring end of the thermocouple was neither insulated nor encapsulated in any kind of protective enclosure, so the sensitivity and response time of the thermocouple were as high as possible. The thermocouple was attached to the sensor using kapton tape. During this experiment temperature was set in a range from room temperature of 25°C to 50°C. We avoided higher temperatures to prevent damage to plastic and nitrile parts. To measure resistance we used our amplifier and multiplexer electronics described in section 4.2. The output voltage of the measuring chain was measured using the PicoScope 2004A computer oscilloscope. When triggered correctly, the signal showed at which point in time the taxels were switched. Using PicoScope measurement utilities, we measured the mean value of output voltage for each taxel (by computing the average between rulers on the time axis). As is visible in the Figure 5.19, output voltage, which is in our measurement directly proportional to the resistance, stayed unchanged. The temperature dependence for each sensor does not show a consistent trend. From this measurement we then assume that our sensor preserves the no-temperature response. The only article showing such dependency is [9], where the sensor based on PDMS doped with multi-walled carbon nanotubes shows in the same temperature range a shift of 2%.
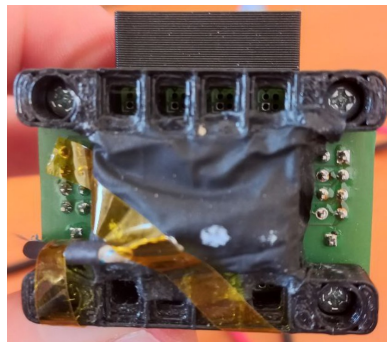
(a) Thermocouple taped to the sensor
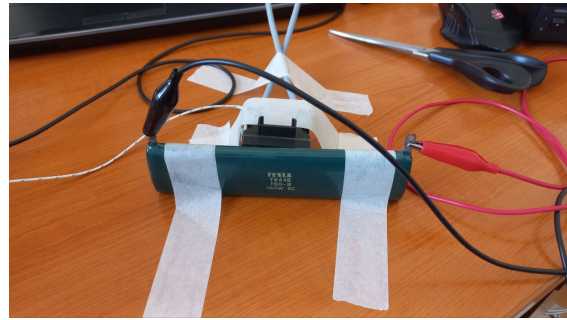
(b) Experiment setup

(c) Thermometer TM-902C
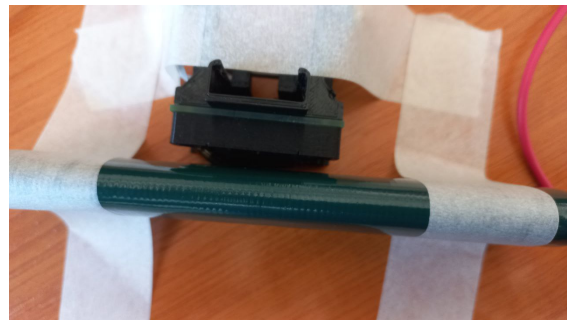
(d) Experiment setup viewed from above

Figure 5.18: Temperature dependency estimation experiment setup
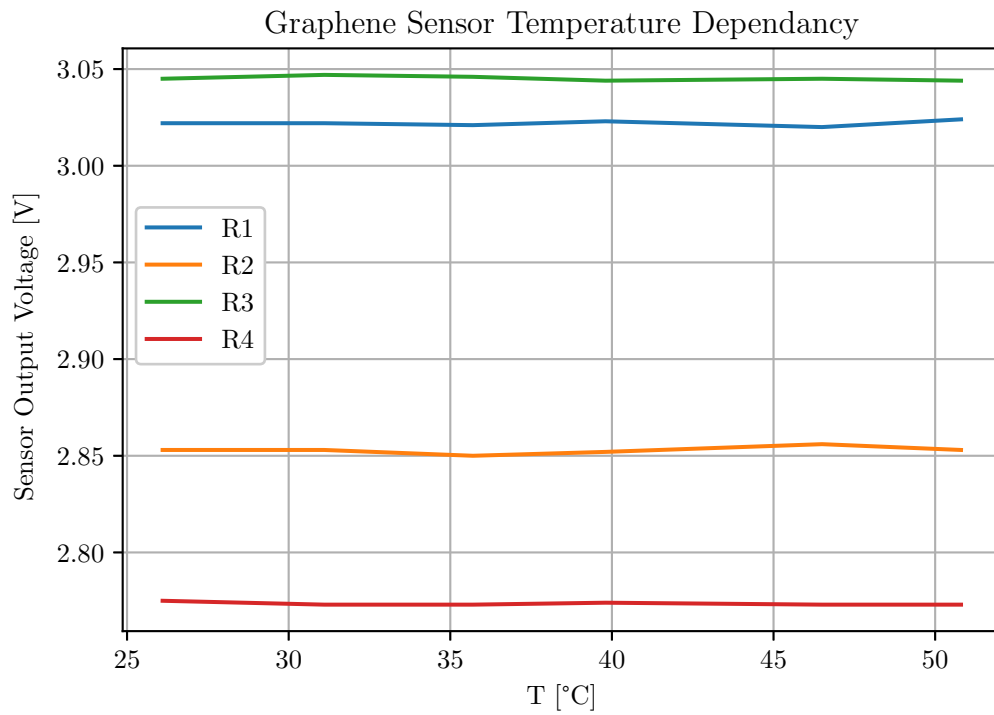
Figure 5.19: Graphene sensor temperature dependency in rage from 25 °C to 50 °C

■ 5.7 **Summary**

In this section we will summarize our observations for the conducted experiments and compare our results with other sensors. Most relevant data are summarized in Table 5.3.

Sensor	Maximum Sensitivity	Dynamic range	Frequency range	Temperature dependency
Piezoresistive Pyramid PDMS/MWCNT [9]	$-1.10\,\mathrm{kPa}^{-1}$	0-7.5 kPa		$\frac{\Delta R}{R} = 2\%$ per 25 °C
Piezoresistive Pyramid PDMS/PEDOT:PSS [3]	$4.88\,\mathrm{kPa}^{-1}$	0.37–5.9kPa		
Piezoresistive Pyramid graphene oxide [8]	$-5.53\,\mathrm{kPa}^{-1}$	0–1.5 kPa		
Piezoresistive Hemisphere PDMS/CNTs [3]	$196\,\mathrm{kPa}^{-1}$	0-5kPa		
Piezoresistive PDMS/Ni [10]		0-2 MPa		
Capacity Pyramid PDMS/ITO [3]	$44.5\,\mathrm{kPa}^{-1}$	0-100 Pa		
Capacity Pyramid PDMS/ITO/PET [3]	$41\,\mathrm{kPa}^{-1}$	0-5 kPa		
Capacitive [5]	$0.0196\,\mathrm{kPa}^{-1}$	0-1MPa		
Contact resistance EVA foam [18]		150 kPa		
Contact resistance PTFE [18]		0.1-2 MPa		
Piezoresistive Sand Paper graphene [3]	$2.5\,\mathrm{kPa}^{-1}$	0-50 kPa		
Thumbsized Optical [13]		0.03–2 N		
Magnetic [16]		1–300 kPa		
Magnetic ReSkin [7]		0–2 N		
BioTac [4, 21]	27.39 bit/kPa	0-100 kPa	>1 kHz	
GA-based	$-4.85\,\mathrm{MPa}^{-1}$	0.003-15.625 MPa	>1 kHz	$\frac{\Delta R}{R} = 0$ per 25 °C

Table 5.3: Comparison of GA-based sensor with other sensors. When the cell is left blank, the given parameter could not be found. Minimum detectable pressure for our sensor is based on noise of the electronic system.

Our sensor in comparison to other sensors shows a remarkably high dynamic range. In comparison to most existing sensors, our sensor is capable of measuring forces of at least one order higher. The sensitivity is, on the other hand, much smaller; however, with respect to the wide range of applicable forces, we assume that this is not a bad value.

Regarding the frequency capabilities of existing sensors, the only example of frequency characteristics we found was for the BioTac sensor only. In comparison to this sensor is our measured frequency range equivalent. Our tool to measure frequency characteristics was

not ideal and lacks a precise calibration; however, the data obtained from these experiments show certain similarities with frequency characteristics of the BioTac sensor.

Finally, we compare temperature dependencies of examined sensors. This parameter was also not a topic of most of the studies we observed. In contrast to a sensor based on multiwall carbon nanotubes, our sensor shows no temperature trend. On the other hand, the temperature dependency of multi-wall carbon nanotubes is not in our opinion too significant, however, it can impose a complication for precise measurement.

Chapter 6

Robotic grasping

In this chapter we introduce our experiments in the field of tactile grasping. These experiments were conducted mainly to show the performance of the graphene aerogel-based sensor in a practical task. For these experiments, we used the multitaxel sensor shown in Figure 4.12. We showed in Chapter 5 results of experiments that estimate the sensitivity, dynamic range, and frequency response of the GA sensor, but here we were also interested in the performance in the closed-loop control system.

During these experiments, several objects with different mechanical properties, such as elasticity and durability, will be grasped. The objects were fragile, such as disposable plastic cups and paper (grasped from the thin side). Grasped objects were selected to be soft and fragile, but also not break down in the event of grasp failure. Furthermore, damage to the grasped object should not cause damage to the manipulator, gripper, or surrounding. For this reason, we did not include objects such as raw eggs, various fruits, or other objects, which could potentially damage the setup.

6.1 Gripper Robotiq 2f-85

In this task we concentrate mainly on the gripper control, because it is a gripping task. We used a Robotiq type 2f-85 gripper designed for collaborative operations. The type "2f" refers to two fingers, which the gripper has, and "85" corresponds to 85 mm of the maximal distance between the fingers. The maximal distance was further lowered by attaching our sensor and the dummy version of the sensor. At the time of our grasping experiment, we had only one sensor constructed. We did not want the mechanism to be asymmetric, so we added a plastic part of the same size as the sensor. This lowered the maximum distance between the fingers to ~60 mm.

The gripper allows two modes to be operated, positional and velocity, which we both use. In position mode, the distance between the fingers is set, where 0 corresponds to the closed gripper. In the velocity mode, the speed of the fingers is set. The negative speed closes the gripper.

To command the gripper, we used the ROS Kortex driver. This implementation allowed us to keep using ROS for the control of the robot and gripper. The disadvantage of this approach is the rather low speed of communication. The ROS version of the Kortex driver was able to communicate at a maximum rate of 40 Hz with the gripper. According to the manual, the usual rate for sending commands is 200 Hz [35]. The 40 Hz rate is very low

compared to the 1 kHz used in article [22]. However, we did not have another option than to use the 40 Hz interface. It was enough for the testing purposes of our task.

The gripper provides as a feedback motor current which is proportional to the applied forces. We compare the signal from our sensor with the said current response. This allowed us to compare our sensor with a commercial solution.

For typical DC motors, the relationship between the current through the winding and the torque is linear. In case of given gripper, rotation motion is converted to linear using double-leverage mechanism. This probably results in the conversion of applied force to motor current being nonlinear, which is a disadvantage because it complicates potential control. This mechanism also shows certain backlash, as this gripper is designed to be adaptive for human-robot collaboration tasks. To overcome the friction powers present in the mechanical system, a certain current flows through the motor winding even when no contact with the object is established. The next disadvantage of such force feedback is that it can be used only when the gripper motor is set in motion; otherwise, the gripper brakes are used and the motor disconnects from power; hence, no current flows. On the other hand, our sensor is independent of motion of the gripper. For these reasons, we believe that our sensor will react faster and provide better feedback about grasp.

One of the concerns we had next regarding the control is the jitter effect. Our control loop consists of the sensor sending data to the PC, which computes control action and sends the command to the gripper. During control, we did not encounter any issues with latency, therefore, we conclude the communication latency is appropriate for our task. When driving the grasp, we did not encounter any issues with jitter; however, our control was rather slow. In case of control with the higher rate, we would prefer the option to control gripper directly using the micro-controller used to read sensory data to also drive the gripper.

∎ **6.2 Control strategy**

While grasping a generic object with a robotic manipulator, several problems must be solved. In addition to detecting the position and orientation of a given object, its physical properties are also important. From physical properties such as elasticity, deformability, and fragility, we can derive the grasping force. Estimating these forces automatically is a rather complex task and deep learning can be utilized to accomplish this [20].

Next, the quality of grasp should be assessed; otherwise, we risk the grasp object falling out of the gripper. Slip detectors are designed for this purpose. There are several implementations varying in performance and complexity. Some are based on detecting spikes in signals processed using high-pass filters, while others are based around neural networks.

In our case, we were more interested in the performance of the sensor than implementing very complex control algorithms. [22] Needless to say, these highly sophisticated algorithms would be very time consuming and perhaps a topic for the thesis. Our goal was to show that it is possible to use the GA based sensor in some way of tactile grasping.

In our implementation, we are inspired by article [22]. The algorithm presented in this paper divides tactile manipulation into several steps: close, load, lift and hold, replace, unload and open. In the close stage, the manipulator is set to position to start grasping and ends when the grasped object surface is detected. To process multi-taxel sensory data sum over all taxels on each finger is used. The surface is detected by either an applied force or a signal representing the applied force processed by a high-pass filter that reaches a certain threshold. The condition must be fulfilled for both fingers for the condition to trigger. In the load stage, the amount of pressure to apply is estimated by a brief pause and evaluating the maximum force detected while waiting. This force is highly dependent on the closing speed. The load stage ends when the desired force is applied and the gripper's finger speed is below a certain threshold. In the next stage, lift and hold, the manipulation is performed. During this phase, a firm, yet gentle grip is maintained, detecting occasional slippages. Slips are detected by detecting high-pass or band-pass-filtered signals of the force sensory signals reaching above a given threshold. This phase is terminated by other software when manipulation is done and the object is only a few centimeters above the desired location. In the replace phase, the grasped object is placed in the desired location at moderate speed. In the last two phases, the grip is released. When unloading, the applied force is lowered at a given pace. Finally, the gripper is opened at constant speed using the positional controller [22].

The algorithm solves the full pick-and-place operation task using professionally manufactured and well-calibrated sensors. We assumed that to implement the algorithm completely would be very time consuming. Instead, we only implemented the close, lift and hold phases. By skipping the load phase, we had to manually estimate the amount of pressure for each object.

Gripper is in [22] controlled using the PD controller to drive the position using motor effort. To drive the force, another P controller was used on top of the position control. The controller uses different P constants based on the sign of the error signal to flight oscillations when applying desired gripping force.

Our grasping algorithm is as follows. First, we recalibrate our sensors. Then we close the gripper at constant speed. Instead of using sum over all taxels as introduced in [22] as a feedback signal, we used mean value over all taxels. We find a more natural scaling by number of taxels approach. When we detect contact with the surface, we go to the PD controller to set the desired force.

■ Sensor recalibration

As shown in Section 5.1.2, the features of GA based sensors tend to drift over time. The calibration process is too tedious to run on a regular basis. Instead, we introduce a different approach.

We would like to recalibrate the sensors before each grasp. The next condition was to keep the process as general as possible, without any additional devices or objects. To solve such a task, we decided not to calibrate our sensor for exact physical units but for the qualitative scale [0,100], where 100 represents the maximum force applicable by Robotiq

2f-85 and 0 without applied force. This allows us to use only the gripper it self to recalibrate our sensors. The disadvantage of this approach is that we have only two points usable for calibration, when the gripper is opened and no force is applied, and when the gripper is fully closed and maximal force is applied. These two points are not enough to estimate the parameters for the model 5.4 where many more points are needed. However, we can use two points to linearly adjust the output of the model 5.4. For each taxel, the function 5.4 is calculated with parameters in Table 6.1. Coefficients shown in Table 6.1 were obtained

A	B	C	D	E	F
1000	10	5	-6	17	-16

Table 6.1: Sensors generalized constants

by scaling calibration results for the sensor "20R" shown in table 5.1. The output of the function is then fed to the linear function

$$\hat{F} = A \cdot F(x) + b, \tag{6.1}$$

These operations do not result in a linear response for all taxels. The output is still non-linear but less curved. This is not an optimal result but, as further shown, functional enough to allow force control.

The complete calibration procedure is as follows. First, the Kinova manipulator moves the gripper a few centimeters away, where no object is expected. Then the reading electronics pipeline is commanded to reset, which means that the current resistances of the taxels are set as R_0 and the amplifications for each taxel are adjusted. The output of function 5.4 is saved for each taxel. The gripper is then closed as much as possible. Since the pipeline uses a moving average to reduce the noise in the data, the procedure stops for a few milliseconds. After this pause the current output of Function 5.4 for each taxel is saved again. Parameters A and b for i-th taxel are given as

$$b_i = F_i(0), A = \frac{F_i(100) - F_i(0)}{100}, \tag{6.2}$$

where $F_i(0)$ is result of Function 5.4 for i-th taxel when no force is applied and $F_i(100)$ when maximum force is applied. The parameters obtained are then sent to the reading electronics and the gripper is fully opened. Finally, the manipulator returns to the original place.

■ **6.2.1 Closing and surface detection**

Similarly with the control strategy introduced in [22] we start our grasp by closing the gripper at a constant speed. For this purpose, we used velocity controller of the gripper. We set the closing speed to 10 % of the maximum velocity. Higher velocities resulted in overshoots in the force control stage, as the gripper could not be stopped fast enough when the surface contact was detected. We assume that a rate of 40 Hz is the reason for this behavior.

To detect contact with the surface, we used a similar method to that in [22]. Instead of signal processing by high-pass filter of sum over all taxels, we used first-order differentiation

of mean value over all taxels. We set the contact for established when condition

$$\left|\hat{F}'_{mean}\right| \geq C_{contact},\tag{6.3}$$

is true, where

$$\hat{F}'_{mean} = \sum_{i \leq N} \frac{1}{N}\left(\frac{d\hat{F}_i}{dt}\right).\tag{6.4}$$

The parameter N is the number of taxels, and $\hat{F}_i$ represents the i-th pre-processed taxel signal. The constant $C_{contact}$ was experimentally established as a level reasonably higher than the maximum noise in the signal. In our case $C_{contact} = 0.2$.

This implementation is simpler than the one presented in [22], but still worked well for our purposes. There were very few false detections. In contrast to [22], our gripper was equipped with only one set of tactile sensors, which means that contact was detected only for one finger of the gripper. The grasped object had to be located in the middle between the fingers for the best grasp performance. In case of contact detection in [22] the contact estimation condition was more complex because both fingers of the gripper are equipped with tactile sensors. The condition must be activated after contact of both fingers is established. In our case, we have no way of detecting contact of the other finger, which counterintuitively leads to a simpler condition.

◼ 6.2.2   PD force controller

In our case, the force controller is invoked immediately after the contact is detected, in contrast to the algorithm presented in [22]. In their case was the stop also caused by sensor rate to be much slower than control rate. Their sensors provided feedback with 24.4 Hz, whereas the controllers ran with 1 kHz. In our case, the roles are reversed. Our sensor feeds the value with 100 Hz, yet our control loop is capable only of 40 Hz. Furthermore, in [22] this time is used to estimate the force needed to grasp the object, we selected the amount of force manually.

To control the force applied, we designed a controller that drives the gripper's velocity. The controls were given as

$$e(n) = \hat{F}_{des} - \hat{F}_{mean}(n),\tag{6.5}$$
$$v(n) = K_P \cdot e(n) + K_D \cdot (e(n) - e(n-1)),\tag{6.6}$$

where $\hat{F}_{des}(n)$ is desired force in pseudo-calibration units described in 6.2, $\hat{F}_{mean}(n)$ represents mean value over all taxels. The constants K_P and K_D were experimentally tuned for each grasped object, as each object showed a different force response. The controller was implemented for discrete time, so, instead of time, the signals are functions of step n.

Our first attempt to control the grip force used the velocity mode of the Robotiq gripper. Although this gripper is said to have 8-bit velocity resolution, the resulting control was very smooth. The resulting movement oscillated even for very low control signals. We assume that this is caused by a limited resolution of the inner velocity measurement system and the low control rate of 40 Hz.

71

To overcome this issue, we switched to gripper control mode to position one. Instead of sending commands with velocity, we send position where we expect the fingers to be in the next iteration of the control loop. To compute the position we simply take

$$x_{des}(n+1) = x(n) + \frac{v(n)}{f_{con}}, \tag{6.7}$$

where $x_{des}(n+1)$ is distance between fingers which we desire in next iteration of the control cycle and $x(n)$ is current distance between fingers. The velocity $v(n)$ is calculated using the equations 6.5 and 6.6. The parameter f_{con} is the controller rate in our case $40Hz$. It is true that this computation of desired position is just a guess of the next position, as we assume infinite acceleration for fingers of the gripper. However, this assumption does not seem to cause any issues with respect to the Robotiq 2f-85 high acceleration capabilities and low control rate.

■ 6.2.3   ROS structure of grasping application

The application of grasping was developed within ROS. Figure 6.1 we show the structure of the distributed system.
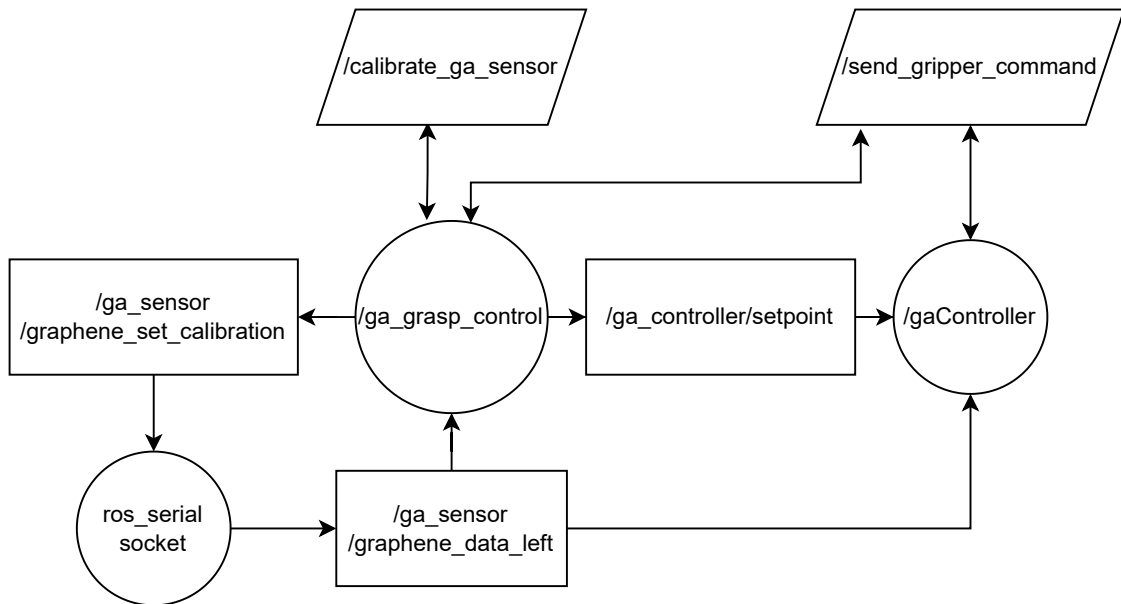
Figure 6.1: Structure of ROS application. Circular fields represent ROS nodes, square boxes topics and parallelogram services.

One of the most important nodes in the control system is the socket node implemented by the ROS serial library. This node ensures communication with low-level hardware, our measurement electronics system. Sensory data are published in a given topic, as shown 6.1. The node `/ga_grasp_control`, which controls the grasp sequence, subscribes to sensor data feedback. In the recalibration phase, the data are captured by **/ga__grasp__control** node. The calibration is computed by the service `/calibrate_ga_sensor`. We implemented

calibration in service variant for cases in future where it would be required to be called by multiple nodes. The formula 6.1 to compute calibration is rather simple and is easy enough to be implemented as a simple regular function. Even though we decided to use the service structure for potential future improvements. If the calibration procedure changes, only one part of the system is modified. The computed sensor calibration is sent to device over socket node using `/graphene_set_calibration` topic.

The gripper `/send_gripper_command` service is used to control the gripper. This server provides communication with the gripper used. Despite the fact that the service responds only with Empty message type. Also, this node was not implemented by us. As mentioned earlier, ROS Kortex library is used to control the Kinova Gen3 robot and the Robotiq 2f-85 gripper.

After the recalibration is executed the control setpoint and controller constants K_p and K_D are published to given topic. The node `/gaController`, which implements the closing, surface detection, and PD control, initiates the grasp after receiving the setpoint information.

Most of the nodes and services are implemented in Python. The only exception, from the nodes which we programmed ourselves, is the `/gaController` node. This node is written in the C/C++ language. For this node, we needed a higher evaluation speed to communicate with the `/send_gripper_command` service. When we tried to implement this node in Python, the control rate was significantly decreased below 40 Hz.

As stated above in this chapter, our feedback for our system must travel through interface controller running on PC and then control is applied through another interface to the gripper. This architecture is not optimal with respect to communication delays and jitter. Next, we do not use real-time version of ROS, which could provide certain evaluation time guarantees. We are well aware about its existence, however utilizing such system would be very time consuming, needless to say, we are not certain about third party software to be compatible with real time ROS variant.

6.2.4 Control results

In this section we will present results of the grasping sequence for different objects. Some objects show certain difficulties when grasped with respect to their shape. For each object, we describe what was challenging. Next, gripper's fingers were equipped only with line of sensors which do not cover the whole finger area. These matters make grasping difficult in some cases. We will present grasping results in order given by object grasping difficulty.

■ Paper tea box

First object we will present is a standard empty paper box for tea. This box is relatively rigid.
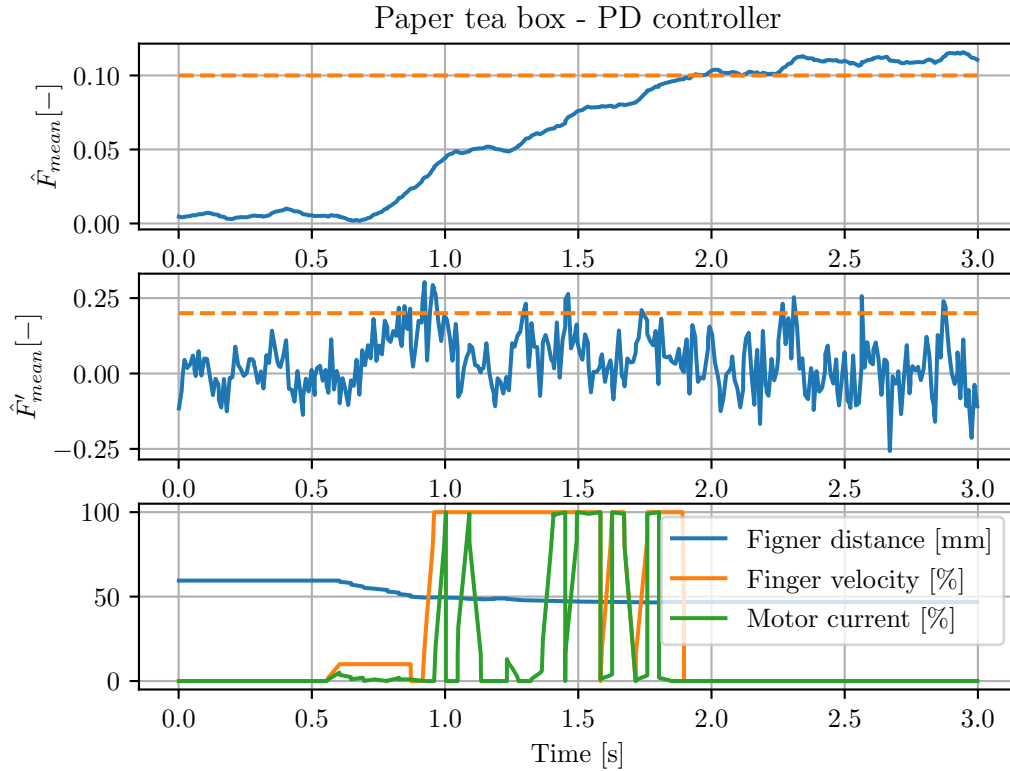
Figure 6.2: Paper tea box grasp and object contact detection. The dashed line in the first chart represents the setpoint in the pre-processed value. The second differentiated signal is shown. The colored line shows the contact detection threshold.

In Figure 6.8 we see detection of object surface at the time ~0.9 s. At this time, the value of $\hat{F}'_{mean}$ reaches a set threshold. Compared to the motor current of the gripper used, no significant response is present. The current response is not as sensitive to applied force as our sensor. At the time of contact detection, the fingers are stopped and the control is switched to the PD controller. The PD controller does not follow the setpoint with zero error; to do so, an integral component of the control would be needed. However, when the integral component was used, it resulted in higher overshoots and, because of the low position resolution of the gripper, also in oscillations. Moreover, such an error is not significantly high, and the grasping task was successful. In this case, we prefer lower control precision with lower overshoots. High overshoots could possibly damage the grasped object, and oscillations lead to dropping of the object. In Figure 6.3 we can see the grasped tea box.
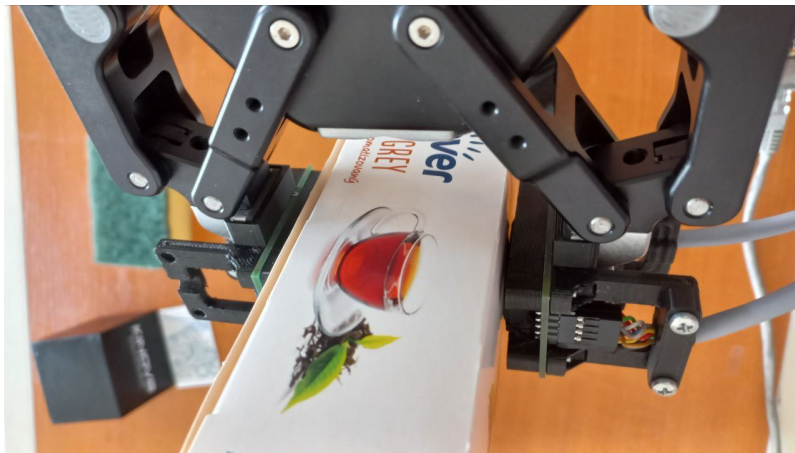
Figure 6.3: Grasped paper tea box. No sides are bent.

Kitchen sponge

This object is also rather simple to grasp. It is soft but has a cubic shape. Also in this case current feedback from motor shows no signs of contact detection. The reversing forces generated by the sponge are in this stage of press too low for the gripper to be measured.

Plastic cups

As one of most challenging objects to grasp shown to be plastic cup. This very low-cost container is very fragile and even humans usually have problem to grasp those without bending.

In ours the grasp was even more challenging due to the circular shape of the cup. Our sensor was composed only of a line. The easiest way to ensure contact with at least one taxel would be to grasp the cup from above. In this way, the line would be tangent to the circular surface. Unfortunately, the upper part of the cup was too large to fit in the gripper with the sensor attached. However, the cup was conic, so we decided to grasp it from the side as shown in Figure 6.7. In this case, the robot must be oriented very precisely with respect to the cup to ensure any contact with the sensitive line. Otherwise, the cup is deformed by the rest of the finger surface, and due to the deformation, the material escapes contact with sensors.

Next, we assumed that one cup was too soft to be grasped. When one cup was to be grasped it easily deformed and no contact with the sensor was established. To simplify our task, we stack two cups together. The resulting "double-cup" was still very soft. Neither in this case was current feedback of the gripper capable of detecting contact surface. Using such sensory in the case of these plastic cups would be ill advised. When grasping such a soft and round object, it is very important not to overshoot the applied force. When too much force is applied, the shape of the cup collapses and the structural integrity of the cup is significantly decreased. The reversing force of the cup is lost, and the cup is bent inward.
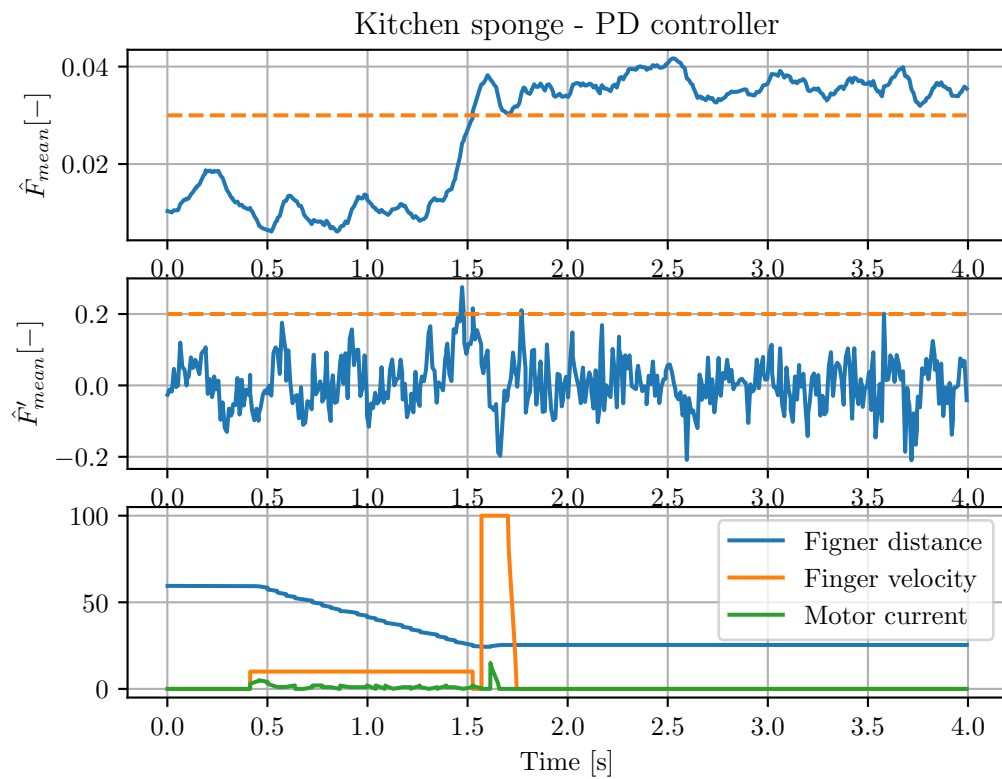
Figure 6.4: Kitchen sponge grasp and object contact detection. The dashed line in the first chart represents the setpoint in the pre-processed value. In the second differentiated signal is shown. The dashed line shows the contact detection threshold.
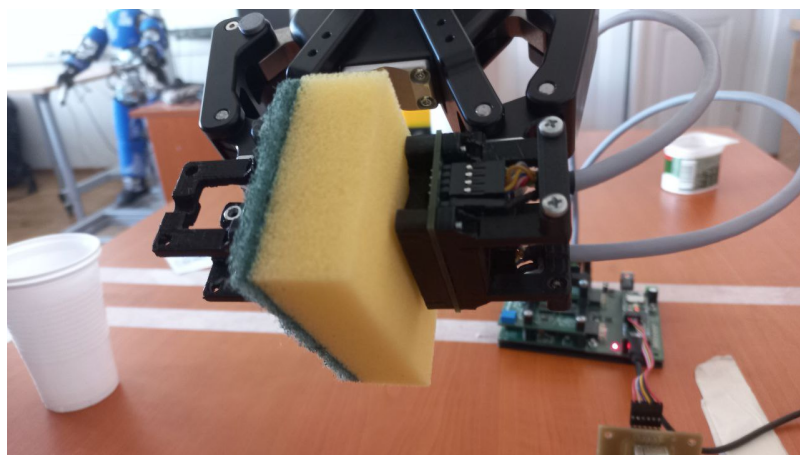
Figure 6.5: Grasped kitchen sponge. Despite the inaccurate setpoint following the sponge is not deformed the all.
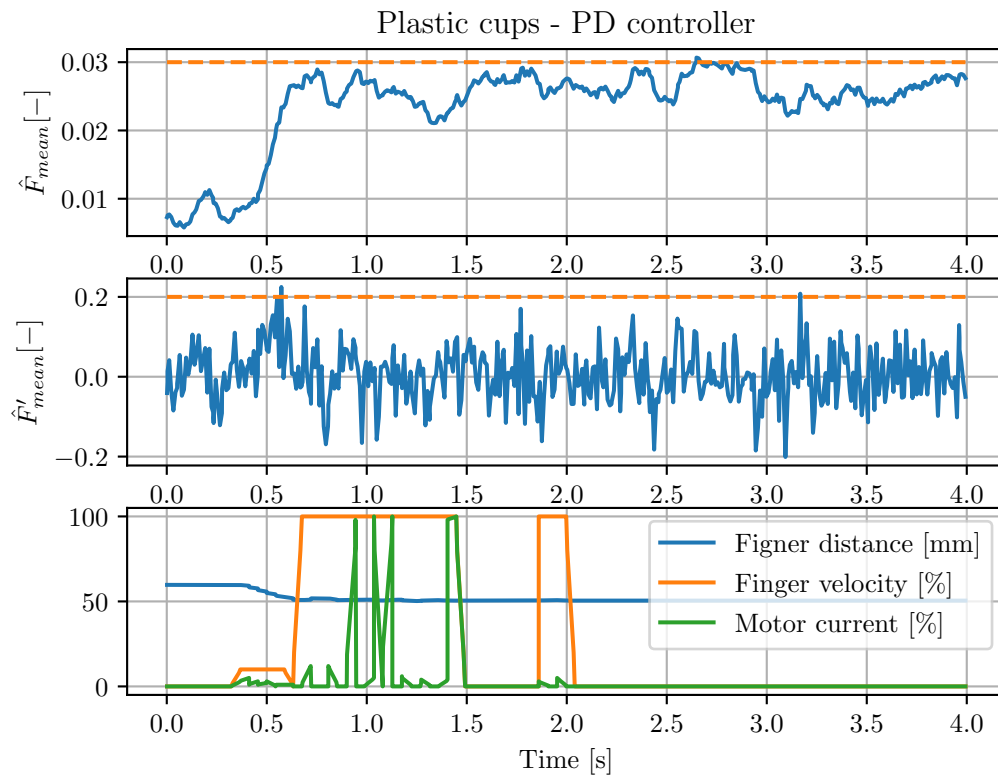
Figure 6.6: Plastic cups grasp and object contact detection. The dashed line in the first chart represents the setpoint in the pre-processed value. In second differentiated signal is shown. Dashed line shows contact detection threshold.
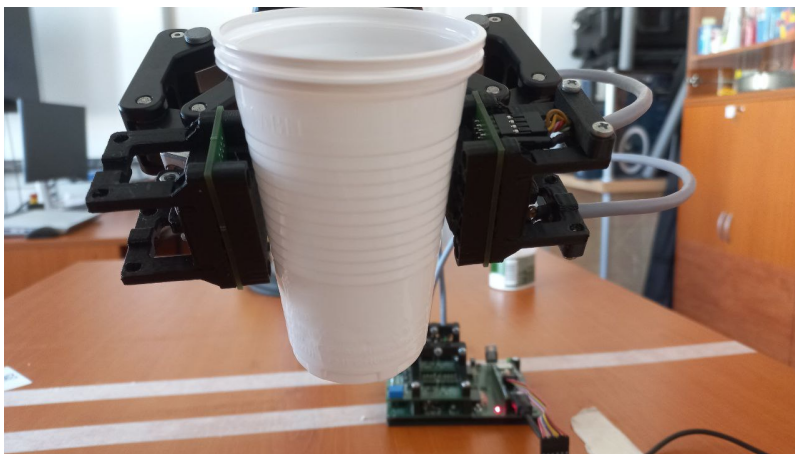
Figure 6.7: Grasped plastic cups.

77

■ Paper card

Finally we present the paper card grasp. The card was made from regular office paper cuts. The paper can be, of course, grasped the easy way, by the wide sides. We, however, wanted to show the sensors sensitivity, and therefore we grasped the card by the thin sides as shown in Figure 6.9. In this configuration, it is very challenging to ensure paper's contact with the sensor. The video recording the grasp of the paper card can be found in attached files.
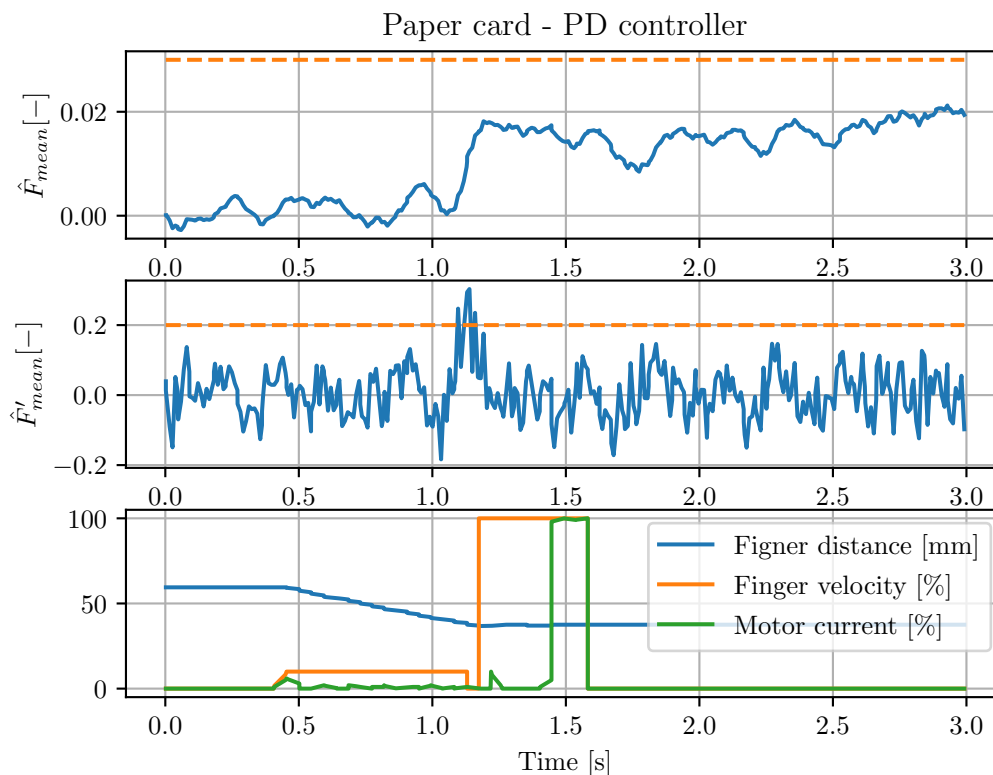
Figure 6.8: Paper card grasp and object contact detection. The dashed line in the first chart represents the setpoint in the pre-processed value. In second differentiated signal is shown. Dashed line shows contact detection threshold.

In this case was the setpoint following rather bad as shows Figure 6.8. We could increase the gain of the controller to achieve the lower error, but the resulting overshoot crumpled the paper. We believe that if we could directly control motor effort, the control performance would be much better. Despite the poor reference following, the task, grasping the paper card was successful.

■ 6.3 Conclusion

As a proof of concept of our sensor, we developed a simple grasping pipeline. Its design was inspired by [22]. Our system had to deal with technical difficulties like resolution of the gripper used, mechanical backlash of the double-leverage mechanism, and rather low
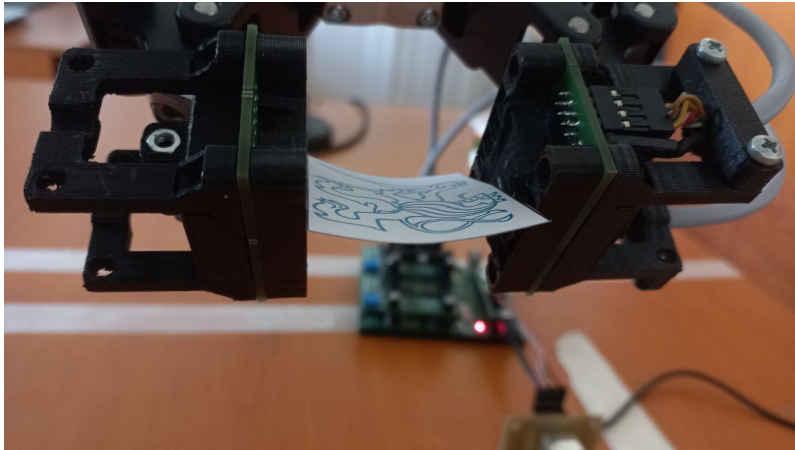
Figure 6.9: Grasped paper. Paper is very slightly bent. Straight card is rather stiff.

command frequency of 40 Hz. Our sensor consists only of a line of sensors that do not cover the entire area of the gripper used. For this reason grasped objects must have been placed correctly into the gripper for the contact with the sensor to be established, by using of full matrix this could be solved. Moreover, our system is spread across multiple devices and overhead for data transfer and jitter effect could be an issue if higher control rates were used. For this reason, we would prefer a more localized system, where we could control the gripper directly.

Despite all these issues, our system was capable of grasping fragile objects such as a paper box, a kitchen sponge, plastic cups, and paper card. We compare the feedback from our sensor with the current response from the gripper motor. Our sensor shows much higher sensitivity to applied forces. In all cases, our sensor could detect contact with the surface earlier than feedback of the gripper.

The designed PD controlled was not always able to ensure a low error of following the setpoit. In case of paper card the following of setpoint reference was rather bad. Despite this error being seemingly high in our paper grasp control, it did not significantly affect performance in our task. All the objects were grasped so that they were not deformed and did not fall out of the gripper.

Chapter 7

Discussion, Conclusion and Future Work

In this thesis we designed a tactile sensor based on contact resistance using graphene aerogel. To accomplish such a task, we familiarized ourselves with graphene aerogel, its synthesis, properties, etc. The design was focused on preserving the unique super-elastic features of graphene aerogel. The final design uses permeable foil as a primary cover and secondary, nonpermeable cover as a protection. We discovered moisture dependence of the graphene aerogel base sensor. To prevent direct contact of the sensor with molecules of water, secondary cover is utilized. In this work, we also encountered the issue of time stability of graphene aerogel based sensor. We reduced the drift by excluding the usage of conductive adhesives and sealing the GA under a secondary cover. Since the seal is not hermetic, we managed only to slow down the drift.

We designed a multitaxel sensor to enhance grasp-evaluation capabilities. For this construction, we used the best single-taxel sensor design we developed with respect to the sensitivity, hysteresis, and stability. Since the sensor was to be built by hand, we decided for a modular architecture where each taxel is inserted into a connector. This architecture brings many connector contact resistances that must be compensated for. During our contraction, we paid attention to the mechanical integrity of the sensor and design the body of the sensor in a way that it is robust and resilient. The sensor was designed to form matrix of taxels; however, due to the low impedance nature of the sensor, we were unable to compensate for the so-called cross-talk currents and also compensate for the influence of connector contact resistance and other parasitic impedance. Instead, we designed the sensor as a single row of taxels. In this configuration, crass-talk currents are not present and, in combination with 4-wire measurement, connector resistances are compensated. Inventing a different approach is the aim of future research on this topic.

We designed our own electronics system to read the tactile array. This system allows to address individual taxels and set different signal processing for each taxel. The reading pipeline is driven by Teensy 4.1 controller with connection to the Robot Operating System, ROS. Since our design uses fast CMOS circuits and switching power components along with analog circuits, we introduce countermeasures to reduce noise. The sensor is connected to the system through a pair of shielded cables, which also reduces noise.

We conducted several tests not only for GA sensors but also for our electronics to make sure that it does not influence sensory evaluation. Graphene sensors were tested to estimate their sensitivity, dynamic range, temperature dependence, and durability. For most of these experiments, we designed our own measurement tools as such devices are not easy

to commercially acquire. To estimate the sensitivity function, we used nonlinear curve fitting techniques. The measured sensitivity of our sensor is much lower than that shown by other published sensors [3, 8, 9, 15], however, our sensor is capable of measuring in much higher dynamic range. With a single sensor we were able to measure forces from 0 to 250N (15.6MPa) without finding signs of damage. The calibration of sensors proved to have quite short time of validity, as features of graphene aerogel still tend to drift in time and, most likely, with atmospheric composition. Next, we tested sensors durability by 1000 iterations of cobble stone lift-up cycles using manipulator Kinova Gen3. The sensor exceeded our expectations as it survived the complete test without breaking.

We estimated the frequency range of the sensors. In this measurement, we were unable to use any reliable reference. In combination with high non-linearity of the sensor we cannot confidently assert the bandwidth. The sensor, on the other hand, was capable of capturing vibrations with frequencies >1kHz. This performance is comparable to the capabilities of the BioTac Finger, which is a well-known sensor. To further support our results, note that the graphene aerogel is capable of high frequency oscillations in the range of MHz, so we assume that the sensor that is damped by additional layers of material performs well while measuring vibrations.

The sensor based on a graphene aerogel shows unique independence from temperature. For example, a sensor based on carbon nanotubes shows a certain temperature dependence [9]. For our sensor, the contact resistance did not show drift when exposed to temperatures in the range [25,50]°C. Our design preserved the temperature independence observed by [12].

Finally, we used our sensor in feedback grasp control with Kinova Gen3 robot and Robotiq 2f-85 gripper Robotiq 2f-85. We compared the performance of our sensor with the current feedback of the gripper used. Our sensor shows to be much more sensitive than the feedback of the gripper used for collaborative tasks between humans and robots. The resulting force dependency was not linear, but allows us to scale multiple sensors to one scale. We implemented the control loop with surface detection and the PD controller. This control loop was a proof of concept. The control was spread across multiple devices interconnected with a fast communication interface. The communication is fast enough, so the resulting jitter is not causing any problems. However, a more localized approach would be preffered. Our grasping control pipe-line was capable of grabbing fragile objects such as plastic cups or paper cards. Since our sensor could not detect the entire grasping area of the gripper, the grasp of round, small, or thin objects highly depends on how the object was inserted into the gripper.

In summary, we designed a new tactile sensor based on a new material. We conducted experiments to obtain its parameters, such as sensitivity, dynamic range, frequency range and temperature stability. Next, we tested the durability of our sensor and stability over long time periods. We designed a custom electronics system to evaluate sensor values that fits our needs. To finally test our prototype, we used it in feedback grasp control.

For future research, we plan to increase sensitivity, frequency range, and time stability. We also plan to examine more the sheer forces dependency of the sensor. Next, we would like to increase the value R_0 of the sensors to reduce the influence of the resistance of the

connector and construct an actual tactile matrix. A new generation of low-density graphene aerogel developed on IoP seems to be promising for such a task. This new aerogel seems to show higher contact resistance and higher sensitivity. Next, we plan to experiment with other principles of tactile sensing using doped sillicones or conductive foams to construct large area artificial skins.

Regarding tactile grasping, we would like to explore more of this area. With respect to this, we plan to investigate the options for direct control of the Robotiq 2f-85 gripper. If this approach would show to be insufficient, we could also design our own gripper, which would incorporate tactile grasping. We could develop such a gripper as a platform for our experiments so that we do not have to rely on manufacturers and adapt our research to their products. This approach might show to be too disadvantageous to be used, but it remains to be seen.

Bibliography

[1] M. Li, Y. Bekiroglu, D. Kragic, and A. Billard, "Learning of grasp adaptation through experience and tactile sensing," in *2014 IEEE/RSJ International Conference on Intelligent Robots and Systems*, 2014, pp. 3339–3346.

[2] P. Svarny, J. Rozlivek, L. Rustler, M. Sramek, Ö. Deli, M. Zillich, and M. Hoffmann, "Effect of active and passive protective soft skins on collision forces in human–robot collaboration," *Robotics and Computer-Integrated Manufacturing*, vol. 78, p. 102363, 2022.

[3] R. Tang, F. Lu, L. Liu, Y. Yan, Q. Du, B. Zhang, T. Zhou, and H. Fu, "Flexible pressure sensors with microstructures," *Nano Select*, vol. 2, no. 10, pp. 1874–1901, Mar. 2021. [Online]. Available: https://doi.org/10.1002/nano.202100003

[4] *PRODUCT MANUAL SYNTOUCH BIOTAC TACTILE SENSOR*, SYNTOUCH INC., September 23, 2020, BioTac finger manual.

[5] M.-Y. Cheng, B.-T. Liao, X.-H. Huang, and Y.-J. Yang, "A flexible tactile sensing array based on novel capacitance mechanism," in *TRANSDUCERS 2009 - 2009 International Solid-State Sensors, Actuators and Microsystems Conference*, 2009, pp. 2182–2185.

[6] M. Lambeta, P.-W. Chou, S. Tian, B. Yang, B. Maloon, V. R. Most, D. Stroud, R. Santos, A. Byagowi, G. Kammerer, D. Jayaraman, and R. Calandra, "Digit: A novel design for a low-cost compact high-resolution tactile sensor with application to in-hand manipulation," *IEEE Robotics and Automation Letters*, vol. 5, no. 3, pp. 3838–3845, 2020.

[7] R. Bhirangi, T. Hellebrekers, C. Majidi, and A. Gupta, "Reskin: versatile, replaceable, lasting tactile skins," in *Conference on Robot Learning (CORL)*, 2021.

[8] B. Zhu, Z. Niu, H. Wang, W. R. Leow, H. Wang, Y. Li, L. Zheng, J. Wei, F. Huo, and X. Chen, "Microstructured graphene arrays for highly sensitive flexible tactile sensors," *Small*, vol. 10, no. 18, pp. 3625–3631, Jun. 2014. [Online]. Available: https://doi.org/10.1002/smll.201401207

[9] L. Wang, H. Peng, X. Wang, X. Chen, C. Yang, B. Yang, and J. Liu, "PDMS/MWCNT-based tactile sensor array with coplanar electrodes for crosstalk suppression," *Microsystems & Nanoengineering*, vol. 2, no. 1, Dec. 2016. [Online]. Available: https://doi.org/10.1038/micronano.2016.65

[10] G. Canavese, S. Stassi, C. Fallauto, S. Corbellini, V. Cauda, V. Camarchia, M. Pirola, and C. F. Pirri, "Piezoresistive flexible composite for robotic tactile applications," *Sensors and Actuators A: Physical*, vol. 208, pp. 1–9, Feb. 2014. [Online]. Available: https://doi.org/10.1016/j.sna.2013.11.018

[11] M. Šilhavík, P. Kumar, Z. A. Zafar, M. Míšek, M. Čičala, M. Piliarik, and J. Červenka, "Anomalous elasticity and damping in covalently cross-linked graphene aerogels," *Communications Physics*, vol. 5, no. 1, Jan. 2022. [Online]. Available: https://doi.org/10.1038/s42005-022-00806-5

[12] P. Kumar, M. Šilhavík, Z. A. Zafar, and J. Červenka, "Contact resistance based tactile sensor using covalently cross-linked graphene aerogels," *Nanoscale*, vol. 14, no. 4, pp. 1440–1451, 2022. [Online]. Available: https://doi.org/10.1039/d1nr06893h

[13] H. Sun, K. J. Kuchenbecker, and G. Martius, "A soft thumb-sized vision-based sensor with accurate all-round force perception," *Nature Machine Intelligence*, vol. 4, no. 2, pp. 135–145, Feb. 2022. [Online]. Available: https://doi.org/10.1038/s42256-021-00439-3

[14] G. D. Maria, C. Natale, and S. Pirozzi, "Force/tactile sensor for robotic applications," *Sensors and Actuators A: Physical*, vol. 175, pp. 60–72, Mar. 2012. [Online]. Available: https://doi.org/10.1016/j.sna.2011.12.042

[15] P. S. Girão, P. M. P. Ramos, O. Postolache, and J. Miguel Dias Pereira, "Tactile sensors for robotic applications," *Measurement*, vol. 46, no. 3, pp. 1257–1271, 2013. [Online]. Available: https://www.sciencedirect.com/science/article/pii/S0263224112004368

[16] J. Klimaszewski and M. Władziński, "Human body parts proximity measurement using distributed tactile robotic skin," *Sensors*, vol. 21, no. 6, p. 2138, Mar. 2021. [Online]. Available: https://doi.org/10.3390/s21062138

[17] L. Jamone, L. Natale, G. Metta, and G. Sandini, "Highly sensitive soft tactile sensors for an anthropomorphic robotic hand," *IEEE Sensors Journal*, vol. 15, no. 8, pp. 4226–4233, 2015.

[18] K. Weiss and H. Worn, "The working principle of resistive tactile sensor cells," in *IEEE International Conference Mechatronics and Automation, 2005*, vol. 1, 2005, pp. 471–476 Vol. 1.

[19] H. Lee, H. Park, G. Serhat, H. Sun, and K. J. Kuchenbecker, "Calibrating a soft ert-based tactile sensor with a multiphysics model and sim-to-real transfer learning," in *2020 IEEE International Conference on Robotics and Automation (ICRA)*, 2020, pp. 1632–1638.

[20] Z. Deng, Y. Jonetzko, L. Zhang, and J. Zhang, "Grasping force control of multi-fingered robotic hands through tactile sensing for object stabilization," *Sensors*, vol. 20, no. 4, p. 1050, Feb. 2020. [Online]. Available: https://doi.org/10.3390/s20041050

[21] J. A. Fishel and G. E. Loeb, "Sensing tactile microvibrations with the BioTac comparison with human sensitivity," in *2012 4th IEEE RAS & EMBS International Conference on Biomedical Robotics and Biomechatronics (BioRob)*. IEEE, Jun. 2012. [Online]. Available: https://doi.org/10.1109/biorob.2012.6290741

[22] J. M. Romano, K. Hsiao, G. Niemeye, S. Chitta, and K. J. Kuchenbeckerr, "Human-inspired robotic grasp control with tactile sensing," *IEEE TRANSACTIONS ON ROBOTICS*, vol. 27, no. 6, 2011.

[23] A. Nag and S. C. Mukhopadhyay, "Fabrication and implementation of carbon nanotubes for piezoresistive-sensing applications: A review," *Journal of Science: Advanced Materials and Devices*, vol. 7, no. 1, p. 100416, 2022. [Online]. Available: https://www.sciencedirect.com/science/article/pii/S2468217921000988

[24] "ROS: Home — ros.org," https://www.ros.org/, [Accessed 15-May-2023].

[25] "ROS/Tutorials - ROS Wiki — wiki.ros.org," https://wiki.ros.org/ROS/Tutorials, [Accessed 15-May-2023].

[26] F. Jacob, *Handbook of Modern Sensors : Physics, Designs, and Applications.* Springer, 2016, vol. Fifth edition. [Online]. Available: https://search.ebscohost.com/login.aspx?direct=true&db=nlebk&AN=1081958&site=ehost-live&scope=site

[27] S. Muller, D. Seichter, and H.-M. Gross, "Cross-talk compensation in low-cost resistive pressure matrix sensors," in *2019 IEEE International Conference on Mechatronics (ICM)*. IEEE, Mar. 2019. [Online]. Available: https://doi.org/10.1109/icmech.2019.8722925

[28] *CDx4HCT08 Quadruple 2-Input AND Gates*, Texas Instruments, August 2019, revision June 2021, 74HCT08 data sheet.

[29] *DC/DC Converters TSR-1 Series, 1 A*, Traco Power, unknown, TSR-1 2450 data sheet.

[30] F. Vidal-Verdú, Ó. Oballe-Peinado, J. A. Sánchez-Durán, J. Castellanos-Ramos, and R. Navas-González, "Three realizations and comparison of hardware for piezoresistive tactile sensors," *Sensors*, vol. 11, no. 3, pp. 3249–3266, Mar. 2011. [Online]. Available: https://doi.org/10.3390/s110303249

[31] *CMOS Analog Multiplexers/Demultiplexer swith Logic Level Conversion*, Texas Instruments, August 1998, revision October 2003, CD4052B data sheet.

[32] *LM134/LM234/LM334, 3-Terminal Adjustable Current Sources*, National Semiconductor Corporation, March 2000, LM334 data sheet.

[33] *Single-Ended, Rail-to-Rail I/O, Low-Gain PGA*, Microchip Inc., 2004, MCP6S91/2/3.

[34] P. Horowitz and W. Hill, *The art of electronics*, 3rd ed. Cambridge, England: Cambridge University Press, Mar. 2015.

[35] *Robotiq 2F-85 & 2F-140 instruction manual*, Robotic Inc., 2018, Robotiq grippers.

Appendix A

List of Attached Files

```
appendix
├── electronics_schematics
│   ├── adjustable_gain.pdf
│   ├── matrix_reading.pdf
│   └── teensy_main_board.pdf
└── grasping_video
    └── paper_grasp.mp4
```